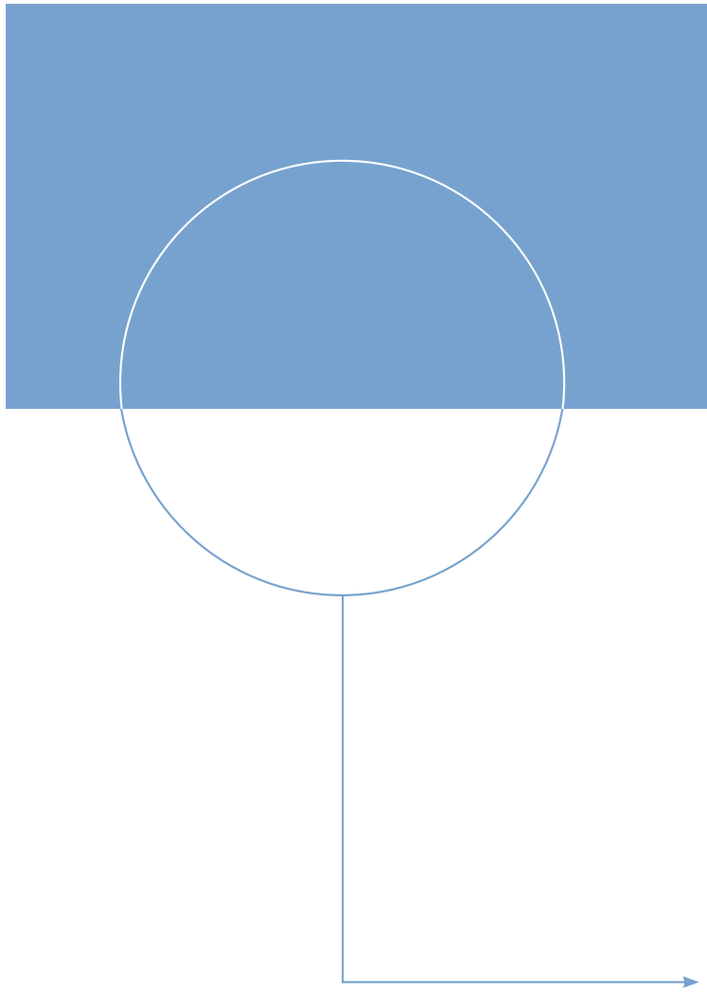

Master's thesis

2019

Oda Marie Johannessen

NTNU
Norwegian University of
Science and Technology
Faculty of Engineering
Department of Geoscience and Petroleum

Oda Marie Johannessen

Evaluation of N/G distribution of the Tofte Formation in the Smørbukk Field through AVO attribute inversion with a focus on tuning and anisotropy effects

June 2019

NTNU
Norwegian University of
Science and Technology

NTNU
Norwegian University of
Science and Technology

NTNU

Norwegian University of
Science and Technology

Evaluation of N/G distribution of the Tofte Formation in the Smørbukk Field through AVO attribute inversion with a focus on tuning and anisotropy effects

Oda Marie Johannessen

Petroleum Geoscience and Engineering
Submission date: June 2019
Supervisor: Kenneth Duffaut
Co-supervisor: Lill-Tove Wetjen Sigernes

Norwegian University of Science and Technology
Department of Geoscience and Petroleum

Abstract

The Tofte Formation in the Smørbukk Field is highly complex with large lateral variations in the net-to-gross distribution. Due to its deep burial and the subsequent low resolution of the seismic data, the formation suffers from tuning effects, and possible anisotropy effects related to the overlying Ror Formation.

This thesis aims to increase the overall understanding of the net-to-gross distribution of the Tofte Formation through an AVO attribute inversion. This involved an evaluation of the anisotropy and tuning effects, followed by a detuning scheme of the input amplitude maps. The resulting intercept and gradient maps are inverted for the net-to-gross ratio to draw insight about the net-to-gross distribution.

This work revealed an expected SW-NE net-to-gross trend in the target area, however more optimistic than the preexisting geological understanding of the depositional pattern of the formation.

While the anisotropy effect was deemed insignificant at common acquisition angles, the tuning effect was found to be dependent on the AVO class of the top and base of the Tofte Formation, decreasing with increasing incident angle. It is found that even small tuning effects appear to have an impact on the resulting AVO attributes. The intercept is enhanced near and at tuning thickness, while the gradient decreases. Both the tuning and anisotropy effects have constructive contributions to the amplitude response, but the contribution from the tuning effects are considerably higher than the anisotropy effects.

The relative net-to-gross maps show an overall agreement with the wells in the area, but some of the areas, which have been noted, are regions of low confidence. Potential explanations for the lower confidence areas is the presence of multiple energy, possible residual tuning effects, noise, or geological trends which are not completely understood. The map should be used with care where marked in this thesis, and these areas should only be analysed internally, and not compared directly with the rest of the map. Further research into the different effects on the amplitude in these areas should be conducted to strengthen the confidence in the net-to-gross map.

Sammendrag

Tofte-formasjonen i Smørbukk-feltet er svært kompleks med store laterale variasjoner i N/G-fordeling. På grunn av formasjonens dyp har seismiske datasett lav oppløsning, og amplituderesponsen til formasjonen lider derfor av tuning-effekter, i tillegg til mulige anisotropieffekter relatert til den overliggende Ror-formasjonen.

Denne masteroppoppgaven tar sikte på å øke den generelle forståelsen av N/G-fordelingen i Tofte-formasjonen gjennom en AVO attributt inversjon. Dette arbeidet innebar en evaluering av anisotropi- og tuningeffekter, etterfulgt av en "detuning"-prosess av amplitudekartene, som igjen ble brukt til å estimere AVO attributtene. De resulterende AVO attributtene ble deretter invertert for N/G for å danne et N/G-kart over Tofte-formasjonen nord i Smørbukk-feltet.

Det endelige N/G kartet viser, som forventet, en sørvest-nordøst N/G-trend i interesseområdet som er mer optimistisk enn den allerede eksisterende geologiske forståelsen av formasjonens avsetningsmønster.

Mens anisotropi-effekten ble ansett som ubetydelig ved vanlige innfallsvinkler, ble tuning-effekten funnet å være avhengig av AVO-klassen av topp og base av Tofte-formasjonen, og avtagende med økende innfallssvinkel. Det ble oppdaget at selv små tuningseffekter ser ut til å ha innflytelse på de resulterende AVO-attributtene. "Intercept" øker nær og ved tuning-tykkelse, mens "gradienten" reduseres. Både tuning- og anisotropieffektene har konstruktive bidrag til amplituderesponsen, men bidraget fra tuningeffektene er betydelig høyere enn anisotropieffektene.

De relative N/G kartene er samstemte med brønnene i området, men noen av områdene, som angitt, er regioner med høy usikkerhet knyttet til seg. Potensielle forklaringer tilknyttet disse usikkerhetene er resterende multippelenergi, mulige tuningeffekter, støy eller geologiske trender som man ikke har full forståelse av per i dag. N/G kartet bør brukes med forsiktighet der det er merket i denne oppgaven. Ytterligere undersøkelse av de ulike effektene på amplitudene i disse områdene bør gjennomføres for å styrke tilliten til N/G kartet ved videre bruk.

Acknowledgement

This thesis is a result of the cooperation between Equinor ASA and the Department of Geoscinece and Petroleum at the Norwegian University of Science and Technology. The thesis has been completed as the final step in the study porgamme Petroleum Geoscience and Engineering, where I have specialised in geophysics.

I would like to thank both of my supervisors, Associate Processor Kenneth Duffaut and Lill-Tove Wetjen Sigernes, Specialist Reservoir Geophysicist at Åsgard Petech, for all the help and guidance they have given me this last year.

Writing this thesis together with Equinor AS has given me an unique opportunity to work on a task related to a real life problem, while observing and learning so much outside of the scope of my thesis of the work in the Åsgard Field. I would therefore like to thank my advisors yet again for giving me this opportunity, for which I am very grateful.

I would also like to thank everyone at Åsgard Petech who have helped me along the way, and who took their time to help me and answer my countless questions.

Oda Marie Johannessen
Trondheim, 2019-06-24

Contents

Nomenclature

$-R_2$	The reflected incident wavelet from the base of a thin bed
ΔT	Two-way travel time
δ	Thomsen (1986) anisotropy parameter
ϵ	Thomsen (1986) anisotropy parameter describing the P-wave anisotropy
ϵ_{kl}	Elements of the strain tensor in Hooke's law
$\frac{\lambda}{4}$	Tuning thickness
γ	Thomsen (1986) anisotropy parameter describing the S-wave anisotropy
λ	The dominating wavelength of a seismic wavelet
λ_d	Dominant wavelength of a seismic wavelet in layer i
μ	Shear modulus
ϕ	Porosity
ϕ_1	Reflection angle of a converted S-wave
ϕ_2	Transmission angle of a converted S-wave
ϕ_0	Critical porosity
ϕ_t	Total porosity
ρ	Density
ρ_f	Fluid density
ρ_m	Matrix density
σ_{ij}	Elements of the stress tensor in Hooke's law
τ	Wavelet period
τ_m	The differential moveout time

θ Incident angle

θ_1 Incident angle

θ_2 Transmission angle

θ_{far} Effective (incident) angle in a far angle cube

θ_{near} Effective (incident) angle in a near angle cube

θ_c Critical (incident) angle

A Amplitude

A_{stable} Amplitude unaffected by tuning

A_{tuning} Amplitude at tuning thickness

A_d Maximum amplitude of the composite wavelet from a thin bed

b Bed thickness

C The curvature component of the reflection coefficient near critical angle

c Arbitrary constant

C_1 Constant used to scale the input intercept maps in the net-to-gross calculation

C_2 Constant used to scale the input gradient maps in the net-to-gross calculation

$c_{\alpha\beta}$ The elastic stress matrix elements in Hooke's law represented using the Voigt scheme

c_{ijkl} The elastic stress tensor elements in Hooke's law

d Layer thickness of layer i

F Constant value

f Frequency

G The gradient of the reflection coefficient

G_t The gradient affected by tuning

K Bulk modulus

M P-wave modulus

p Ray parameter

R The intercept of the reflection coefficient at zero incident angle or offset

R_0 The intercept of the reflection coefficient at zero incident angle or offset

R_1 The reflected incident wavelet from the top of a thin bed

R_d The composite wavelet of R_1 and $-R_2$, or the reflection from a thin bed

$R_{ipp}(\theta)$ P-wave reflection coefficient in an isotropic medium

$R_{pp}(\theta)$ Reflection coefficient of a P-wave

$R_{pp}^{VTI}(\theta)$ P-wave reflection coefficient in a VTI medium

$R_{ps}(\theta)$ Reflection coefficient of a converted S-wave

t Time relative to t_0

t_0 Zero time

$T_{pp}(\theta)$ Transmission coefficient of a P-wave

$T_{ps}(\theta)$ Transmission coefficient of a converted S-wave

V_{clay} Clay volume

V_i Interval velocity in layer i

$V_{p,0}$ P-wave velocity parallel with the symmetry axis in a TI medium

V_p P-wave velocity

V_p/V_s Velocity ratio

$V_{s,0}$ S-wave velocity parallel with the symmetry axis in a TI medium

V_{SH} Shale volume

V_s S-wave velocity

Z Acoustic impedance

z Depth

AVO Angle versus offset

DT Pressure sonic log data

DTS Shear sonic log data

HTI Horizontal (or azimuthal) transverse isotropy

N/G The net-to-gross ratio. The ratio of sand to total rock volume.

TI Transverse isotropy

TTI Tilted transverse isotropy

VSP Vertical seismic profiling

VTI Vertical transverse isotropy

List of Figures

List of Tables

Chapter 1

Thesis Introduction

1.1 Previous work and the challenges met for the Tofte Formation in the Smørbukk Field

The Åsgard Field is a mature field located on the Haltenbanken in the Norwegian Sea. The field is operated by Equinor ASA, and was discovered in 1981, with initiation of production in 1999. The Åsgard Field is comprised of the three deposits Smørbukk, Smørbukk Sør and Midgard, and the discovery of Smørbukk was made in 1985 (Norwegian Petroleum Directorate, 2019). The reservoirs are found in the Åre, Tilje, Tofte, Ile and Garn Formations.

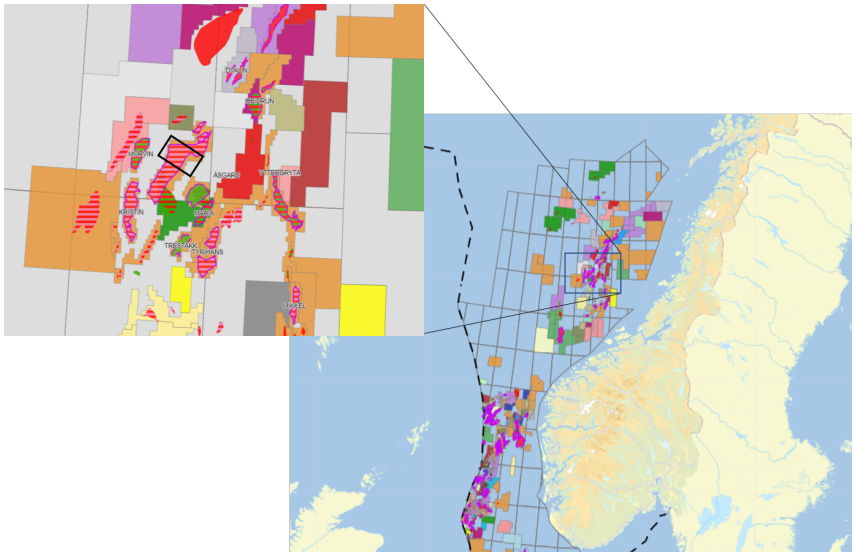

Figure 1.1: An overview of the Åsgard Field in the Norwegian Sea, showing the target area (as a black square) for the AVO analysis. Taken from Norwegian Petroleum (2019).

The target area of the AVO analysis is the northern part of the Smørbukk Field, as indicated in Figure 1.1, and the formation of interest is the Tofte Formation. The work which is presented

here is based on the findings by Johannessen (2018), in addition to any relevant information from earlier in house studies by Equinor AS.

Earlier work on the Tofte Formation in the area of interest include a conceptual understanding of the geology of the formation, and a multiple removal scheme has been applied to the seismic data set covering the area. The next natural step is thus to continue investigating tuning and anistropy effects, before moving on to the net-to-gross distribution of the formation.

1.1.1 The depositional nature of the Tofte Formation

The reservoir quality of the Tofte Formation is poorly understood due to the heterogeneous nature of the deposits and the deep burial of the zone, at depths ranging from 3700 to 4500 meters (Martinius et al., 2005). The reservoir quality of the Tofte Formation depends on the clay or shale content, and the amount of cementation, which can be severe (Equinor in house study, Report 1, 2016). The interpreted depositional pattern of the formation based on well log data in the Smørbukk Field is shown in Figure 1.2. The formation is interpreted to have been deposited from local sources in the west, thinning to the east of the Halten Terrace as it interfingers with the Ror Formation (Dalland, Worsley, and Ofstad, 1988).

The Tofte Formation was deposited in deltaic and estuarine environments with a strong tidal influence (Martinius et al., 2005). Heterolithic deposits are characteristic of tide-influenced environments, and heterolithic sedimentary packages consist of alternations of sandstone and siltstone and/or clay layers with varying lateral extent at a centimetre to decimetre scale. The net-to-gross ratio can vary between 0.3 and 0.9 (Martinius et al., 2005), making interpretation of the overall distribution of the net-to-gross ratio from well log data difficult.

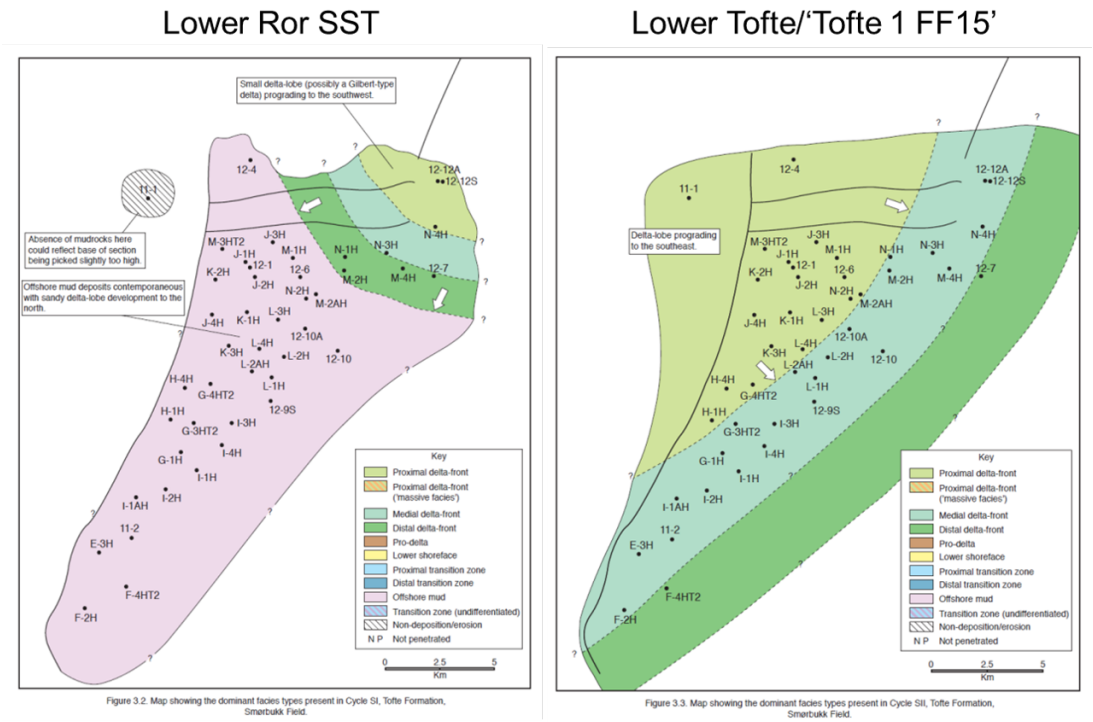

(a)

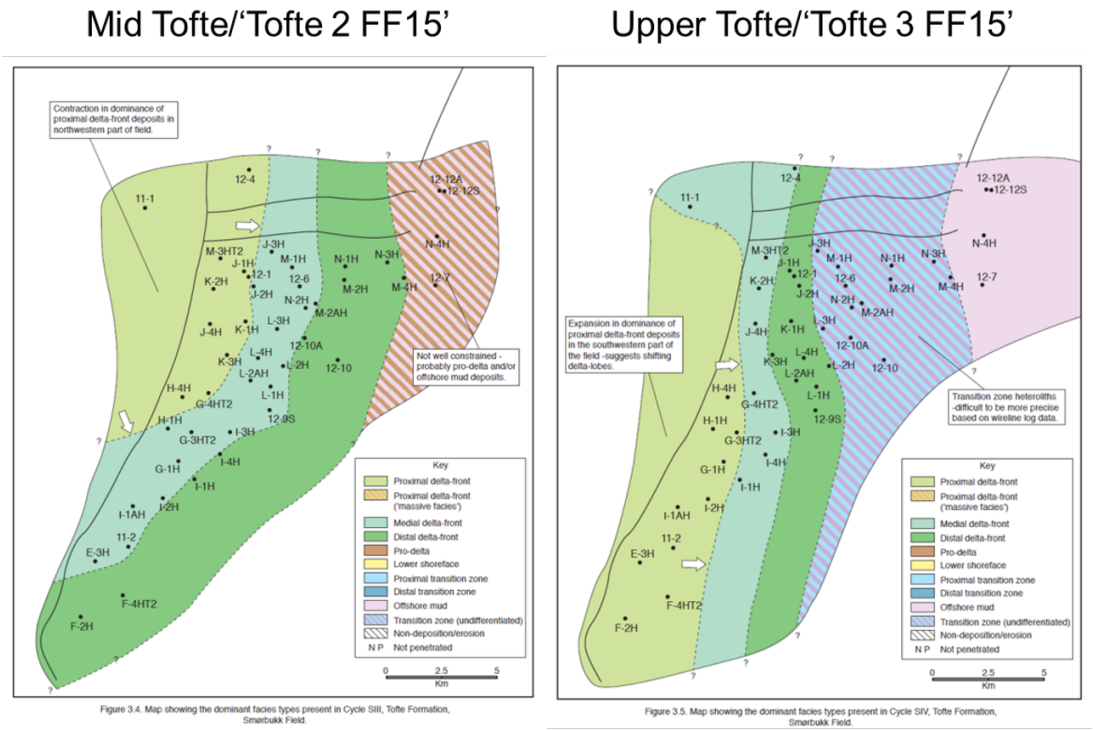

(b)

Figure 1.2: The depositional pattern of the Tofte Formation in the Smørbukk Field. Taken from the Equinor in house study Report 2 (2013).

1.1.2 The additional trouble of tuning and possible anisotropy effects

Johannessen (2018) investigated the feasibility of an AVO analysis of net-to-gross and porosity in the presence of tuning effects in the Tofte Formation. From the wedge modelling it became clear that the Tofte Formation suffers from tuning effects across the Smørbukk Field. The tuning effects are expected to be present for the Tofte Formation top and base reflectors throughout the field, due to the thickness of the formation being close to, and at, tuning thickness. The tuning effects are expected to be constructive.

The analysis found that the net-to-gross has a major control on the AVO behaviour, which is superior to the tuning effects, making an AVO analysis of the Tofte Formation feasible.

Fluid effects are assumed negligible due to the deep burial and near marginal porosities of the formation, and are not expected to be distinguishable from the net-to-gross ratio in an AVO analysis. This has also been concluded in the Equinor in house study Report 1 (2016).

An investigation of the anisotropy effects on the top Tofte Formation reflector was not incorporated in the feasibility analysis conducted by Johannessen (2018), but will be included in this thesis. Previously, little to no work has been done concerning anisotropy effects for the Upper Ror Formation overlying the Tofte Formation. The investigation conducted by Johannessen (2018) concerning the tuning effects is also the first contribution to the work on the matter.

1.2 The thesis objective

The objective of the thesis is to remove the effects of tuning, and to investigate possible anisotropy effects and removing them if necessary, in order to extract information about the net-to-gross distribution from the AVO behaviour of the Tofte Formation. The thesis aims at estimating the net-to-gross ratio in the Tofte Formation in northern part of the Smørbukk Field. The motivation behind the work is to aid in future development of the Smørbukk Field.

The heterogeneity of the formation combined with its deep burial has lead to the complex distribution of a varying net-to-gross ratio and the degree of cementation. The reservoir quality of the Tofte Formation is already difficult to understand and predict, and combined with tuning and possible anistropy effects the task is complicated further. Thus this thesis is trying to describe the net-to-gross distribution in a zone where there is a high degree of lateral variation, combined with tuning and possible anisotropy effects.

The key questions to answer is how the net-to-gross ratio varies in the Tofte Formation in the area of interest, and how this complies with the initial geological understanding of the formation. Other questions the thesis aims at answering is in which manner the tuning effects are affecting the AVO behaviour and how they should be removed, and if necessary, how the anisotropy effects

should be dealt with.

1.3 Approach

The first step in the thesis work will be to evaluate potential anisotropy effects on the Tofte Formation amplitude behaviour caused by the overlying Upper Ror Formation, and to remove these effects if it is deemed necessary. Following the investigation of any anisotropy effects, the tuning effects will be modelled and analysed for the top Tofte Formation reflector, before they are removed through a detuning process.

The third and final step is to perform an AVO analysis with the detuned, and possible anisotropy-corrected, seismic data set. The net-to-gross will be estimated through an inversion of the AVO attributes, and result in a net-to-gross map of the target area. The work flow of the thesis work is given below in Figure 1.3.

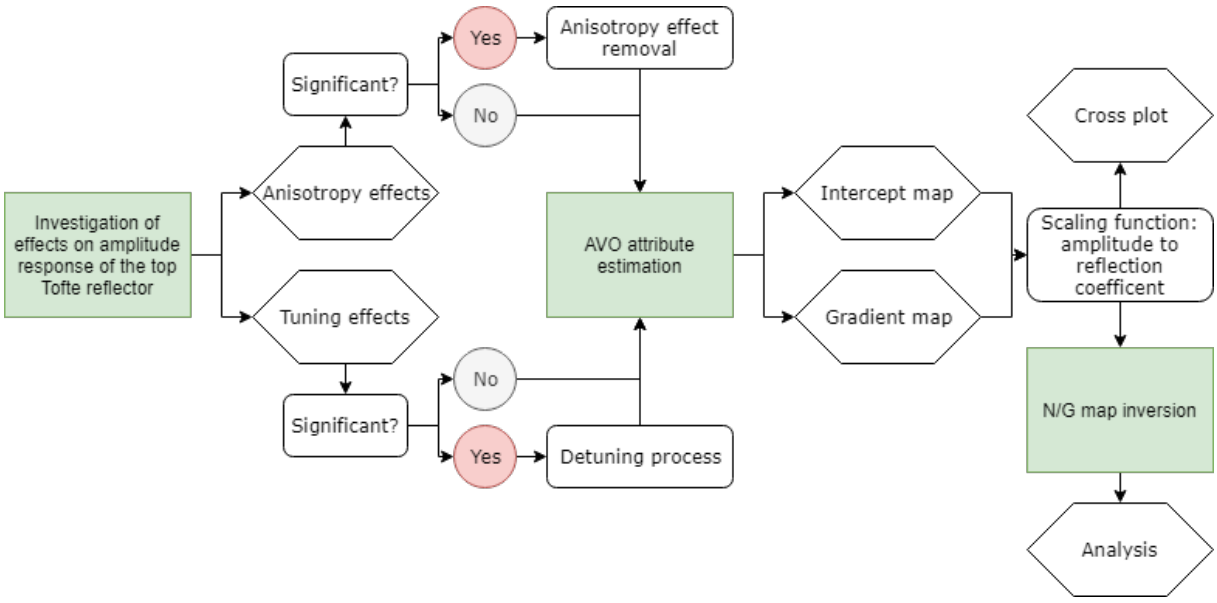

Figure 1.3: The work flow followed in the thesis.

Chapter 2

Background Theory

2.1 Introduction

This chapter describes the basis of an AVO analysis and introduces the AVO attribute net-to-gross inversion which will be performed in this thesis work. The chapter also investigates the background theory of anisotropy and tuning effects, and introduce several methods proposed for detuning seismic data sets.

2.2 AVO analysis

Angle versus offset (AVO) analysis is a diagnostic tool used in the oil and gas industry to determine rock physics parameters from seismic amplitude behaviour as a function of the reflection angle (Avseth, Mukerji, and Mavko, 2008). Today, AVO analysis is used as an exploration tool to discover hydrocarbon accumulations, in addition to being used in lithology identification and fluid parameter analysis (Zhang and Brown, 2001).

The earliest use of information gained from amplitude interpretation as a direct hydrocarbon indicator (DHI) was in the 1970s (Avseth, Mukerji, and Mavko, 2008). With his famous paper and lecture, Ostrander (1984) was the first who actively promoted AVO behaviour as an exploration tool (Castagna, 1993). His discoveries of the angle dependent behaviour of gas-filled sand, combined with the preceding work done in the field and the emerging computer power in the 1980s, was the starting point for the AVO analysis as a popular tool in the petroleum industry.

The AVO analysis has had great success as a diagnostic tool, but it has been known to produce failures (Avseth, Mukerji, and Mavko, 2008). The technique can be heavily influenced by processing and acquisition effects, effects related to lithology and overburden, in addition to tuning effects associated with thin beds. AVO analysis is a tool that can produce reliable results

if it is used wisely and within its limitations, and if it is used wrongly it can produce misleading results which can prove to be costly (Avseth, Mukerji, and Mavko, 2008).

An AVO analysis is most likely to prove to be successful at high porosities and shallow depths, with a gas or light oil replacing the water in a reservoir (Simm and Bacon, 2014). At greater depths and decreasing porosity the AVO analysis has to be used with greater care, and it may not be suitable for an extraction of fluid information, but only details on lithology.

In this section the basis of the AVO analysis is examined and an introduction to the main geologic controls on AVO behaviour is given. For an overview of seismic data processing requirements for an AVO analysis, see Johannessen (2018). Some of the content in this section has been modified from Johannessen (2018).

2.2.1 The basis of the AVO analysis

When an incidence plane P-wave encounters an interface between two semi-infinite isotropic half spaces with contrasts in the acoustic impedance and S-wave velocity, the energy in the wave will be transmitted, reflected and converted (Castagna, 1993), as demonstrated in Figure 2.1. The amount of reflected and transmitted energy, and the behaviour of the resulting waves, are controlled by the P-wave velocity, S-wave velocity and the density of the two half spaces, in addition to the incident angle of the plane P-wave at the interface. The assumption of a plane wave is acceptable as long as the wavelength is considerably shorter than the source-receiver offset (Castagna, 1993), which is generally the case in seismic acquisition today. Conversion of the incident P-wave will not be discussed further here. It is important to keep in mind that reality will be more complex than this simple model described here, and that the AVO behaviour which is observable/detectable is not necessarily related to a single interface.

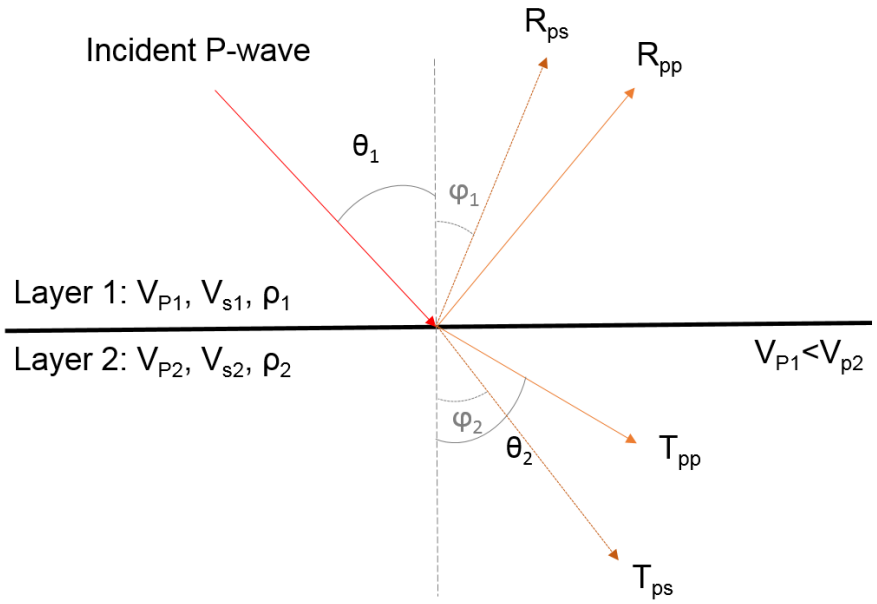

Figure 2.1: The reflection and transmission of an incident P-wave. Redrawn after Simm and Bacon (2014).

The P-wave and S-wave velocities and the bulk density of the half spaces are given in Equation 2.1-2.3. The S-wave and the P-wave velocity are both dependent on the density, ρ, and the shear modulus, μ. The P-wave velocity is in addition dependent on the bulk modulus, K, of the rock and fluid system. The bulk density, ρ, is dependent on the density of the matrix and pore fluids, and of their respective fractions in the sedimentary rock-fluid-mixture. (ha med?)

$$V_p = \sqrt{\frac{M}{\rho}} = \sqrt{\frac{K + \frac{4\mu}{3}}{\rho}} \tag{2.1}$$

$$V_s = \sqrt{\frac{\mu}{\rho}} \tag{2.2}$$

$$\rho = \rho_m(1 - \phi) + \phi\rho_f \tag{2.3}$$

Figure 2.1 demonstrates how the incident angle, combined with the contrast in the layer properties, dictates the behaviour of transmission and reflection. The incident and reflection angle is related as given in Snell's law in Equation 2.4, where p is the ray parameter.

$$p = \frac{\sin\theta_1}{V_{p1}} = \frac{\sin\theta_2}{V_{p2}} \tag{2.4}$$

From Snell's law, the critical angle, θ_c, is given in Equation 2.5. As the incident angle grows larger than the critical angle, θ_c, the wave energy is no longer transmitted in the lower half

space, but refracted along the interface boundary. The critical angle can only be reached and cause refraction if there is a velocity increase going from the upper half space to the lower half space, namely $V_{p1} < V_{p2}$, as evident from Equation 2.5. If $V_{p1} > V_{p2}$ the critical angle will not be reached (Castagna, 1993). Having critical energy present in the seismic data set can lead misinterpretation of amplitudes in an AVO analysis, and should be avoided if possible (Simm and Bacon, 2014).

$$\theta_c = \sin^{-1}(\frac{V_{p1}}{V_{p2}}) \tag{2.5}$$

The reflected energy as a function of incident angle, the reflection coefficient, $R_{pp}(\theta)$, is given as the ratio of the reflected amplitude to the amplitude of the incident P-wave. The transmission coefficient, $T_{pp}(\theta)$ is the ratio of the remaining amplitude which is transmitted to that of the incident P-wave. At zero incidence angle the reflection and transmission coefficients are defined by the contrast in the acoustic impedance, Z, (Castagna, 1993), as given in Equation 2.6 and 2.7.

$$R_{pp}(\theta) = \frac{Z_2 - Z_1}{Z_2 + Z_1} \tag{2.6}$$

$$T_{pp}(\theta) = 1 - R_{pp}(\theta) = 1 - \frac{Z_2 - Z_1}{Z_2 + Z_1} = \frac{2Z_1}{Z_2 + Z_1} \tag{2.7}$$

$$Z = \rho V_p \tag{2.8}$$

Where Z_1 and Z_2 are the acoustic impedance in the upper layer and lower layer, respectively.

Knott (1899) and Zoeppritz (1919) were the first to describe the behaviour of the reflection and transmission coefficients (of the primary plane elastic wave and the converted elastic wave) as a function of the incident angle and elastic properties (Castagna, 1993).

The offset dependent equations were derived assuming that the there is continuity of displacement, with no caviation or slippage along the layer boundary, and continuity of the normal and tangential stress (Castagna, 1993). The equations are very complex, and are not included here for simplicity. They offer little physical insight, and were not used before computer technology became sufficient in the 1970s and 1980s. From their derivation the Zoeppritz (1919) equations are limited by the set of assumptions given below.

Assumptions for which the Zoeppritz (1919) equations are valid (Castagna, 1993)

- The incident wave is assumed to be a plane wave. This assumption is valid when the offset is much larger than the wave length of the incident wave.
- The media above and below the interface are isotropic, homogeneous and elastic.

- The interface is horizontal and plane.
- The equations are assumed to be representative for angles in the pre-critical domain.

Because the Zoeppritz (1919) equations are so complicated, several weak angle and weak contrast approximations are in use today (Simm and Bacon, 2014). Using approximations provides physical insight into the controls on the AVO behaviour, enabling the AVO analysis itself. Bortfeld (1961) made this possible when he linearized the Zoeppritz (1919) equations by assuming small changes in layer properties across the interface. For more detailed information on the different approximations available, the reader is directed to Castagna (1993) and Simm and Bacon (2014). Theese approximations can be used as long as the assumptions given below hold.

Assumptions for which the weak angle and contrast approximations are valid (Avseth, Mukerji, and Mavko, 2008)

- The contrasts across the interface are much smaller than one: $\frac{\Delta\rho}{\overline{\rho}}, \frac{\Delta V_p}{\overline{V_p}}, \frac{\Delta V_s}{\overline{V_s}} << 1$
- The range of incident, reflection and transmission angles in the seismic data are real and far from 90°.

One of the best known weak angle and contrast approximations for the P-wave reflection coefficient is the Aki and Richards (1980) approximation, given in Equation 2.9 (Simm and Bacon, 2014). This formulation was provided by Wiggins, Kenny, and McClure (1983).

$$R_{pp}(\theta) = R + G\sin^2\theta + C\sin^2\theta\tan^2\theta \tag{2.9}$$

R is the intercept, which represents the change in acoustic impedance Z across the interface, and G is the gradient which determines the amplitude change with increasing offset. C represents the curvature of reflection coefficient near the critical angle (Simm and Bacon, 2014). The intercept, gradient and curvature terms are given in Equation 2.10-2.12. In essence, this formulation describes a different angle range in every term, thus simplifying the AVO analysis by separating the contributions in each angle range.

$$R = \frac{1}{2}\left(\frac{\Delta V_p}{\overline{V_p}} + \frac{\Delta\rho}{\overline{\rho}}\right) \tag{2.10}$$

$$G = \frac{\Delta V_p}{2\overline{V_p}} - 4\left(\frac{\overline{V_s}}{\overline{V_p}}\right)^2\left(\frac{\Delta V_s}{V_s}\right) - 2\left(\frac{\overline{V_s}}{\overline{V_p}}\right)^2\left(\frac{\Delta\rho}{\overline{\rho}}\right) \tag{2.11}$$

$$C = \frac{1}{2}\frac{\Delta V_p}{V_p} \tag{2.12}$$

The intercept is controlled by the contrasts in the P-wave velocity and density, while the gradient is additionally controlled by the contrast in the S-wave velocity. The shear velocity contrast is the major control on the gradient, and thus the amplitude behaviour at angles away from the critical angle. A positive shear velocity contrast yields a negative gradient, while a negative contrast yields a positive gradient (Simm and Bacon, 2014). Similarly, the third curvature term takes control of the amplitude behaviour as the incident angle comes close to the critical angle, and it is solely controlled by the contrast in the P-wave velocity.

The P-wave velocity, S-wave velocity and density averages and contrasts which define the intercept, gradient and curvature terms are given in Equation 2.13-2.18.

$$\overline{V_p} = \frac{V_{p1} + V_{p2}}{2} \tag{2.13}$$

$$\overline{V_s} = \frac{V_{s1} + V_{s2}}{2} \tag{2.14}$$

$$\overline{\rho} = \frac{\rho_1 + \rho_2}{2} \tag{2.15}$$

$$\Delta V_p = V_{p2} - V_{p1} \tag{2.16}$$

$$\Delta V_s = V_{s2} - V_{s1} \tag{2.17}$$

$$\Delta \rho = \rho_2 - \rho_1 \tag{2.18}$$

$$(\frac{\overline{V_s}}{\overline{V_p}})^2 = \frac{(\frac{V_{s1}}{V_{p1}})^2 + (\frac{V_{s2}}{V_{p2}})^2}{2} \tag{2.19}$$

Shuey (1985) showed that only the two first terms of the Aki and Richards (1980) equation need to be included for an angle range up to $30 - 40°$, greatly simplifying the interpretation of the AVO behaviour. Given weak layer contrasts, the critical angle will typically be high, and thus in this angle range only the intercept and the gradient are expected to have an effect on the amplitude behaviour.

The most popular two-term approximation was thus provided by Shuey (1985), and is given in Equation 2.20. Leaving out the curvature term allows for a separate investigation of the intercept

and gradient, which can again be inverted for rock physic parameters. In Figure 2.2 the two and three term approximations are compared. It is evident the two term approximation is sufficient for the common acquisition angles ($0° - 40°$) and it is popular in use for AVO crossplot analysis (Simm and Bacon, 2014).

$$R_{pp}(\theta) = R + G \sin^2 \theta \tag{2.20}$$

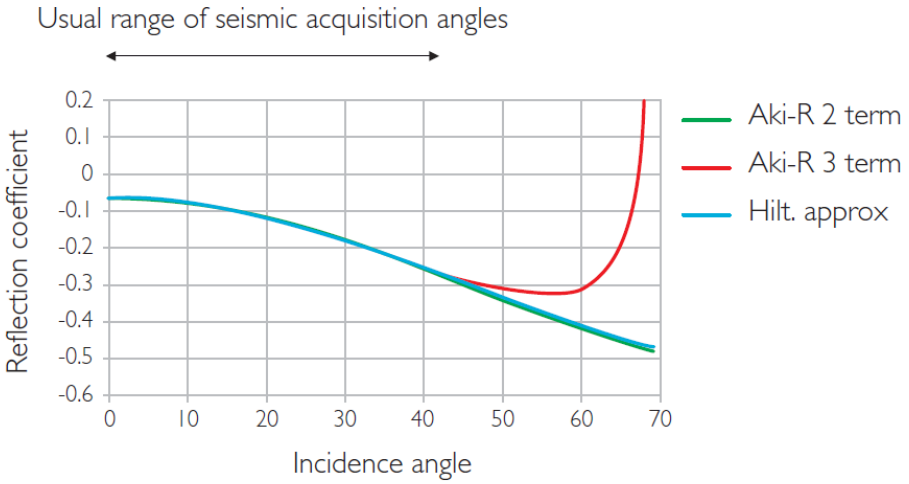

	V_p	V_s	ρ	AI	PR
Shale	2438	1006	2.25	5486	0.397
Gas sand	2600	1700	1.85	4810	0.127

Figure 2.2: Two and three term approximations to the P-wave reflection coefficient compared over an angle range of $0 - 70°$. From Simm and Bacon (2014).

Using Equation 2.20, the intercept and gradient values can be extracted from seismic data sets using Equation 2.21 and 2.22 for the case of a near and far angle cube.

$$R = A_{near} - G \sin^2 \theta_{near} \tag{2.21}$$

$$G = \frac{A_{far} - A_{near}}{\sin^2 \theta_{far} - \sin^2 \theta_{near}} \tag{2.22}$$

2.2.2 AVO classes and the AVO crossplot

Following the advances made with the weak angle and contrast approximations in the 1980s, Rutherford and Williams (1989) provided a classification scheme for the amplitude versus angle behaviour, which is based on the Shuey (1985) equation. The classification divides the different

comnbinations of intercept and gradient behaviour into four main classes, as seen in Figure 2.3 where the reflection coefficient is plotted against the incident angle, θ.

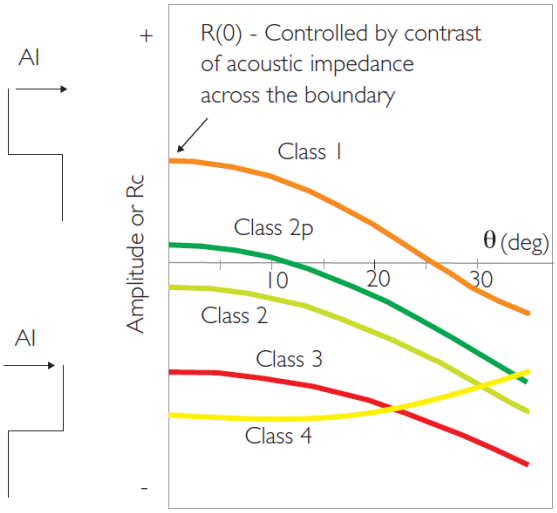

Figure 2.3: The AVO classes defined on the basis of the sign of the intercept and gradient by Rutherford and Williams (1989) and Castagna and Swan (1997). Figure from Simm and Bacon (2014).

The classes where originally used to describe different shale-gas reservoir interfaces, but is today used as a general description of AVO behaviour (Simm and Bacon, 2014). However, it is important to remember that one AVO class is not exclusively linked one single scenario. AVO analysis is a relative concept, and many different scenarios can produce the same AVO signature.

The AVO behaviour can be interpreted in greater detail by implementing an AVO crossplot. In the AVO crossplot the intercept and gradient from the Shuey (1985) approximation is plotted against each other following extraction. In Figure 2.4a the intercept-gradient plot is shown together with the AVO classes. The AVO crossplot can be used to detect relative change in the response from a background trend (Simm and Bacon, 2014), which is here indicated by the black dotted diagonal line in the crossplot in Figure 2.4b. The background trend is usually determined to be the shale overlying a brine saturated sandstone at the target zone. Any deviations, or AVO anomalies, from this background trend can be investigated to obtain information about fluid effects or lithology variations (Simm and Bacon, 2014).

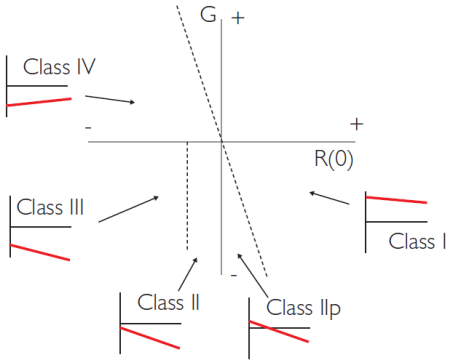

(a) The AVO classes in a crossplot

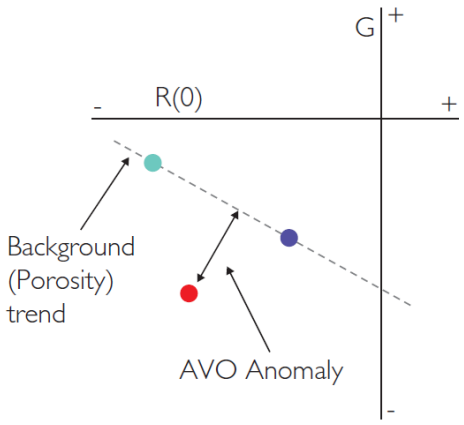

(b) The deviation from the background trend in an AVO crossplot

Figure 2.4: The AVO classes represented in an AVO crossplot. Both figures are taken from Simm and Bacon (2014).

2.2.3 Geological controls on the AVO behaviour in the subsurface

Having described the concepts of an AVO analysis, it is necessary to study the link between the subsurface geology and the AVO behaviour further. As discussed the AVO behaviour of an interface will be dictated by the elastic parameters of the layering above and below it, in addition to the incident angle of the seismic wave. These elastic parameters are again the result of the deposition, burial and compaction of the sediments over time.

The AVO behaviour of an interface is thus determined by the history of compaction and diagenesis of the sediments, the matrix material and the geometry of the pore space, the fluids present in the pore space, the bed thickness, the pressure and the presence of anisotropy in the fabric of the rock (Simm and Bacon, 2014).

Considering a shale-sand interface, the most important control on AVO behaviour will be the porosity, which again controls both the velocities in and the density of the rock. The effect of bed thickness and anisotropy on AVO behaviour will be explained in detail in the following sections. The fluid, pore geometry and pressure effects will not be discussed further here.

When studying rock physic parameters two types of geological trends for the porosity have to be separated from each other, namely the depositional trend and the compactional trend (Avseth, Mukerji, and Mavko, 2008). The depositional environment will set the limits for the porosity at deposition, while the compaction will determine the porosity reduction with burial depth, and increase the stiffness of the rock. Together these trends set the main control for the AVO behaviour. The porosity dependence on burial depth is given in Equation 2.23, where the critical porosity, ϕ_0, will be reduced with an exponential factor dependent on the depth z and a constant

c.

$$\phi = \phi_0 e^{-cz} \tag{2.23}$$

During burial the porosity of the sedimentary rock is reduced through mechanical compaction and diagenesis with precipitation of cement (Simm and Bacon, 2014), increasing both the bulk density and velocities.

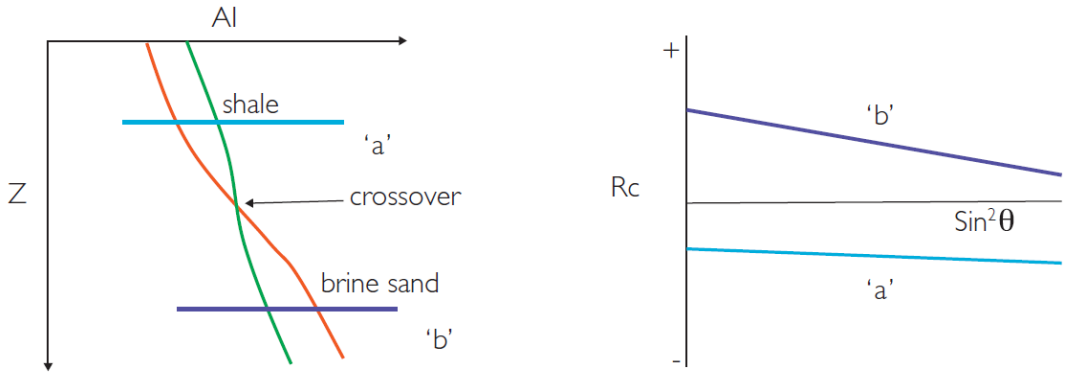

Figure 2.5: The relationship between shale and sand acoustic impedance with increasing depth, and the corresponding AVO behaviour at different depths. Taken from Simm and Bacon (2014).

Figure 2.5 shows that the acoustic impedance, of both shale and sandstone, will increase with increasing depth. However, the compaction and diagenesis also changes the relationship between the acoustic impedance of shale and sandstones, as indicated by the crossover with depth in Figure 2.5. This crossover can also be seen and explained in Figure 2.6. The onset of quartz cementation will start at approximately 70°C (Simm and Bacon, 2014) which will increase the velocities in the sandstone relative to the shale as its rock frame stiffens. Thus the contrasts in rock properties between sand and shale will vary as a function of depth, leading to a varying AVO response also dependent on depth for the "same" shale-sand interface.

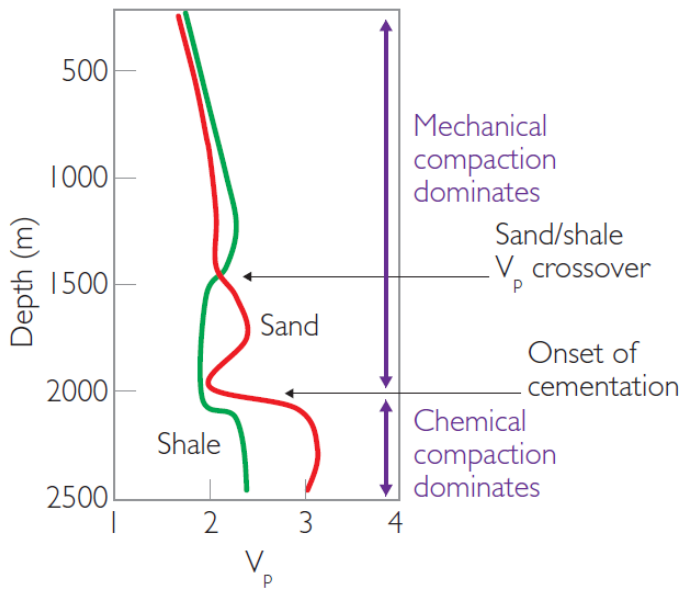

Figure 2.6: The velocity-depth trend relationship between sand and shale in rocks of Paleogene age on the NCS. From Simm and Bacon (2014).

A depositional trend which also will affect the AVO behaviour of a shale-sand interface is the amount of clay or shale present during the deposition of the sand. The porosity (and stiffness) at deposition will be dependent on the sorting of the sedimentary rock, and Marion et al. (1992) described the consequences of adding clay content to unconsolidated sand. Figure 2.7 shows how the addition of clay to a clean sand first results in an increase in the P-wave velocity, as the clay replaces the pore space and reduced the porosity. When the clay has completely filled up the pore space (only micro-porosity remains) and continues to replace the sand, the mixture changes from grain to matrix supported, and the softer clay replacing hard sand grains now causes a decrease in the P-wave velocity.

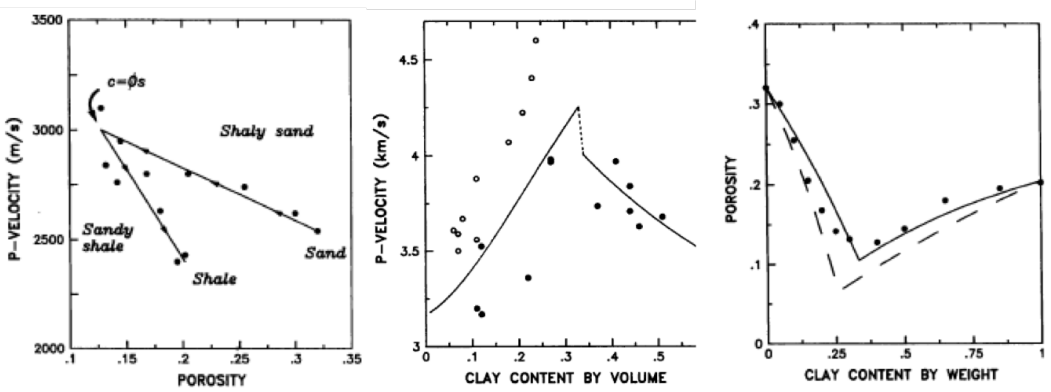

Figure 2.7: The relationship between P-wave velocity, clay content and porosity determined by Marion et al. (1992) at a constant effective pressure of 50 MPa.

2.2.4 The expected AVO behaviour of the Tofte Formation

The Tofte Formation in the Smørbukk Field is defined by its upper boundary, the interface underlying the shaly Upper Ror Formation. The AVO forward modelling conducted by Johannessen (2018) can be seen in Figure 2.8. The expected AVO behaviour of the reflector is type 2 and 3, or possible 1, with an increasingly negative gradient as the net-to-gross ratio increases (Johannessen, 2018). The reflector is best seen at far angles, due to the intercept commonly being close to zero. The negative gradient is believed to be caused by a positive shear velocity contrast between the Tofte and the Upper Ror Formation (Equinor in house study, Report 1, 2016).

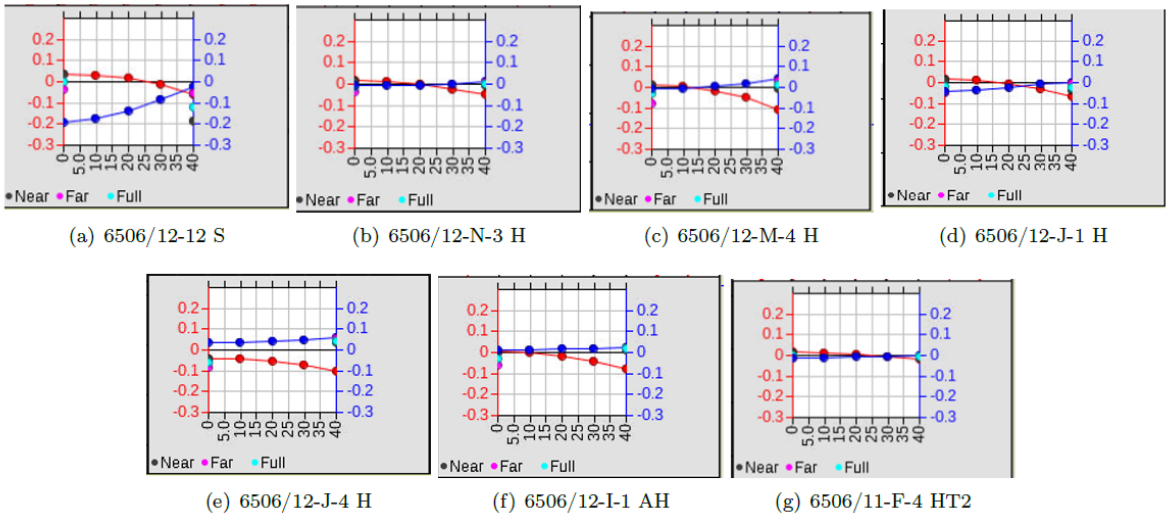

(a) 6506/12-12 S (b) 6506/12-N-3 H (c) 6506/12-M-4 H (d) 6506/12-J-1 H

(e) 6506/12-J-4 H (f) 6506/12-I-1 AH (g) 6506/11-F-4 HT2

Figure 2.8: The modelled AVO behaviour of the top (red) and base (blue) reflector of the Tofte Formation. Taken from Johannessen (2018).

2.2.5 AVO inversion: From intercept and gradient to net-to-gross

The goal of an AVO analysis is to extract information about the geology which controls the AVO behaviour. Both the intercept and gradient are underlain the controls of sorting, or net-to-gross ratio, porosity and burial depth.

Different methods for inverting AVO attributes to rock physics parameters exist and are in use today. For the sake of brevity only one method will be described here, and that is the method provided by Stovas, Landrø, and Avseth (2006), which will be used in the thesis work. For further inquiries about AVO inversion the reader is referred to Avseth, Mukerji, and Mavko (2008) and the work cited there.

The AVO inversion method of Stovas, Landrø, and Avseth (2006) provides a link between the intercept, gradient and the net-to-gross ratio of an effective binary medium composed of sand and shale layers, which is over- and underlain by a semi infinite shale layer. The three layer model which they have utilised can be seen in Figure 2.9a. The different models, M, varies the content of shale and sand layers. The reflectivity of the upper interface between the shale, and the effective mediums with varying shale-content, has been modelled in Figure 2.9b.

At seismic frequences the binary medium will behave as an effective medium, where the net-to-gross will control the overall response from the bed. In Figure 2.9b it can be seen that for increasing net-to-gross (downwards) the amplitude response increases, regardless of the internal distribution of the shale and sand.

The required input for utilising the method for N/G estimation is rock-physic properties for the sand and shale layers, and AVO reflection coefficient intercept and gradient data from a seismic data set.

	M_1	M2	M_3	M_4	M_5	M_6	M_7
Shale	1 × 50	2 × 25	4 × 12.5	8 × 6.25	16 × 3.1	32 × 1.5	64 × 0.7
Sand	2 × 25	3 × 16.7	5 × 10	9 × 5.56	17 × 2.9	33 × 1.4	65 × 0.7

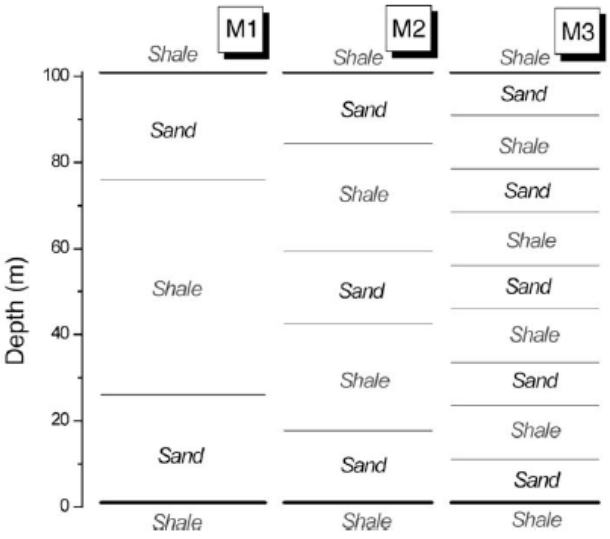

(a) The different binary models investigated, with increasing numbers of thinning sand and shale layers

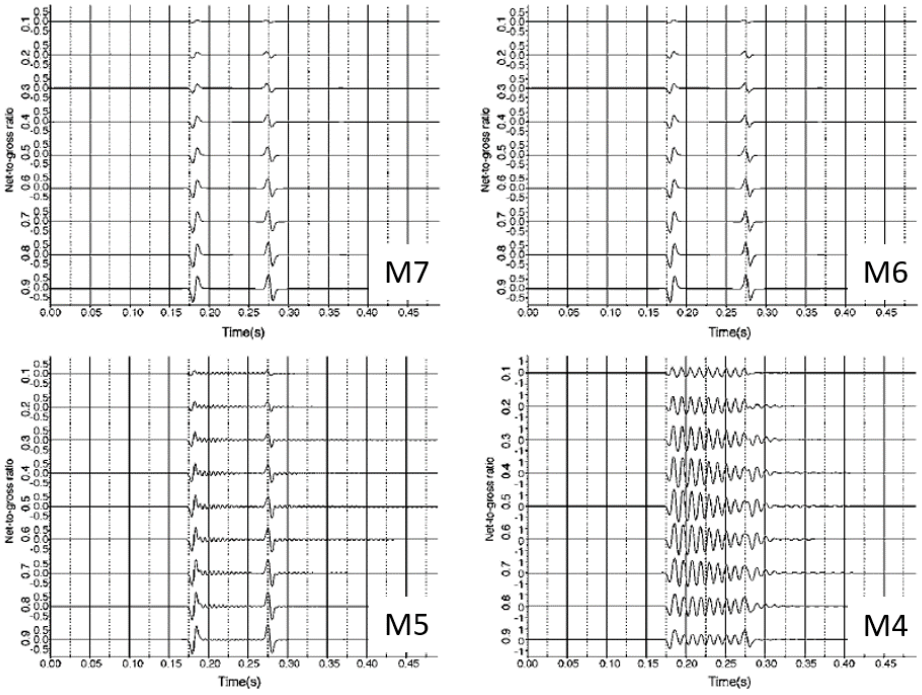

(b) Seismic responses of the effective medium in model 4-7 as a function of increasing net-to-gross ratio.

Figure 2.9: Binary shale-sand model for an effective medium and its reflectivity response

Stovas, Landrø, and Avseth (2006) uses Backus averaging to obtain the properties of the effective medium on the basis that the reflectivity contrast between shale and sand tends to be small. The AVO attributes are estimated from the top reflector between the overlying shale and the effective medium constructed of sand and shale layers. They found that the intercept and gradient at the interface between the shale and the effective binary medium can be defined by Equation 2.24 and 2.25.

$$R = \frac{(N/G)}{4}\left(\frac{\Delta C_{33}}{1 + \frac{(1-(N/G))}{2}\Delta C_{33}} + \frac{\Delta\rho}{1 - \frac{(1-(N/G))}{2}\Delta\rho}\right) \tag{2.24}$$

$$\begin{aligned} G = \frac{(N/G)}{4}\Bigg(&\frac{\Delta C_{33}}{1 + \frac{(1-(N/G))}{2}\Delta C_{33}} - \frac{\Delta\rho}{1 - \frac{(1-(N/G))}{2}\Delta\rho} - 4\Delta C_{44}\gamma_1^2 \\ &\frac{(1 + \frac{(1-2(N/G))}{2}\Delta C_{33})}{(1 + \frac{(1-2(N/G))}{2}\Delta C_{44})(1 + \frac{(1-(N/G))}{2}\Delta C_{33})} + 2\gamma_1^2(1 - \gamma_1^2(N/G)) \\ &\Delta C_{44}\frac{\Delta C_{33} - \Delta C_{44}}{(1 - \Delta C_{44}^2)(1 + \Delta C_{33}^2)}\Bigg) \end{aligned} \tag{2.25}$$

In the case of weak (> 0.20) relative contrasts in all the elastic constants, the effective medium becomes isotropic, setting the anisotropy parameters equal to zero. This reduces Equation 2.24 and 2.25 to Equation 2.26 and 2.27, respectively.

$$R \approx \frac{(N/G)}{4}(\Delta C_{33} + \Delta\rho) = \frac{(N/G)}{2}(\Delta V_P + \Delta\rho) \tag{2.26}$$

$$G \approx \frac{(N/G)}{4}(\Delta C_{33} - \Delta\rho - 4\gamma_1^2\Delta C_{44}) = \frac{(N/G)}{2}(\Delta V_p - 2\gamma_1^2(\Delta\rho + 2\Delta V_s)) \tag{2.27}$$

Where the relative contrasts in the stiffness coefficients are given in Equation 2.28-2.29 and the relative contrast in density is given in Equation 2.30.

$$\Delta C_{33} = 2\frac{C_{33,2} - C_{33,1}}{C_{33,2} + C_{33,1}} \tag{2.28}$$

$$\Delta C_{44} = 2\frac{C_{44,2} - C_{44,1}}{C_{44,2} + C_{44,1}} \tag{2.29}$$

$$\Delta\rho = 2\frac{\rho_2 - \rho_1}{\rho 2 + \rho_1} \tag{2.30}$$

The relative contrasts in the vertical velocities are given below in Equation 2.31 and 2.32.

$$\Delta V_P = \frac{1}{2}(\Delta C_{33} - \Delta\rho) \tag{2.31}$$

$$\Delta V_S = \frac{1}{2}(\Delta C_{44} - \Delta\rho) \tag{2.32}$$

The parameter γ_1^2 is the squared relationship between the S- and P-wave velocity of the shale, as given in Equation 2.33.

$$\gamma_1^2 = (\frac{V_{S1}}{V_{P1}})^2 \tag{2.33}$$

Inverted for net-to-gross Equation 2.26 and 2.27 become

$$N/G \approx \frac{2R}{\Delta V_P + \Delta\rho} \tag{2.34}$$

$$N/G \approx \frac{2G}{\Delta V_P - 2\gamma_1^2(\Delta\rho + 2\Delta V_S)} \tag{2.35}$$

And thus the net-to-gross is approximated as a linear function of the AVO attributes and the relative contrast in the sand and shale elastic parameters.

This AVO attribute inversion method has its limitations, as it may not be expected that the shale and sand properties vary as a binary medium with only two sets of parameters. It may also be too simplistic to vary the layer thicknesses in a systematic way, as the shale and sand content usually will be mixed together in as shaly sand, and not necessarily as separate laminated layering.

2.3 Seismic velocity anisotropy and effects on AVO behaviour

It has been common practice to consider the sedimentary rocks in the subsurface to be isotropic (Thomsen, 1986; Avseth, Mukerji, and Mavko, 2008; Simm and Bacon, 2014). The isotropic approximation is still quite common to use today, and this is due to the demanding equations describing anisotropic wave propagation, and because the most common type of anisotropy, transverse anisotropy, will be disguised as isotropy when the angle of incidence is near vertical (Thomsen, 1986).

In an isotropic medium the properties are directionally independent, and will be the same irrespective of the direction they are measured in (Simm and Bacon, 2014). If the medium is anisotropic one or more of the properties is directionally dependent. A common property of the subsurface where anisotropy can be observed is the velocity, and seismic anisotopy is defined as the dependence of seismic velocity upon angle (Thomsen, 2002).

The assumption of isotropy is not necessarily correct, as most crustal rocks have been shown to be anisotropic through laboratory experiments (Thomsen, 1986). The effect of anisotropy could reverse the expected AVO behaviour of an interface modelled for an isotropic case (Wright, 1987), or it can be expected to enhance negative gradients and to stretch the gradient relative to the intercept (Simm and Bacon, 2014). Blangy (1994) found that anisotropy effects should be taken into account in AVO studies involving shales because its contribution to the AVO signature can be significant.

In this section the basic concepts of anisotropy will be investigated, and the concept of modelling the P-wave relfection, and estimating anisotropy parameters, in anisotropic media will be introduced.

2.3.1 The origin of anisotropy

The small-scale heterogeneity in the sedimentary rocks creates the large-scale anisotropy effect in seismic (Thomsen, 2002). The velocity anisotropy in sedimentary rocks is a product of depositional and compactional processes, in addition to tectonic episodes, and is mainly caused by (Thomsen, 1986):

- Intrinsic anistropy: The preferred orientation of isotropic or anisotropic mineral grains
- Systems of cracks within a sedimentary rock
- Extrinsic anisotropy: Thin beds of individual isotropic and anisotropic layers

2.3.2 Linear elastic and anisotropic media

In media which are considered linear elastic the relationship between stress and strain can be explained by Hookes's law, as given in Equation 2.36 (Mavko, Mukerji, and Dvorkin, 2012), where indices ij corresponds to stress, while kl corresponds to strain. Hooke's law states that such a material will have a linear relationship between stress and strain, and that each component of stress is linearly proportional to each component of strain (Thomsen, 2002).

$$\sigma_{ij} = \sum_{k=1}^{3} \sum_{l=1}^{3} c_{ijkl} \epsilon_{kl} \tag{2.36}$$

Where $i, j = 1, 2, 3$. Hooke's law can be written in compacted form as (Thomsen, 2002),

$$\boldsymbol{\sigma} = \boldsymbol{c}\boldsymbol{\epsilon} \tag{2.37}$$

Where $\boldsymbol{c}$ is the $3\times3\times3\times3\times3$ (fourth-order) elastic stiffness tensor (Thomsen, 2002). It contains the elements c_{ijkl}, and thus consist of a total of 81 components. The number of independent constants in the tensor can be reduced when taking advantage of the symmetry of the stresses and strains, and the fact that there exists a unique strain energy potential (Mavko, Mukerji, and Dvorkin, 2012), which requires the following given in Equation 2.38 and 2.39. These requirements reduces the number of independent constants from 81 to 21 in the elastic stiffness tensor.

$$c_{ijkl} = c_{jikl} = c_{ijlk} = c_{jilk} \tag{2.38}$$

$$c_{ijkl} = c_{klij} \tag{2.39}$$

The tensor c_{ijkl} can be converted to a 6×6 matrix $c_{\alpha\beta}$ by using the Voigt scheme, which is presented in Equation 2.40 and 2.41 (Thomsen, 2002). Four subscripts are reduced to two, as each ij par is reduced to the single index α.

$$ij = ji \rightarrow \alpha \tag{2.40}$$

$$\begin{aligned} 11 &\rightarrow 1 \\ 22 &\rightarrow 2 \\ 33 &\rightarrow 3 \\ 23, 32 &\rightarrow 4 \\ 13, 31 &\rightarrow 5 \\ 12, 21 &\rightarrow 6 \end{aligned} \tag{2.41}$$

Using the Voigt notation the stresses, σ, and strains, ϵ, are written as column vectors containing six elements, as given below in Equation 2.42 and 2.43 (Mavko, Mukerji, and Dvorkin, 2012).

$$\boldsymbol{\sigma} = \begin{bmatrix} \sigma_1 = \sigma_{11} \\ \sigma_2 = \sigma_{22} \\ \sigma_3 = \sigma_{33} \\ \sigma_4 = \sigma_{23} \\ \sigma_5 = \sigma_{13} \\ \sigma_6 = \sigma_{12} \end{bmatrix} \tag{2.42}$$

$$\boldsymbol{\epsilon} = \begin{bmatrix} \epsilon_1 = \epsilon_{11} \\ \epsilon_2 = \epsilon_{22} \\ \epsilon_3 = \epsilon_{33} \\ \epsilon_4 = 2\epsilon_{23} \\ \epsilon_5 = 2\epsilon_{13} \\ \epsilon_6 = 2\epsilon_{12} \end{bmatrix} \tag{2.43}$$

Hooke's law expressed in Voigt notation is thus (Mavko, Mukerji, and Dvorkin, 2012),

$$\begin{bmatrix} \sigma_1 \\ \sigma_2 \\ \sigma_3 \\ \sigma_4 \\ \sigma_5 \\ \sigma_6 \end{bmatrix} = \begin{bmatrix} C_{11} & C_{12} & C_{13} & C_{14} & C_{15} & C_{16} \\ C_{12} & C_{22} & C_{23} & C_{24} & C_{25} & C_{26} \\ C_{13} & C_{23} & C_{33} & C_{34} & C_{35} & C_{36} \\ C_{14} & C_{24} & C_{34} & C_{44} & C_{45} & C_{46} \\ C_{15} & C_{25} & C_{35} & C_{45} & C_{55} & C_{56} \\ C_{16} & C_{26} & C_{56} & C_{46} & C_{56} & C_{66} \end{bmatrix} \begin{bmatrix} \epsilon_1 \\ \epsilon_2 \\ \epsilon_3 \\ \epsilon_4 \\ \epsilon_5 \\ \epsilon_6 \end{bmatrix} \tag{2.44}$$

Which gives the elastic stiffness matrix $\boldsymbol{C}_{\alpha\beta}$ in Equation 2.45. This matrix contains 21 independent constants in the upper triangle and is symmetric about the diagonal. This stiffness matrix describes the highest degree of anisotropy, namely triclinic symmetry (Thomsen, 2002). The upper triangle in the elastic stiffness matrix contains the 21 constants which are needed to describe media of triclinic anisotropy.

$$\boldsymbol{C}_{\alpha\beta} = \begin{bmatrix} C_{11} & C_{12} & C_{13} & C_{14} & C_{15} & C_{16} \\ C_{12} & C_{22} & C_{23} & C_{24} & C_{25} & C_{26} \\ C_{13} & C_{23} & C_{33} & C_{34} & C_{35} & C_{36} \\ C_{14} & C_{24} & C_{34} & C_{44} & C_{45} & C_{46} \\ C_{15} & C_{25} & C_{35} & C_{45} & C_{55} & C_{56} \\ C_{16} & C_{26} & C_{56} & C_{46} & C_{56} & C_{66} \end{bmatrix} \tag{2.45}$$

If the solid is isotropic, the elastic stiffness matrix, as given in Equation 2.46, will only contain two independent elastic constants (Mavko, Mukerji, and Dvorkin, 2012). This means that two constants alone are needed to describe the stress-strain relationship in the solid. This explains why the isotoropic assumption is so common; it is easy to describe and use in computations.

$$C_{\alpha\beta} = \begin{bmatrix} C_{33} & C_{12} & C_{12} & 0 & 0 & 0 \\ C_{12} & C_{33} & C_{12} & 0 & 0 & 0 \\ C_{12} & C_{12} & C_{33} & 0 & 0 & 0 \\ 0 & 0 & 0 & C_{44} & 0 & 0 \\ 0 & 0 & 0 & 0 & C_{44} & 0 \\ 0 & 0 & 0 & 0 & 0 & C_{44} \end{bmatrix} \tag{2.46}$$

Where C_{11}, C_{44} and C_{12} can be defined by Equation 2.47, 2.48 and 2.49, respectively.

$$C_{33} = \lambda + 2\mu = M = \rho V_P^2 \tag{2.47}$$

$$C_{44} = \mu = \rho V_S^2 \tag{2.48}$$

$$C_{12} = C_{33} - 2C_{44} = \lambda = \rho(V_P^2 - 2V_S^2) \tag{2.49}$$

The simplest case of realistic anisotropy is transverse isotropy (Thomsen, 1986; Thomsen, 2002), also called polar anisotropy. A transverse isotropic (TI) medium has a polar symmetry, and layering perpendicular to the symmetry axis will show no anisotropy effects (Simm and Bacon, 2014). The velocity propagation through a transverse isotropic medium will vary with incident angle, or direction, relative to the symmetry axis (Simm and Bacon, 2014).

This type of anisotropy is used to describe thin-bed sequences or massive, unfractured shale sequences (Thomsen, 2002). If the symmetry axis is vertical, the medium is classified as a vertical transverse isotropic (VTI) medium. The symmetry axis can also be tilted, which gives the medium a classification as a tilted transverse isotropic medium (TTI). In the case of a (usually vertically) fractured medium the transverse isotropy with horizontal symmetry (HTI) is used

to describe the medium (Simm and Bacon, 2014). An example of a VTI medium is shown in Figure 2.10.

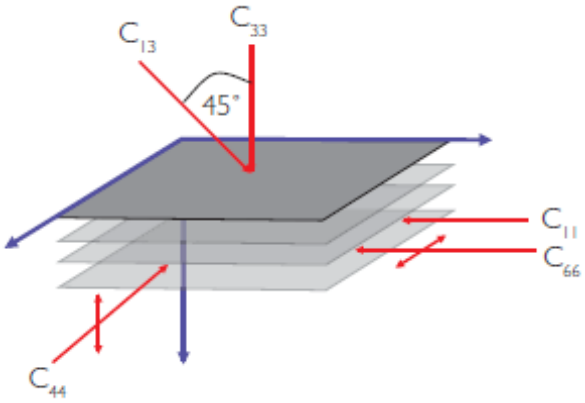

Figure 2.10: A VTI medium and the independent constants needed to describe its stress-strain relationship. From Simm and Bacon (2014).

The elastic stiffness matrix of transverse isotropic (TI) given in Equation 2.50 media contains five independent constants in the non-zero components, which can be seen in Figure 2.10.

$$C_{\alpha\beta} = \begin{bmatrix} C_{11} & C_{11}-2C_{66} & C_{13} & 0 & 0 & 0 \\ C_{11}-2C_{66} & C_{11} & C_{13} & 0 & 0 & 0 \\ C_{13} & C_{33} & C_{13} & 0 & 0 & 0 \\ 0 & 0 & 0 & C_{44} & 0 & 0 \\ 0 & 0 & 0 & 0 & C_{44} & 0 \\ 0 & 0 & 0 & 0 & 0 & C_{66} \end{bmatrix} \tag{2.50}$$

The non-zero components of the elastic stiffness matrix are related to the velocities and density of the medium as given in Equation 2.52-2.56 (Mavko, Mukerji, and Dvorkin, 2012), and the coefficient C_{66} is given in Equation 2.51.

$$C_{66} = \frac{1}{2}(C_{11} - C_{12}) \tag{2.51}$$

$$V_{p,0^\circ} = \frac{\sqrt{C_{33}}}{\rho} \tag{2.52}$$

$$V_{p,45^\circ} = \frac{\sqrt{C_{13}}}{\rho} \tag{2.53}$$

$$V_{p,90^\circ} = \frac{\sqrt{C_{11}}}{\rho} \tag{2.54}$$

$$V_{sv,0^\circ} = \frac{\sqrt{C_{44}}}{\rho} \tag{2.55}$$

$$V_{sh,90^\circ} = \frac{\sqrt{C_{66}}}{\rho} \tag{2.56}$$

2.3.3 Introducing Thomsen parameters and weak anisotropy

In his paper Thomsen defined five parameters, given in Equation 2.52, 2.55, and 2.57-2.59 which can be used to describe TI media. The five parameters are the vertical P- and S-wave velocity, in addition to the three anistropy parameters, ϵ, δ and γ. There is no general consensus for parameterization of transversely isotropic media, but the Thomsen parameters are most often used (Blangy, 1994).

$$\epsilon = \frac{C_{11} - C_{33}}{2C_{33}} \tag{2.57}$$

$$\delta = \frac{(C_{13} + C_{44})^2 - (C_{33} - C_{44})^2}{2C_{33}(C_{33} - C_{44})} \tag{2.58}$$

$$\gamma = \frac{C_{66} - C_{44}}{2C_{44}} \tag{2.59}$$

Assuming weak anisotropy δ in Equation 2.58 can be reduced to (Thomsen, 2002),

$$\delta_{weak} = \frac{C_{13} - C_{33} + 2C_{44}}{C_{33}} \tag{2.60}$$

The three Thomsen (1986) anisotropy parameters are dimensionless, and will reduce to zero in the case of isotropy. ϵ and γ have been found in laboratory experiments to often be positive, while δ is found to be both positive and negative (Thomsen, 2002).

Even though the minerals which makes up the sedimentary rocks can be highly anisotropic, the rock itself is often just weakly anisotropic. It is generally thought that anisotropy is weak (10-20 %) in most geological settings (Thomsen, 1986). Assuming that $\epsilon, \delta, \gamma << 1$ (the limit is set by Thomsen at 0.20) allows for great simplification of the equations describing anisotropic wave propagation (Thomsen, 1986).

The velocities of plane waves under the assumption of weak anisotropy can be described as given in Equation 2.61-2.63 (Thomsen, 2002).

$$V_p(\theta) \approx V_{p0}[1 + \delta \sin^2\theta \cos^2\theta + \epsilon \sin^4\theta] \tag{2.61}$$

$$V_{s\perp}(\theta) \approx V_{s0}[1 + (\frac{V_{p0}}{V_{s0}})^2(\epsilon - \delta)\sin^2\theta\cos^2\theta] \tag{2.62}$$

$$V_{s\parallel} = V_{s0}[1 + \gamma\sin^2\theta] \tag{2.63}$$

For horizontal incidence $\theta = 90°$ the velocities are given in Equation 2.64-2.66

$$V_p(\theta) \approx V_{p0}[1 + \epsilon] \tag{2.64}$$

$$V_{s\perp}(\theta) = V_{s0} \tag{2.65}$$

$$V_{s\parallel} = V_{s0}[1 + \gamma] \tag{2.66}$$

ϵ describes the fractional difference between the horizontal and vertical P-wave velocity. It is known as the P-wave anisotropy, and can be approximated by rewriting Equation 2.64 as given in Equation 2.67. The parameter is insignificant for near-vertical angles (Thomsen, 1986).

$$\epsilon \approx \frac{V_p(\pi/2) - V_p(0)}{V_p(0)} \tag{2.67}$$

The same applies for γ, which describes the S-wave anisotropy. It can be approximated by the fractional difference in horizontal and vertical S-wave velocity, as seen in Equation 2.68. As this discussion involves P-wave reflectivity, this anisotropy parameter is not discussed further.

$$\gamma \approx \frac{V_{s\parallel}(\pi/2) - V_s(0)}{V_s(0)} \tag{2.68}$$

The parameter δ is a more complicated parameter to understand than the two other anisotropy parameters. It has the major control on near-vertical anisotropy (Thomsen, 1986). At near-vertical angles, and when $\Delta\delta \neq \Delta\epsilon$, the contributions of ϵ are smaller than that of δ. At higher angles the contribution of ϵ are larger, and both ϵ and δ will contribute to the anisotropy effects (Thomsen, 2002).

2.3.4 P-wave reflection coefficient approximations including anisotropy

Keith and Crampin (1977) provided the solution of the Zoeppritz (1919) equation for P-wave reflectivity in anisotropic media, while Daley and Hron (1977) introduced the exact generalization in elastic transversely isotropic (TI) media. These solutions are complex and difficult to grasp intuitively (Thomsen, 1993), much like the Zoeppritz equations themselves. It is therefore necessary to use approximations.

Banik (1987) introduced an approximation to the P-wave reflection coefficient in anisotropic media, shown in Equation 2.69. The term $R_{ipp}(\theta)$ is the approximation derived by Aki and Richards (1980) for the P-wave reflection coefficient in isotropic media, given in Equation 2.9. The approximation is valid under the same assumptions as the Aki and Richards (1980) approximation.

$$R_{pp}(\theta) \approx R_{ipp}(\theta) + \frac{\sin^2\theta}{2}\Delta\delta \tag{2.69}$$

Because the approximation only contains the anisotropy contribution from δ, the approximation will only be valid at small incidence angles when the contribution of ϵ is dominated by that of δ. Beyond approximately 18-20 ° the term $\Delta\epsilon$ has a non-negligible, or potentially greater than 10 %, contribution to the P-wave reflection coefficient (Blangy, 1994).

Thomsen (1993) presented a quasi-P-wave reflection coefficient which is valid for the assumption of weak anisotropy, weak (vertical) layer contrasts and pre-critical incidence angles. The approximation is shown in Equation 2.70, and can be applied at larger angles of incidence.

$$\begin{aligned} R_{pp}(\theta) = \frac{1}{2}[\frac{\Delta Z}{Z}] + \frac{1}{2}[\frac{\Delta V_{P,0}}{V_{P,0}} - (\frac{2V_{S,0}}{V_{P,0}})^2\frac{\Delta\mu_0}{\mu_0} + (\delta_2 - \delta_1)]\sin^2\theta + \\ \frac{1}{2}[\frac{\Delta V_{P,0}}{V_{P,0}} - (\delta_2 - \delta_1 - \epsilon_2 + \epsilon_1)]\tan^2\theta\sin^2\theta \end{aligned} \tag{2.70}$$

Where $\overline{Z}$ is the average of (vertical) acoustic impedance in the media, as given in Equation 2.71.

$$\overline{Z} = \frac{Z_1 + Z_2}{2} \tag{2.71}$$

The approximation given by Thomsen (1993) is equivalent to the Banik (1987) expression at smaller angles. Both approximations depends on the contrast in the anisotropy parameters, and not the contrasts themselves.

An approximation for the P-wave reflection coefficient at a horizontal boundary in VTI media was provided by Rüger (1997). It is also an Aki and Richards (1980) type-approximation, but it is more accurate for larger angles and for non-zero difference in δ than the solutions proposed by

Banik (1987) and Thomsen (1993). In the case isotropy, Equation 2.72 reduces to an expression equivalent to the Aki and Richards (1980) equation given in Equation 2.9.

$$R_{pp}^{VTI}(\theta) = \frac{1}{2}[\frac{\Delta Z}{Z}] + \frac{1}{2}[\frac{\Delta V_{p0}}{V_{p0}} - (\frac{2V_{s0}}{V_{p0}})^2 \frac{\Delta\mu}{\overline{\mu}} + \Delta\delta]\sin^2\theta + \frac{1}{2}[\frac{\Delta V_{p0}}{V_{p0}} + \Delta\epsilon]\tan^2\theta\sin^2\theta \quad (2.72)$$

Where

$$\overline{\mu} = \frac{\mu_1 + \mu_2}{2} \quad (2.73)$$

$$\Delta\mu = \mu_2 - \mu_1 \quad (2.74)$$

$$\Delta\delta = \delta_2 - \delta_1 \quad (2.75)$$

$$\Delta\epsilon = \epsilon_2 - \epsilon_1 \quad (2.76)$$

The main problem with this approximation is simply the manner in which the anisotropy coefficients are supplied (Simm and Bacon, 2014). The approximation is a weak contrast and angle approximation, and is only valid under the assumptions given below.

The assumptions for which the Rüger (1997) approximation is valid

- The anisotropy is weak, ϵ, δ, $\gamma << 1$ (or < 0.20) (Thomsen, 1986)
- The contrasts across the interface are small, $\frac{\Delta\rho}{\rho}$, $\frac{\Delta V_p}{\overline{V_p}}$, $\frac{\Delta V_s}{\overline{V_s}} << 1$ (Rüger, 1997)
- The modelled reflectivity responses of the interfaces are in approximated VTI media.

As seen in Equation 2.69 and 2.72 the greatest anisotropy effect will occur when the contrasts in the anisotropy parameters are large and the contrasts in layer properties are small. The response will differ increasingly from the isotropic case with decreasing contrast in layer properties (Blangy, 1994).

To quantify the change in reflection coefficient from an isotropic to an anisotropic case, an anisotropy effect can be defined as the relative change in the reflection coefficient for the anisotropic case and the isotropic case, as given in Equation 2.77.

$$\text{Relative change} = \frac{R_{pp}^{VTI} - R_{pp}}{R_{pp}} \quad (2.77)$$

Figure 2.11 shows the modelled response of an oil sand overlain by a shale. It can be seen that assuming isotropy is sufficient at near angles, but as the incident angle increases, the effect of anisotropy becomes increasingly apparent.

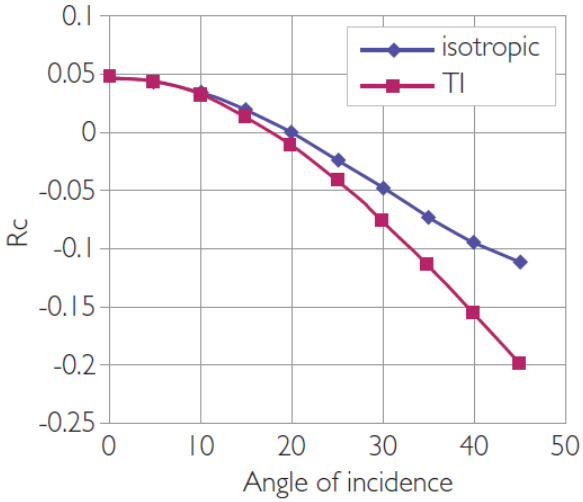

	V_p	V_s	ρ	δ	ε
layer 1	2.438	1.006	2.250	0.150	0.020
layer 2	2.953	1.774	2.036	0.000	0.000

Figure 2.11: A comparison of isotropic and TI reflection modelling for a shale-oil sand interface. From Simm and Bacon (2014).

2.3.5 Estimation of anisotropic parameters

To be able to model the P-wave reflection coefficient, the five Thomsen (1986) weak anisotropy parameters are needed as input. The vertical velocities can be easily obtained, while the anisotropic properties have to be determined from laboratory measurements, vertical seismic profiling (VSP) or seismic refraction (Li, 2006). However, these measurements are usually not available due to measurement and cost restrictions.

Li (2006) developed an empirical method to derive anisotropic properties from conventional properties of sedimentary rocks as an alternative approach to the costly direct or indirect anisotropy measurements. The method has been verified by comparison to, among others, anisotropy parameters obtained from VSP measurements in the North Sea.

The work of Li (2006) is based on earlier findings which proved that variation in seismic velocity caused by anisotropy is proportional to the clay content of the rock. The empirical method he derived consists of quantitative relationships between the vertical P-wave velocity, the vertical S-wave velocity, the clay volume and the anisotropy parameters.

The input conventional rock properties are determined directly or indirectly from either well

logging, laboratory measurements or in-situ seismic measurements, and they are the (vertical) compressional (V_p) and shear (V_s) velocities perpendicular to the bedding, in addition the the clay volume (V_{clay}). The input can be in the form of constants or well logs.

Thus the Thomsen parameters can be estimated empirically by the linear equations listed below in Equations 2.79-2.80. Using these equations yield three different anisotropy logs, and examples of these logs can be seen in Figure 3.2-3.4. The method was tested against VSP measurements conducted in the North Sea, and the results were promising.

$$\epsilon = \frac{0.6V_{clay}(V_p - V_{p,water})}{V_{p,quartz} - V_{p,water} - 2.65V_{clay}} \tag{2.78}$$

$$\gamma = \frac{0.67V_{clay}V_s}{V_{p,quartz} - 2.29V_{clay}} \tag{2.79}$$

$$\delta = 0.32\epsilon \tag{2.80}$$

2.4 Interference and tuning effects

2.4.1 The problem of tuning

The Zoeppritz (1919) equations, and their many approximations, are built on the assumption that the reflection and transmission of an incident plane compressional wave occur at an interface between two infinite half spaces. These equations do not account for the presence of tuning effects as the bed thickness decreases (Xie et al., 2017). Today the target zones for exploration are often not "thick" reservoirs anymore, but rather thinner beds as explored areas become more and more mature (Xie et al., 2017).

So, what are interference and tuning effects? The tuning effect is the occurrence of constructive or destructive interference between a top and base reflector (of a bed) which are closely spaced together (Avseth, Mukerji, and Mavko, 2008). The tuning effect is controlled by the vertical resolution of the seismic data and the elastic properties of the layers.

The vertical resolution separates the beds of thicknesses which are below it into thin beds, and the beds of higher thickness into thick beds (Simm and Bacon, 2014). An example of tuning effect on an amplitude response is shown in Figure 2.12.

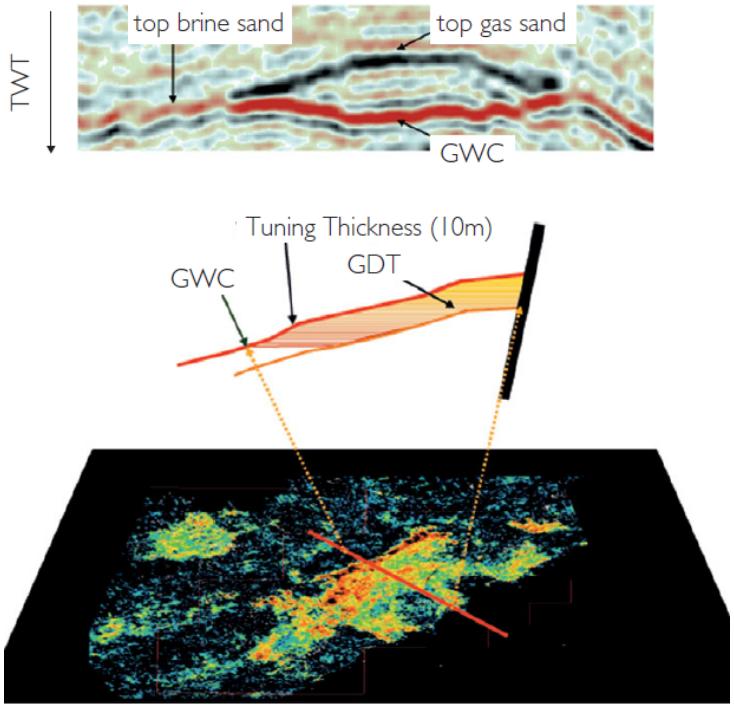

Figure 2.12: An amplitude map with an observable tuning effect (amplitude increase) between the top sand and top gas water contact as the gas sand thins out. From Simm and Bacon (2014).

In order to provide meaningful interpretation of amplitudes in terms of lateral property changes,

such as net-to-gross changes, the effects of tuning should be removed prior to further analysis (Francis, 2015). Possible tuning effects should also be accounted for in an AVO analysis to understand their contribution to the amplitude behaviour with offset, as tuning effects tend to be the most significant factor affecting amplitude maps (Francis, 2015). Some of the content in the following sections have been reworked from Johannessen (2018).

2.4.2 Vertical seismic resolution

The description of interference and tuning effects should start with the main cause of the phenomenon. Tuning becomes an issue as we try to image beds in the subsurface which are close to, or at, the vertical resolution of the seismic data set. The vertical resolution of a seismic data set indicates how large an object has to be in order to be visible in the seismic data. The vertical resolution is defined as the minimum separation between two interfaces such that each of the interfaces are identifiable as two separate events instead of one (Avseth, Mukerji, and Mavko, 2008).

The vertical resolution of a seismic data set is limited by the seismic wavelet's dominating wavelength, λ, as it propagates through the subsurface. The dominant wavelength is defined by Equation 2.81, where V_i is the interval velocity in layer i, and f is the dominant frequency of the wavelet (Avseth, Mukerji, and Mavko, 2008).

$$\lambda = \frac{V_i}{f} \tag{2.81}$$

A layer can be resolved in a seismic data set if its thickness is greater than $\frac{\lambda}{4}$. Beds are detectable down to $\frac{\lambda}{30}$, but the reflection of a bed this thin will not reveal any information about the bed thickness (Avseth, Mukerji, and Mavko, 2008). For thicknesses at $\frac{\lambda}{4}$ and higher it is possible to measure the gross thickness correctly using trough-to-peak measurements. If the bed is thinner, information on the thickness can be provided from amplitude measurements. Below a thickness of $\frac{\lambda}{8}$, the peak-to-trough time separation of the composite wavelet stays constant.

It is not only the dominating wavelength which limits the vertical resolution of the seismic data set. There will always be some noise present following acquisition, causing the resolution to become lower and possibly making beds thicker than $\frac{\lambda}{4}$ unresolvable (Widess, 1973).

2.4.3 What are interference and tuning effects?

Widess (1973) set the basis for the investigation of the tuning phenomenon. In his renowned article he investigated the reflections at zero incidence from a three-layer model constructed of a thin high impedance layer sandwiched in between two layers of lower and equal impedance,

as seen under (c) in Figure 2.13. If the impedance of the upper and lower layer is unequal, or the incidence angle is different from zero, his results are not representative of the reflection response. This is considered the most simplistic model for investigating interference and tuning effects.

Widess (1973) investigated the responses and the interaction of two identical wavelets of opposite polarity with a time shift, ΔT, separating them, a seen in (a) in Figure 2.13. ΔT represents the two-way travel time in the high impedance bed, and is given in Equation 2.82. The approximated responses R_1 and $-R_2$ are given in Equation 2.83 and 2.84, and belong to the wavelet reflected at the top of the layer and at the base of the layer, respectively. The difference between the wavelets, or the composite response, R_d, is shown under (b) in Figure 2.13 and is given in Equation 2.85. The wavelet R_d is approximately 90° phase shifted forward relative to the wavelets reflected from the upper and lower interface of the bed.

R_d represents the reflected response from the thin bed, given that the acoustic impedance is the same above and below it, and that the incidence angle is zero.

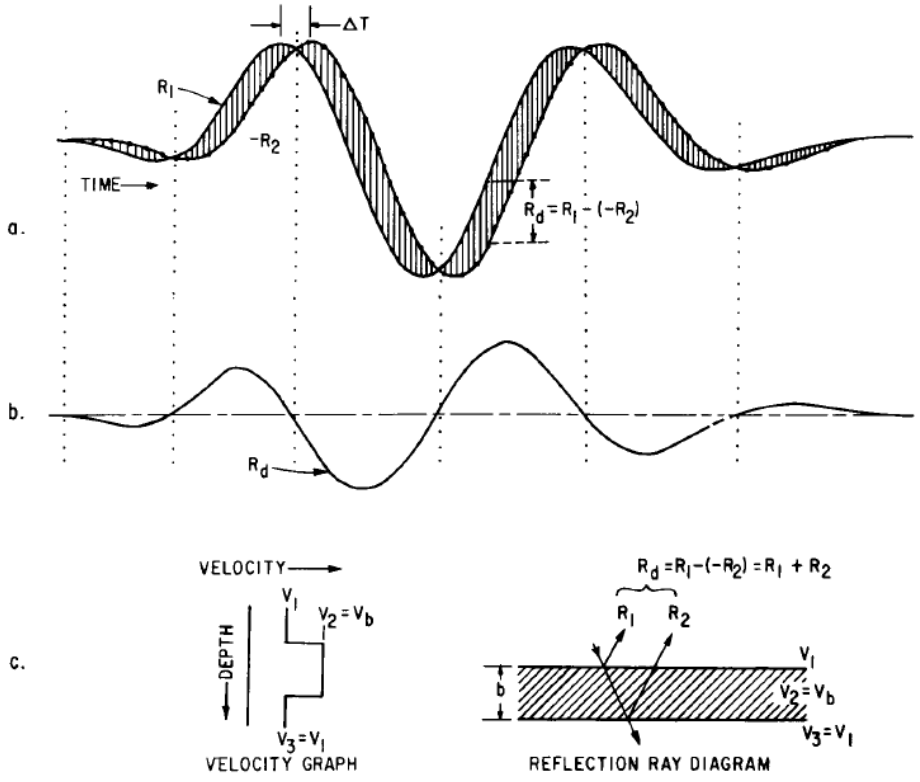

Figure 2.13: (a) The wavelets reflected from the top (1) and the base (2) of the three-layer model. (b) The reflection response of the thin bed. (c) The velocity profile with depth (left) and the reflection ray paths for the reflected wavelets from the top and base of the thin bed (right).

$$\Delta T = \frac{2b}{V_i} \tag{2.82}$$

$$R_1 \cong -A\frac{\cos(t + \frac{d}{V_i})2\pi}{\tau} \tag{2.83}$$

$$-R_2 \cong -A\frac{\cos(t - \frac{d}{V_i})2\pi}{\tau} \tag{2.84}$$

$$R_d = R_1 + R_2 \cong (2A\sin(\frac{2\pi d}{\tau V_i}))\sin(\frac{2\pi t}{\tau}) \tag{2.85}$$

In Equation 2.82-2.84 A represents the amplitude of an incident wave in a bed of thickness higher than $\frac{\lambda}{4}$, and τ the wavelet period of the incident wave in the thin bed. By using the small angle approximation that $\sin x \approx x$, the maximum amplitude of the response from the thin bed, A_d, is given in Equation 2.86.

$$A_d \cong \frac{4\pi Ab}{\tau V_i} \tag{2.86}$$

Widess (1973) further investigated how the composite response of a bed varies as the thickness decreases. He found that interference between the top and base reflection caused a constructive interference at $\frac{\lambda}{4}$. Below a thickness of approximately $\frac{\lambda}{8}$ the interference becomes destructive.

For bed thicknesses lower than $\frac{\lambda}{8}$ the composite response is approximated by the derivative of the incident wave reflected at the top of the thin bed, R_1. Based on this, Widess (1973) named the thickness $\frac{\lambda}{8}$ the "theoretical threshold of resolution". Below this thickness, it is not possible to gain information about the separate top and bottom reflector, and the resolving power is lost.

When bed thickness decreases down towards $\frac{\lambda}{8}$, less energy will be present in the individual reflectors, while the composite energy for the two reflections will increase. As a bed reaches a thickness of $\frac{\lambda}{8}$, the amplitude reflected from it will be approximately equal to $4\pi A\frac{b}{\lambda}$.

The tuning effects are better shown for a wedge model and its corresponding tuning curve, as given in Figure 2.14. In Figure 2.14 it can be seen that the relative amplitude starts increasing at a thickness of $\frac{\lambda}{2}$. This marks the start of the interference effects between the side lobes of the top and base reflectors of the bed. At the tuning thickness $\frac{\lambda}{4}$ the constructive interference is at its highest. At and below this thickness the phenomenon event tuning arises (Avseth, Mukerji, and Mavko, 2008). It can be observed that the curve is approximately linear below a thickness of $\frac{\lambda}{8}$ where the composite response is roughly equal to the time derivative of the incident wavelet.

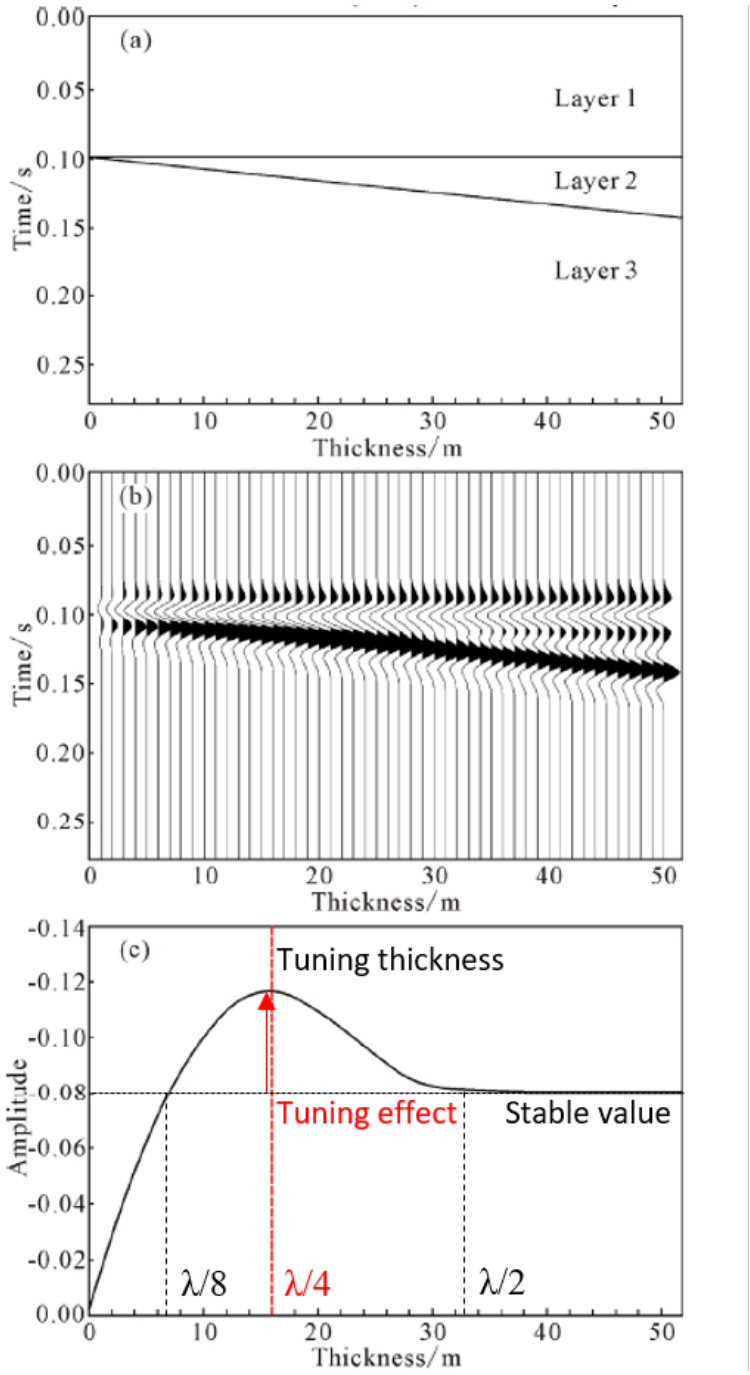

Figure 2.14: A simple wedge model of varying thickness and its corresponding synthetic trace model tuning curve for zero incidence angle. Between a bed thickness of approximately $\frac{\lambda}{2}$ and $\frac{\lambda}{4}$ (red line) the interference is constructive. The destructive interference initiates as the bed becomes thinner than . Edited image from Xie et al. (2017)

Lin and Phair (1993) took the next big step in the investigation of interference and tuning effects by expanding the work done by Widess (1973) to including the effect on offset-dependent reflectivity, namely the AVO tuning effect, on pre-stack data. Their most important findings was that the behaviour of the gradient close to, and at, tuning thickness depends on the algebraic sign of the "geological" intercept and gradient. The "tuned gradient" will reflect the actual gradient

if the both the intercept and gradient originally have the same algebraic sign.

Lin and Phair (1993) used the same one-dimensional model as Widess (1973) to investigate the AVO tuning effect: a thin bed which is surrounded by layering of constant and equal acoustic impedance. A wedge model was created using the layer properties of a shale above and below a gas sand of lower acoustic impedance. A number of synthetic gathers of varying thickness were then investigated. They investigated the tuning curves, similar to the example given in Figure 2.14, of the intercept and gradient separately.

The AVO effect is by Lin and Phair (1993) defined as "the measured AVO gradient as affected by the bedding thickness". While at zero offset the tuning effect is controlled by the vertical resolution and the acoustic impedance in the three layers, they found that with increasing offset the AVO gradient is both affected by tuning and by offset differential moveout, which will not be discussed in detail here.

Lin and Phair (1993) reformulated the expression for the maximum amplitude of the wavelet from the thin bed, A_d in Equation 2.86, by including the differential moveout time, $\frac{b\cos\theta}{V_i}$, in the expression, given in Equation 2.87. A is the amplitude from the bed if it was above tuning thickness.

$$A_d(\theta_1) = \frac{4\pi A b \cos\theta}{V_i \Delta T} \tag{2.87}$$

By combining this modified expression in Equation 2.87 with the Shuey (1985) equation, given in Equation 2.20, expressions for the tuning amplitude gradient and the true amplitude gradient are given in Equation 2.88 and 2.89, respectively.

$$G_t \frac{4\pi b}{V_i \Delta T}(G - \frac{1}{2}A_d) \tag{2.88}$$

$$G = \frac{V_i \Delta T}{4\pi d}(G_t + \frac{1}{2}A) \tag{2.89}$$

With this Lin and Phair (1993) proved that it should be possible to obtain information about the true gradient from the gradient suffering from tuning effects under the conditions provided by Widess (1973). They also showed that the sign of the intercept and gradient was not affected by the interference and tuning effects, which has also later been found by Xie et al. (2017), namely that the AVO class is kept unchanged during tuning for a three layer model. However, the consistency between a given AVO response and the thickness of a bed is still unclear (Xie et al., 2017).

2.4.4 Investigation of tuning effects

The simplest and most common method of studying the tuning effects on a thin bed is to use a synthetic wedge model, first described by Widess (1973) in his famous paper, and later Lin and Phair (1993) and many others. Meckel and Nath (1977) were the first to define the classic tuning curve such as the one given in Figure 2.14.

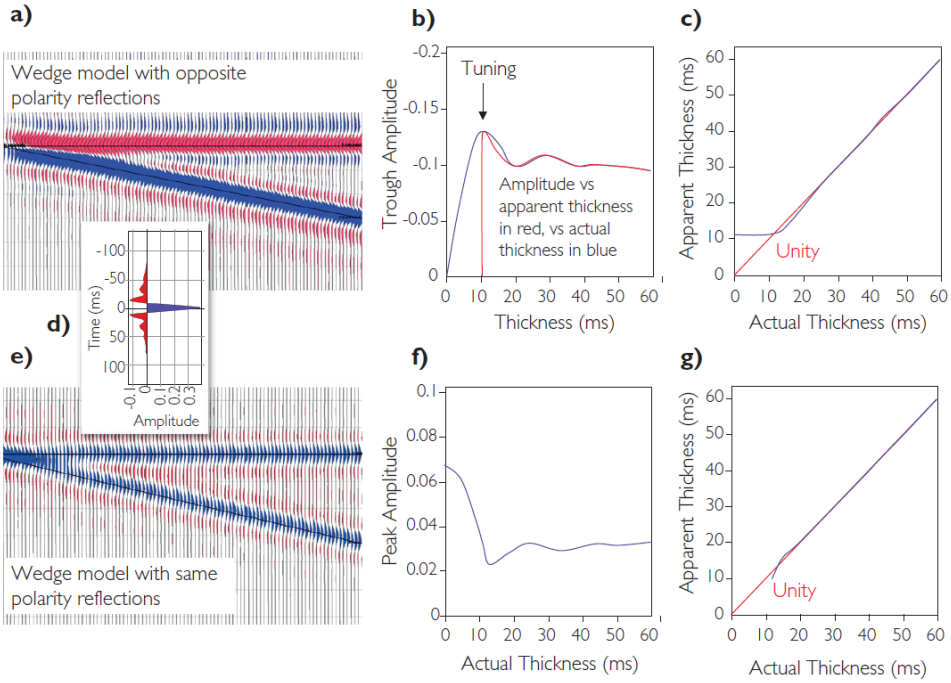

Figure 2.15: Two wedge models with opposite and same polarity reflections, the wavelet used to calculate the reflections, their corresponding tuning curves for the top reflector in the wedge model, and the comparison of the actual and apparent thickness of the wedge. Taken from Simm and Bacon (2014).

The wedge model is normally created for a sandstone containing hydrocarbons with decreasing thickness encased in a shale unit. Examples of wedge models are shown in Figure 2.14 and 2.15.

The wedge model is constructed using a specified wavelet and layer parameters as input, while varying the thickness of the layer which makes up the wedge. The shape of the tuning curve is dependent on the wavelet used to estimate it during the wedge modelling (Connolly, 2007), as can be seen in the tuning curves in Figure 2.15. The synthetic traces are modelled using either the Zoeppritz (1919) equations or any other two- or three-term approximation. The synthetic traces can then be varied with incidence angle to investigate the effect of tuning on AVO behaviour.

The simplest case of a wedge model is when a three layer one dimensional model with equal and constant layer properties in the upper and lower layer are used, while the middle layer is has either lower or higher acoustic impedance and S-wave velocity. The wedge model (a) in

Figure 2.15 is an example of this. The wedge model in (a) has varying, constant (and increasing) properties in all three layers.

Hamlyn (2014) and Xie et al. (2017), among others, examined the impact of thin beds on pre-stack seismic amplitudes and the subsequent effects on AVO attributes. They observed that the intercept and gradient showed a strengthened value at tuning thickness equal to twice the stable amplitude value. It was found that since the input in an AVO analysis will be affected by tuning effects, the same errors will be found in the AVO attributes, and in any inversion results from gained these attributes.

In essence, the investigation of tuning effects by the use of a wedge model will reveal which effects the tuning is expected to have on the amplitudes in a seismic data set, and further in an AVO analysis.

2.5 Detuning: Removal of tuning effects

After having examined tuning effects on the amplitude response of a thin bed, schemes of removing these effects should be considered if deemed necessary. The process of detuning attempts to restore the true amplitude signature of a bed of thickness near, or close to, tuning thickness. This is done by removing, or rather trying to remove, the effects of interference between the top and base reflectors on the top, base or the composite amplitude. Many authors have derived different methods for removing these thin bed effects, and some of them are presented in the following section.

2.5.1 Various methods for detuning amplitudes

The first to provide a detuning scheme were Brown et al. (1984). Their method was developed as a part of a net pay estimate of a reservoir with lateral changes in, among other factors, thickness. The first step was to determine the tuning thickness, then the tuning effect was compensated for by reducing the composite amplitude response where the time thickness was less then the determined tuning thickness. Their method for determining a "tuning curve" was again based on the work of Meckel and Nath (1977).

The next progress was by Brown et al. (1986), continuing the work done by Brown et al. (1984), where tuning effects were investigated by creating statistical tuning curves based on the composite amplitudes and deterministic tuning curves based on different wavelets. The detuning method they derived is shown in Figure 2.16. The tuning curve is shown in red, while the desired stable and unaffected amplitude response is shown in blue. The spread in amplitudes seen can be related to the difference in reservoir properties at equal thicknesses. The amplitudes are detuned by multiplying them with a ratio of the baseline (blue) and the tuning curve which corresponds to the belonging apparent thickness, as given in Equation 2.90.

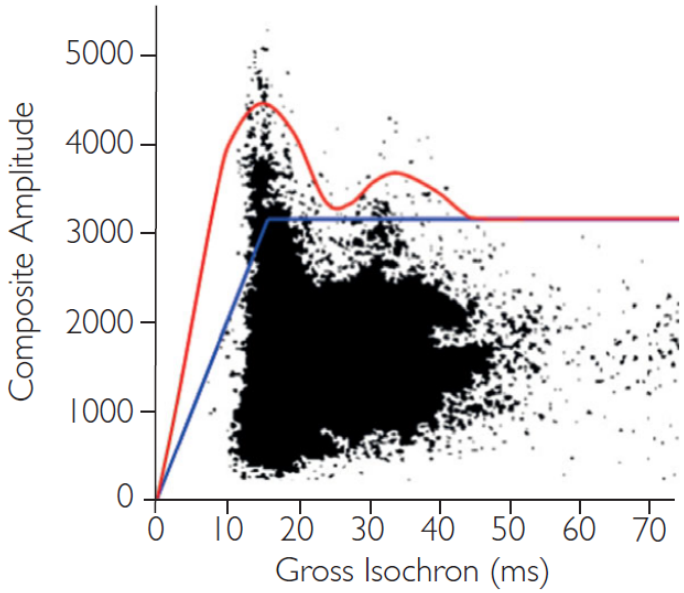

Figure 2.16: The composite amplitude (the sum of the absolute amplitudes of the top and base reflectors) plotted against the seismic thickness. From Simm and Bacon (2014), redrawn after Brown et al. (1986).

Bakke and Ursin (1998) found a correction factor for which the amplitude data can be divided by to correct for offset dependent AVO tuning. Li et al. (2009) presented a detuning scheme they called the "phase scanning" method, based on work by Bakke and Ursin (1998). It differs from earlier methods in that it can handle non-zero phase wavelets, but is still simplistic as it is developed for a three layer sand-shale model where the top and base layer have the same properties, as investigated by Widess (1973) and many others. The purpose of the method provided by Li et al. (2009) is to extract the amplitude response corresponding to the top reflection from the composite response. The method has proven to be stable with noise present, and works well for beds of thicknesses higher than $\frac{\lambda}{8}$, where other earlier methods have proven to work poorly (Li et al., 2009).

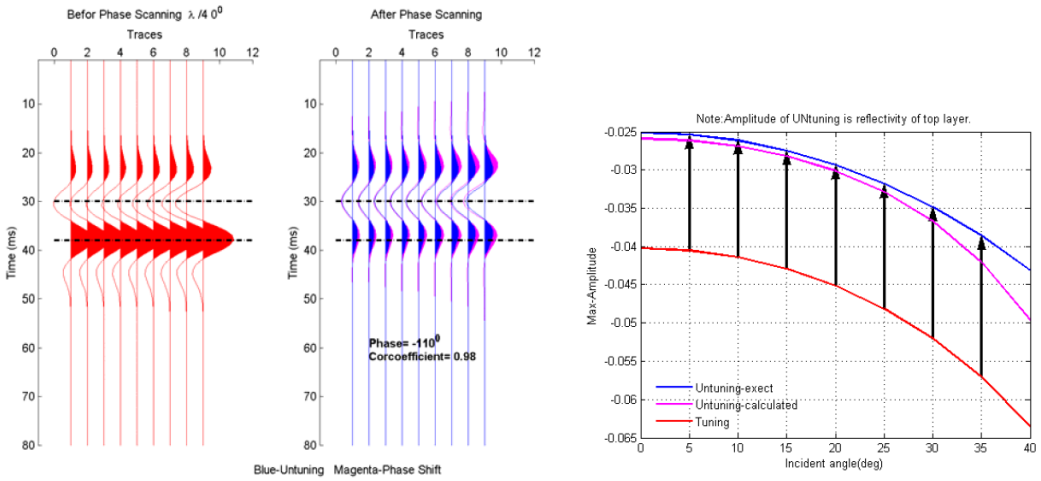

Figure 2.17: The results of the "phase scanning" detuning method derived by Li et al. (2009).

Connolly (2005) and Connolly (2007) developed a method for estimating net-to-gross through coloured seismic inversion, and subsequently provided an improvement to the amplitude scaling method proposed by Brown et al. (1984) and Brown et al. (1986) to remove tuning effects.

Connolly (2007) estimates the net pay from band-limited impedance data, and the detuning scheme is run on the on the impedance data instead of the amplitudes themselves. He follows the same steps as Brown et al. (1986) by calculating a detuning correction curve, which is then applied to the average band-limited impedance. Connolly (2007) has based this method on the findings by Meckel and Nath (1977), and assumes that the net-to-gross is proportional to the average amplitude, and the tuning curve is defined as the amplitude for the case of 100% net-to-gross. It is important to note that proposed by Connolly (2007) is only valid in relatively simple geological environments.

Francis (2015) provides a similar approach to that of Connolly (2007) for detuning amplitudes. The tuning curve is defined either through modelling or empirically from seismic picks (i. e. from a wedge model), and a "reference amplitude" is defined as the relative amplitude we assume will show for no tuning effects. Francis (2015) sets this at approximately half the peak of the highest amplitude observed at the tuning thickness, similar to that of Brown et al. (1986), as seen in Figure 2.16. The detuning is performed by multiplying the ratio of the reference value to that the tuning curve with the seismic amplitudes as a function of thickness, as given in Equation 2.90.

$$A_{\text{detuned}}(b) = A\frac{A_{\text{stable}}}{A_{\text{tuning}}(b)} \tag{2.90}$$

Chapter 3

Well Log Data and Seismic Data Sets

3.1 Input well log data

The well log data used in this thesis is taken from the Smørbukk LFP routine, and the input curves used are listed in Table 3.1.

Table 3.1: Input well log curves

Measurement	Input log data
P-wave velocity, V_p	LFP_VP
S-wave velocity, V_s	LFP_VS
Density, ρ	LFP_RHOB
Shale volume, V_{SH}	LFP_VSH
Total porosity, ϕ_t	LFP_PHIT
Sand flag, net-to-gross	LFP_SAND

The well log curves used as input to create the LFP curves are selected from the best data available, and have been depth shifted and/or environmentally corrected if necessary. In general, the input logs should be continuous, and all wells used in this thesis are reported to have continuous curves on reservoir level (Equinor in house study, Report 3, 2010; Report 4, 2017).

3.1.1 Well log curve details

P-wave velocity V_p

The LFP_VP curves are calculated using a pressure sonic (DT) log which goes through a quality control before it can be used as an LFP_DT log.

S-wave velocity V_s

The shear wave velocity, in the same manner as the P-wave velocity, is not measured directly. It is calculated from a shear sonic (DTS) log, or from the P-wave velocity if no shear sonic log is available.

The sand flag curve

The sand flag curve is defined by two default cut-off values for porosity and shale volume. The lower porosity limit is set at 10%, and the upper shale volume limit at 50%. This curve is used to define the net-to-gross ratio in each well.

Shale volume V_{SH}

The LFP_VSH curve is the final shale volume curve calculated in the LFP process. This curve represents the minimum of the different methods for calculating the shale volume (Equinor in house study, Report 3, 2010). It can be estimated using the gamma ray log, a density-neutron cross-plot, resistivity logs, the spontaneus potential (SP) or the density-sonic cross-plot.

The shale volume calculated here is defined as the wet shale curve, where shale is defined as a fine-grained sedimentary rock composed of silt, mud and clay particles (Equinor in house study, Report 3, 2010).

3.2 Seismic data sets

The seismic data sets which are used in this work are presented in Table 3.2, and their coverage of the Smørbukk Field is shown in Figure 3.1.

Table 3.2: Seismic data sets used in the thesis work

Seismic data set	Area of coverage	Angle range (°)
1.1	Smørbukk Field	4-52
1.2	Southern part of the Smørbukk Field	4-44

The seismic data set used as input in the AVO analysis is data set 1.1, and the avaible angle cubes in this data set are given in Table 3.3.

Table 3.3: Available angle cubes in data set 1.1 used in the AVO analysis

Name of cube	Angle range (°)	Eff. angle (°)	Input in AVO
Data set 1.1-ANG-STK-04-12	4-12	8	*X*
Data set 1.1-ANG-STK-12-20	12-20	16	✓
Data set 1.1-ANG-STK-20-28	20-28	24	✓
Data set 1.1-ANG-STK-28-36	28-36	32	✓
Data set 1.1-ANG-STK-36-44	36-44	40	*X*

The multiple cube model from data set 1.2 is the data set used as input for the preliminary evaluation of residual multiple energy, and the available angle ranges in the near, mid and far cubes are given in Table 3.4.

Table 3.4: Available multiple cubes in data set 1.2

Multiple cube	Angle range (°)
1.2.1 near model	4-17
1.2.2 mid model	17-28
1.2.3 far model	28-44
1.2.4 full model	4-44

The angle cubes included in this thesis work as input in the AVO analysis are the cubes ranging from 12° to 36°. The angle cube of the 4°-12° range is not included because the near offsets may contain multiple energy which has not been removed sufficiently, as discussed in Section 4.1. The cubes ranging from 36° to 44°, and 44° to 52° have not been included because the quality of the top Tofte reflector in the pre-stack gathers appears to be poor above incident angles of $34 - 36°$. For a more detailed discussion, see Chapter 4.

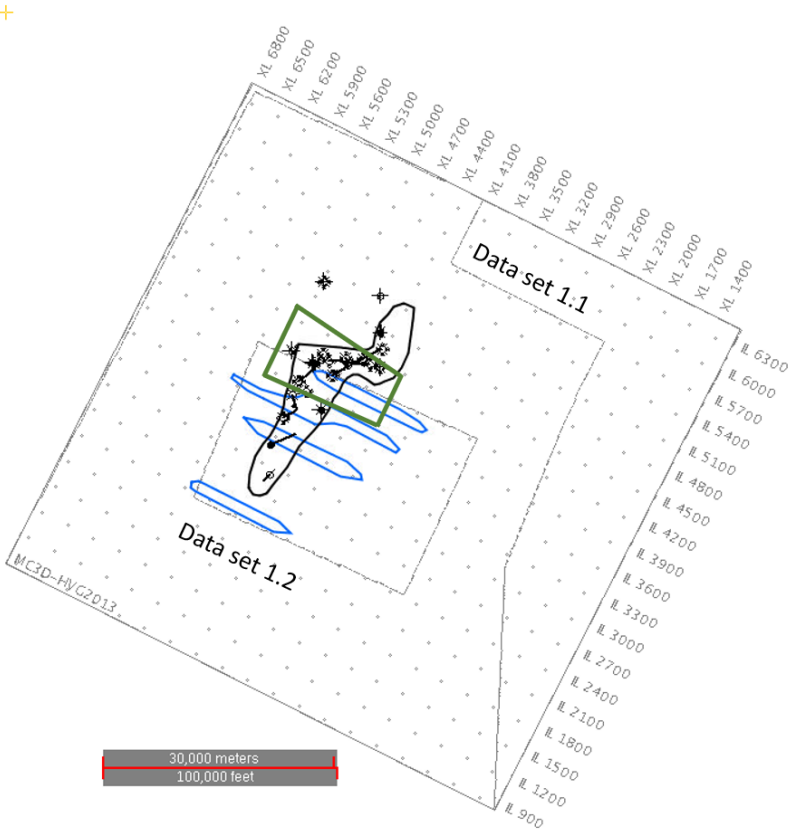

Figure 3.1: An overview of the seismic data sets and their lateral extent. The outline of the Smørbukk Field is in black, and the righoles are shown in blue. The dark green boundary indicates the area of interest. The LFP wells are shown in black. The data quality of the seismic in the righoles can be poor.

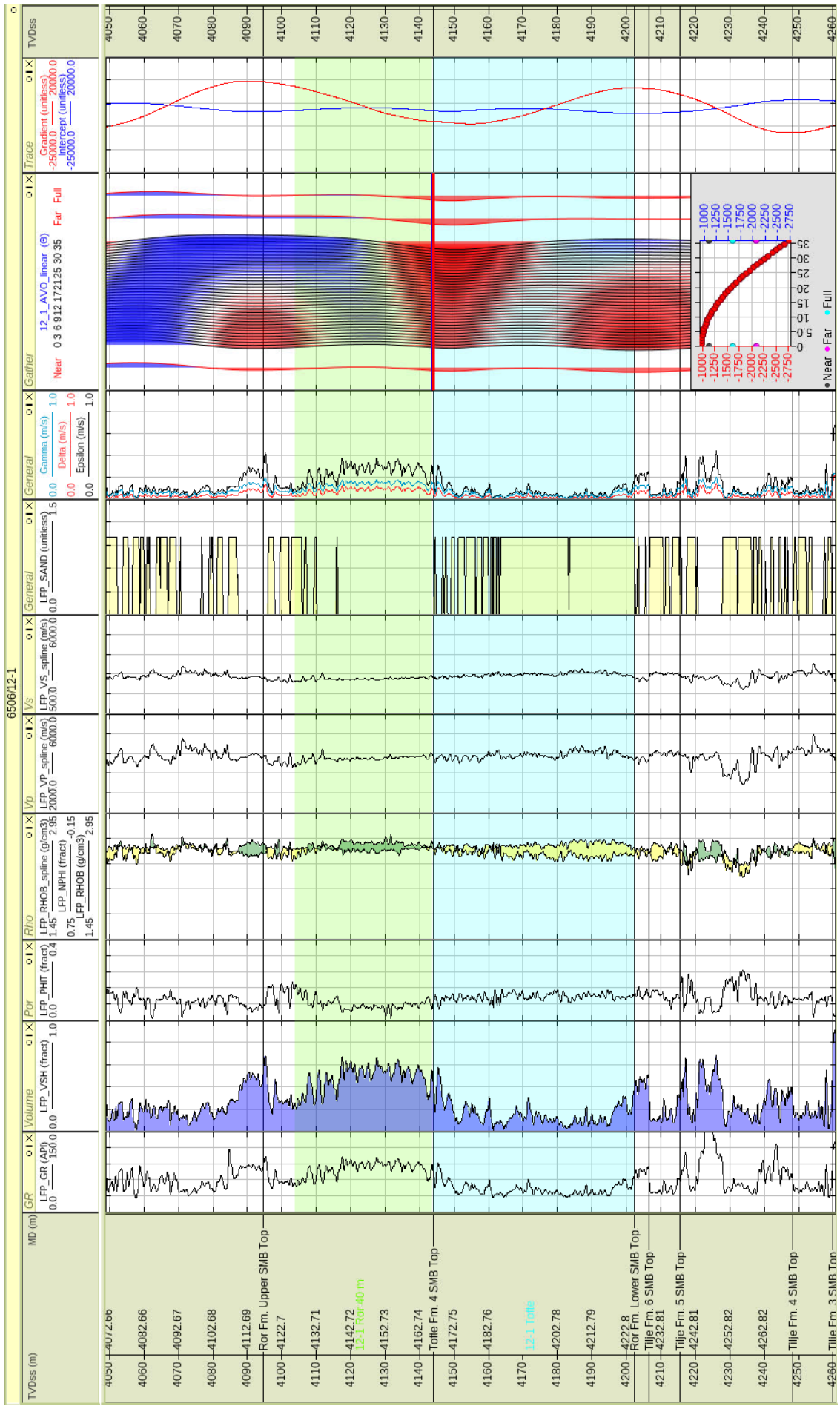

Figure 3.2: A snapshot from well 6506/12-1 showing the Ror, Tofte and Tilje Formations. Well logs from left to right: Gamma ray (GR), Shale volume (V_{SH}), Bulk density, Neutron porosity, P-wave velocity, S-wave velocity, Sand flag, Anisotropy parameters (γ, δ and ϵ), AVO forward modelling (Shuey equation) gather using a wavelet extracted from the seismic data set for effective angle 24°, Gradient and Intercept measurements of the AVO gather.

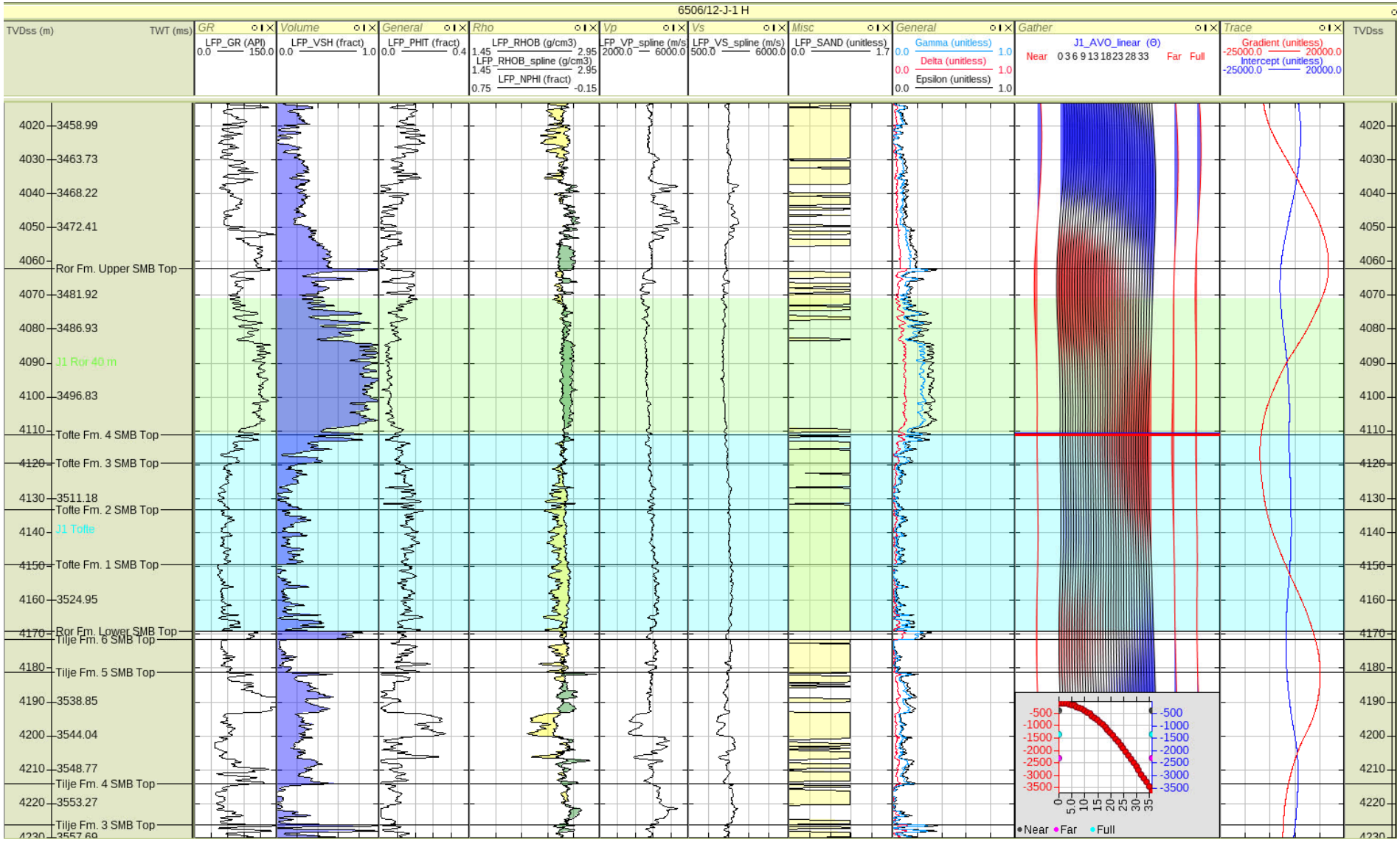

Figure 3.3: A snapshot from well 6506/12-J-1 H showing the Ror, Tofte and Tilje Formations. Well logs from left to right: Gamma ray (GR), Shale volume (V_{SH}), Bulk density, Neutron porosity, P-wave velocity, S-wave velocity, Sand flag, Anisotropy parameters (γ, δ and ϵ), AVO forward modelling (Shuey equation) gather using a wavelet extracted from the seismic data set for effective angle 24°, Gradient and Intercept measurements of the AVO gather.

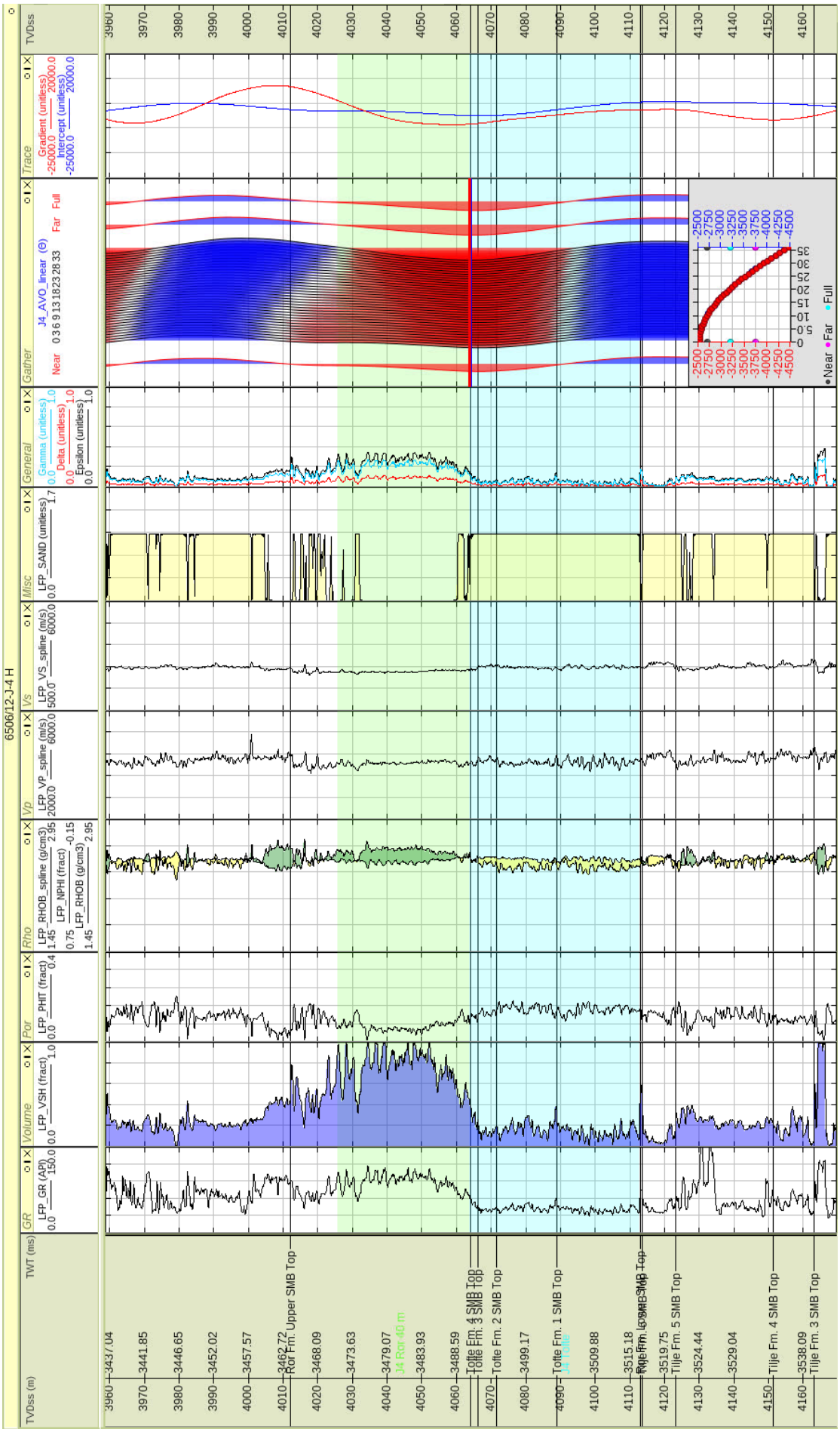

Figure 3.4: A snapshot from well 6506/12-J-4 H showing the Ror, Tofte and Tilje Formations. Well logs from left to right: Gamma ray (GR), Shale volume (V_{SH}), Bulk density, Neutron porosity, P-wave velocity, S-wave velocity, Sand flag, Anisotropy parameters (γ, δ and ϵ), AVO forward modelling (Shuey equation) gather using a wavelet extracted from the seismic data set for effective angle 24°, Gradient and Intercept measurements of the AVO gather.

Chapter 4

Pre-stack, Multiple Cube and Critical Angle Evaluation

4.1 Pre-stack and multiple cube evaluation

An evaluation of pre-stack data in the data set 1.1 and the multiple cubes available in data set 1.2 is done to assess which angle angle cubes can be used in the thesis work, and which areas should be handled with care in the AVO analysis due to the possibility of residual multiple energy affecting the amplitudes.

4.1.1 Pre-stack evaluation

The pre-stack evaluation is done using two inlines, avoiding the righoles, in the area of interest indicated in Figure 3.1. The pre-stack gather which is used is the gather 1.3 with AVO angles added.

Figure 4.1 shows a section with two pre-stack gathers displayed. From looking at the pre-stack gather to the left, it appears that the top Tofte Formation reflector, and the reflectors below, are of good quality up to about $32 - 34°$. Studying the pre-stack gather to the right, it appears to be sufficient up to $34°$. The higher angle data appears noisy and of poor quality.

Figure 4.2 shows a section further north in the area of interest. Looking at this pre-stack gather the top Tofte reflector quality appears sufficient up to approximately $36 - 37°$.

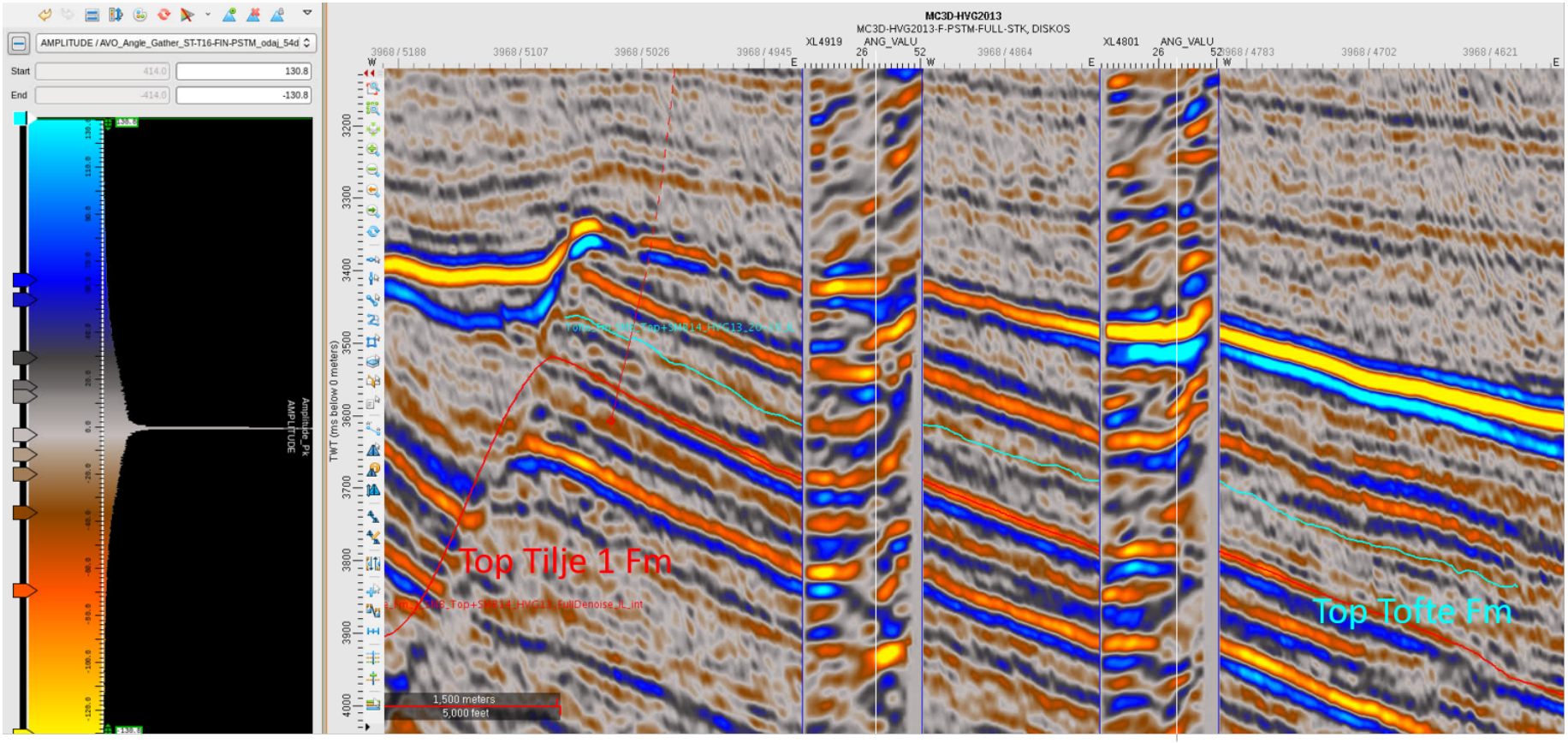

Figure 4.1: An inline section in the southern part of the target area from the seismic cube data set 1.1 full stack with two pre-stack gathers displayed. The angle range in each pre-stack gather increases from zero to 52° with an increment of 2.6°. The white lines indicates up to which angle range the data quality is sufficient, and in this case it appears that an upper limit can be set at 34°.

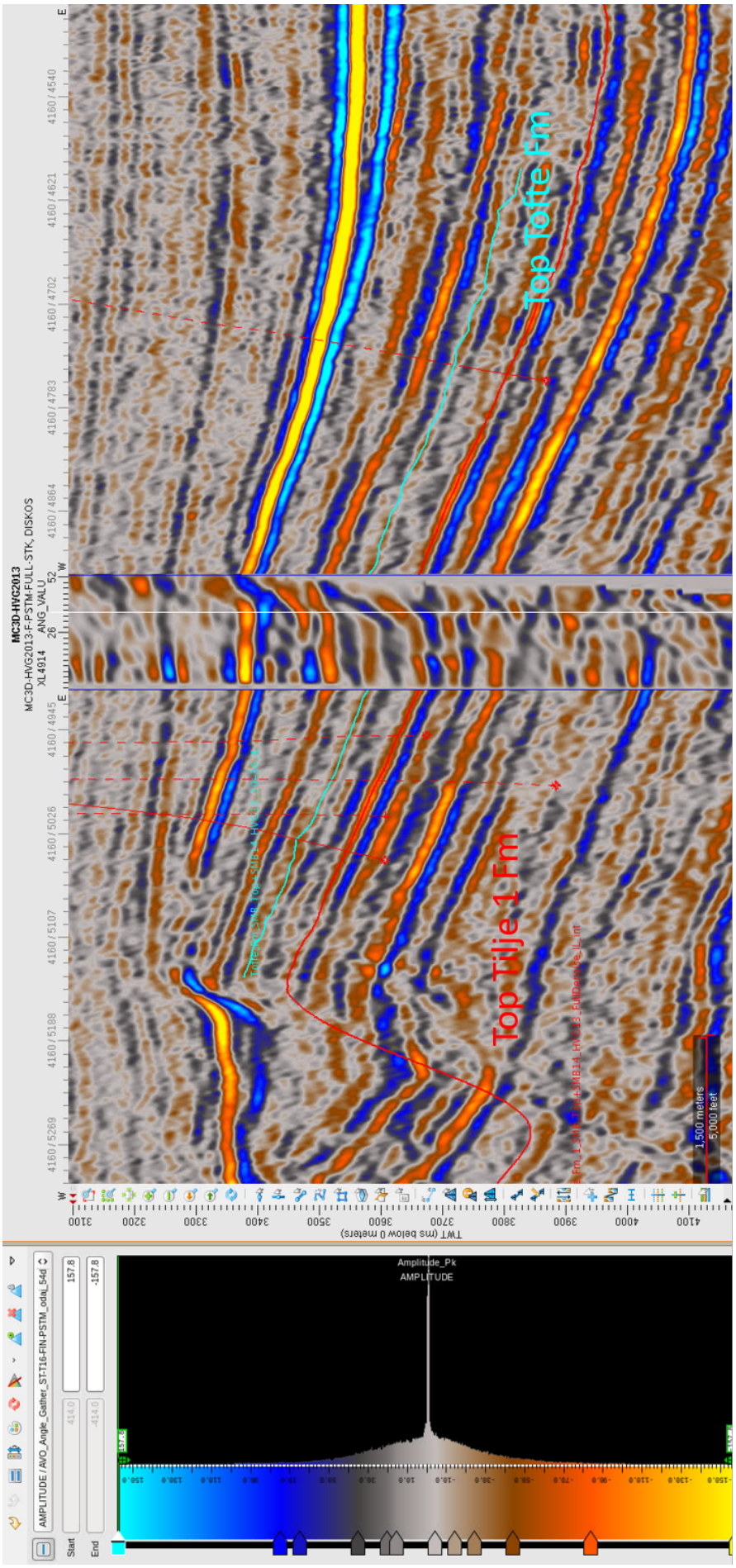

Figure 4.2: An inline section in the northern part of the target area from the seismic cube data set 1.1 full stack. The angle range in each pre-stack gather increases from zero to 52° with an increment of 2.6°. The white line indicates up to which angle range the data quality is sufficient, and in this case it appears that an upper limit can be set at 36°.

4.1.2 Evaluation of the multiple cubes

The multiple cubes, the data set 1.2.1-1.2.4, are the result of a multiple removal from the data set data set 1.2, and these cubes will be used to consider the residual multiple energy in the top Tofte Formation reflector. It is to be expected that multiple energy could still be present in the data set 1.1, but there does not exist an equivalent demultiple model for it, and thus the demultiple model from data set 1.2 is used as a substitution.

Preliminary multiple "polygons" have been created to be used together with the interpretation of the results, and can be seen in Figure 4.3. The areas which appear to contain multiple energy will only be comparable internally in the AVO analysis and cannot be compared to other areas. The multiple polygons are made by studying the multiple cubes in the area of interest (in the southern part that they cover) at the Tofte Formation interval. The study is done on an inline where the top Tofte Formation reflector has been interpreted, in between the two northernmost rig hole polygons. The set consists of three polygons created mainly considering the mid-range amplitude cube, seen in Figure 4.5.

Evaluation of the near angle multiple cube

An inline showing the near angle ($4 - 17°$) multiple cube together with the interpreted top Tofte and Tilje 1 reflectors is given in Figure 4.4. There is a lot of multiple energy present throughout the section. Looking at the top Tofte interpretation there appears to be residual multiple energy present in the top Tofte Formation reflector, and everywhere else in the cube. There is both negative (trough=red) and positive (peak=blue) energy present in the reflector, indicating that the energy belongs to different multiples. There is overall a lot of multiple energy present in the interval below the top Tofte reflector. On the basis of this examination, the near angle cube has been excluded as input in the AVO analysis.

Evaluation of the mid angle multiple cube

The mid angle cube contains visibly less multiples than the near cube, as expected, but there is still multiple energy present in the top Tofte reflector, as seen in Figure 4.5. There is in particular three or four areas which stand out, marked in Figure 4.5 by black arrows. Some areas appear to be free of multiples, and these are indicated by white arrows. It is evident from Figure 4.5 that most of the multiple energy is indicated by the black arrow number one and two from the left.

It appears that the multiple energy belongs to one multiple and not several, but this might simply be caused by the decreasing resolution with increasing offset.

Evaluation of the far angle multiple cube

The section showing an inline in the far angle multiple cube is shown in Figure 4.6. It is evident that the multiple energy contained in this cube is less than that of the near and mid angle cubes. There is little to no energy present in the top Tofte reflector in the left part of the section, and some multiple energy in the right part, represented by the two rightmost black arrows in Figure 4.6.

There appears to be little trouble in using the far angle cubes as input in the AVO analysis on the basis of the residual multiple energy in them. The two rightmost arrows indicate the same residual energy as seen in the mid angle cube in Figure 4.5. The residual energy present on the left side of the section in the mid angle cube appears to be almost gone.

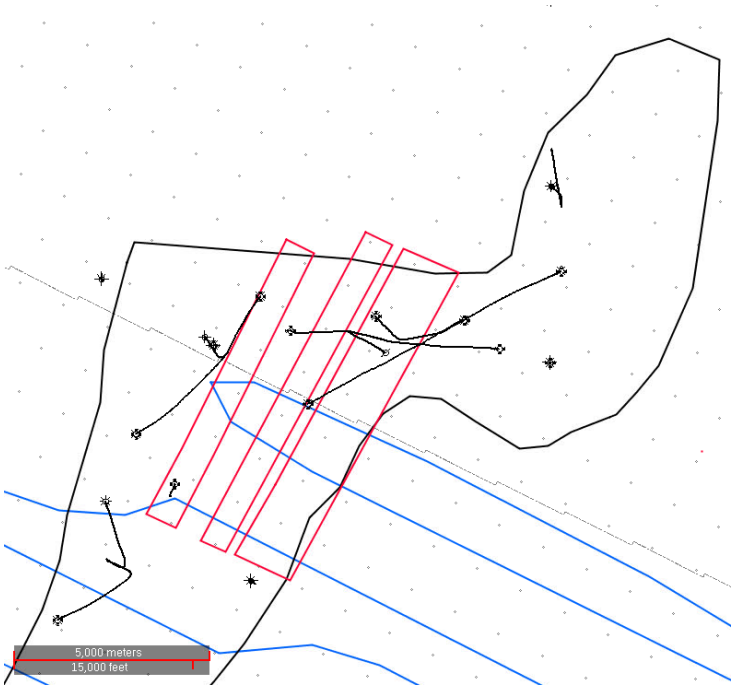

Figure 4.3: A close up of the target in the Smørbukk Field. The multiple polygons are shown in red, the LFP wells in black, and the rig hole polygons in blue.

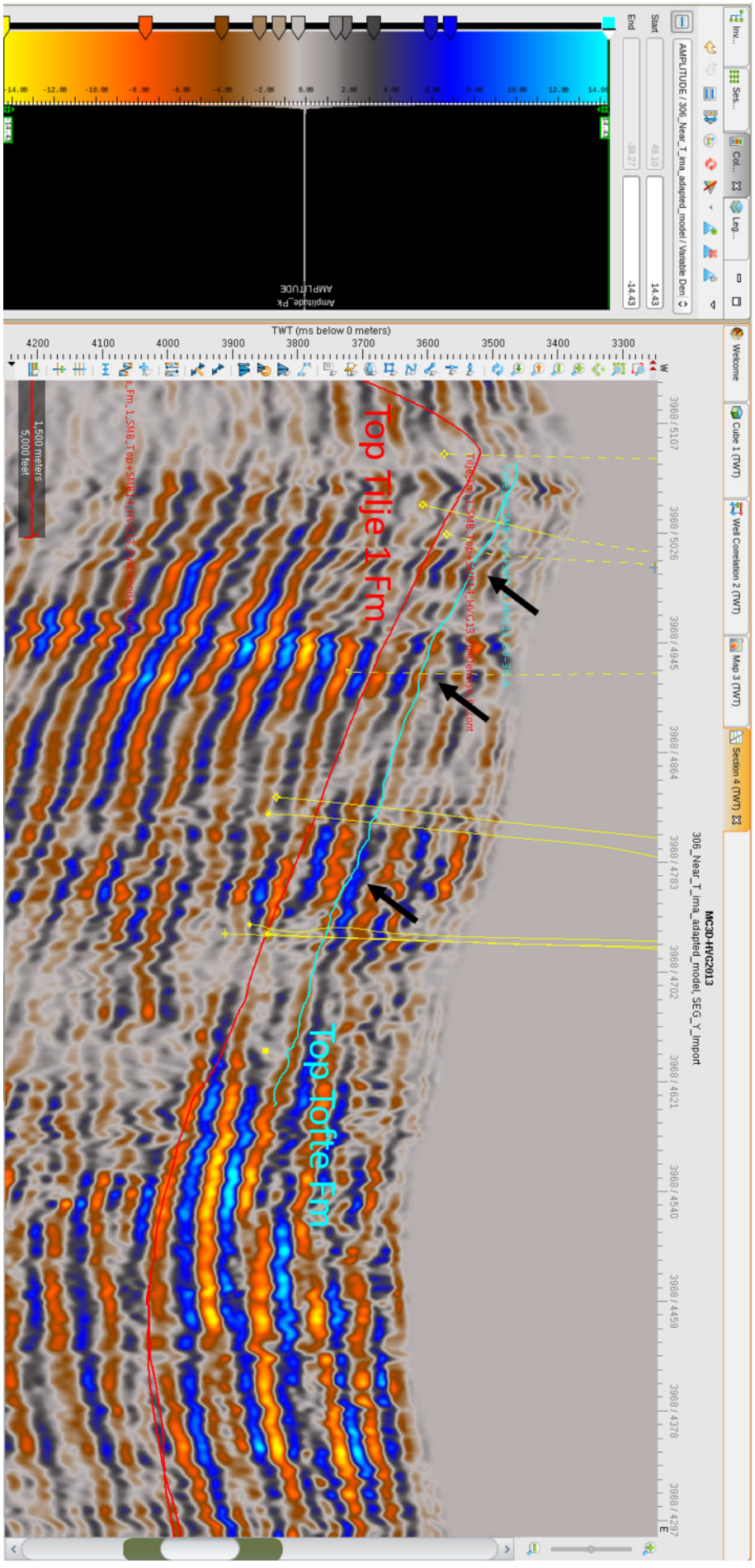

Figure 4.4: An inline section in the southern part of the target area from the seismic cube 1.2.1. Multiple energy is present in much of the inline section, and both positive and negative multiple energy is present in the top Tofte reflector, as indicated by the black arrows. There appears to be multiple energy present throughout the reflector, and in the reflectors below it, and thus the near-angles are excluded as input in the AVO analysis.

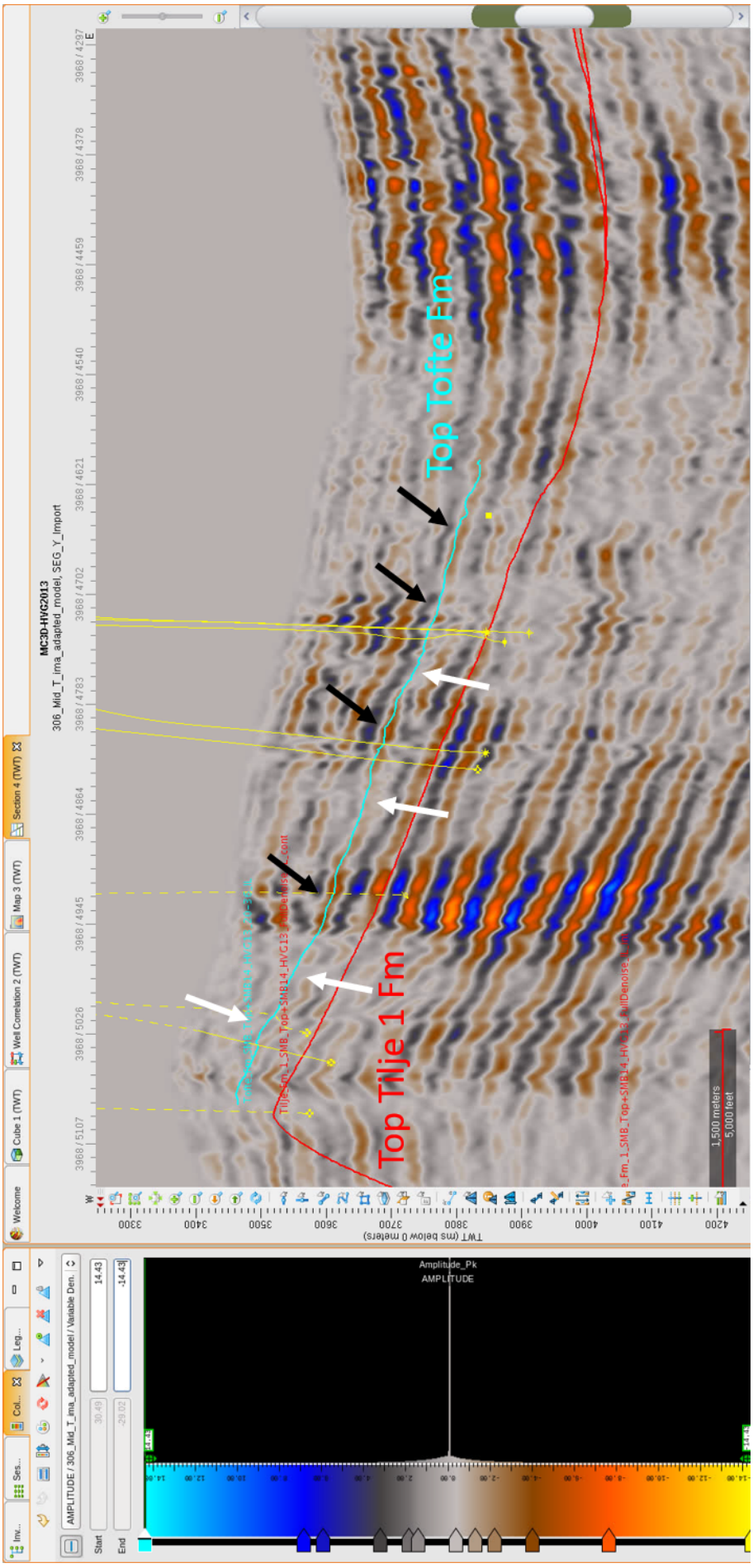

Figure 4.5: An inline section in the southern part of the target area from the seismic cube 1.2.2. In comparison to the near angle cube, there is less multiple energy present in the mid angle cube. The black arrows indicate residual multiple energy in the top Tofte reflector, and the white arrows indicate areas with little multiple energy present. This is the basis for the multiple polygons made to aid in the interpretation of the results.

Figure 4.6: section in the southern part of the target area from the seismic cube 1.2.3. As expected the far angle cube contains less multiple energy than the mid and near angles. The black arrows indicate residual multiple energy in the top Tofte reflector, and the white arrows indicates the areas where little to no multiple energy is present.

4.2 Critical angle estimation

The critical angle at the Upper Ror and Tofte Formation interface can be calculated for the isotropic case using Equation 2.5. Well 6506/12-J-1 H has good pressure sonic (DT) log data, and has been used for this purpose. The input P-wave velocities have been averaged 40 meters above and below the interface.

Table 4.1: Isotropic critical angle estimation

	Input velocities		
Well	$\overline{V_{p,1}}$	$\overline{V_{p,2}}$	Critical angle, ϕ_{crit}
6506/12-J-1 H	4117 m/s	4324 m/s	72.2 °

Because there is little difference in the P-wave velocity between the formations (the interface is visible due to the contrast in shear velocity, not the P-wave velocity), it appears there is no need to worry about having critical or near-critical energy in the data set for the top Tofte Formation reflector.

Chapter 5

Estimation of the Anisotropy Effect

5.1 Modelling of the anisotropy effect on the P-wave reflection coefficient

The anisotropy effect on the top Tofte Formation reflector is estimated by modelling the reflectivity response for the isotropic and anisotropic case for the Upper Ror-Tofte Formation interface. The work flow followed is shown below. RokDoc (version 6.6.1.133) is used to calculate the anisotropy logs, and MATLAB (version R2017b) is used for the reflection coefficient modelling.

Work flow for estimating the anisotropy effect

- Choose a vertical well with well log data of good quality to use as input in the modelling
- Calculate the Thomsen (1986) anisotropy parameters logs in RokDoc
- Model the reflectivity response assuming isotropic media using the Aki and Richards (1980) approximation
- Model the reflectivity response in VTI media including the anisotropy effect using the Rüger (1997) approximation
- Compare the responses by calculating the relative change in reflectivity. Is the anisotropy effect significant, and if yes, at which angles?
- If necessary, remove the anisotropy effect where it is of significance

5.1.1 Anisotropy parameter estimation

Two wells are used for the estimation of the anisotropy parameters. Well 6506/12-J-1 H is a near-vertical production well with good well log data. An exploration well, 6506/12-1, has also been included in the anistropy parameter estimation as a quality control. The wells were chosen to estimate the anisotropy parameters because they are located in the area of interest, the Tofte Formation is of high net-to-gross ratio in both wells, and the quality of the well log data is good. It should be noted that well 6506/12-1 has a synthetic shear sonic log, but of good quality. The well sections can be seen in Figure 3.2-3.3.

The Thomsen (1986) anisotropy parameters that are needed for the Rüger (1997) modelling of the P-wave reflection coefficient are ϵ and δ. Since there are no direct measurements of these anisotropy parameters available, the empirical relation created by Li (2006) will be used to estimate them. The empirical relationship created by Li (2006) requires the velocities parallel to the axis of symmetry of the VTI medium and the clay volume of each formation as input. The input well logs and constant values are given in Table 5.1.

Table 5.1: Input to the anisotropy parameter estimation

	Well log input			Constant values	
Well	$V_p, 0$	$V_s, 0$	V_{SH}	$V_{p,quartz}$	$V_{p,water}$
6506/12-J-1 H	LFP_VP	LFP_VS	LFP_VSH	6050 m/s	1500 m/s
6506/12-1	LFP_VP	LFP_VS	LFP_VSH	6050 m/s	1500 m/s

Unfortunately, there are no clay volume log available, and this input is approximated by the LFP_VSH curve. The LFP_VSH curve in well 6506/12-J-1 H is estimated from the gamma ray (GR) log, while the estimation of the shale volume curve for 6506/12-1 is unknown, as it has a different shale volume estimation than the current LFP analysis.

The anisotropy parameter logs for ϵ, γ and δ are calculated in RokDoc using Equation 2.78-2.80, and can be seen together with the other well logs in Figure 3.2 and 3.3 in number track eight. The calculated average anisotropy parameters are given in Table 5.2. The parameters presented in the table represent an interval in the Upper Ror and Tofte Formations 40 meters above and below the interface between them, respectively.

Table 5.2: Calculated anisotropy parameters for the Ror and Tofte Fm

Well	Tofte Fm			Upper Ror Fm		
	$\overline{\epsilon}$	$\overline{\gamma}$	$\overline{\delta}$	$\overline{\epsilon}$	$\overline{\gamma}$	$\overline{\delta}$
6506/12-J-1 H	0.072	0.058	0.023	0.263	0.206	0.084
6506/12-1	0.063	0.044	0.02	0.245	0.13	0.078

5.1.2 Reflection coefficient modelling

The reflection coefficient is modelled using two approximations to the Zoeppritz (1919) equations with input values from well 6506/12-J-1 H. The first approximation is that of Aki and Richards (1980) assuming isotropy, given in Equation 2.9, while the second is that of Rüger (1997), given in Equation 2.72, where the anisotropy is taken into account.

The values calculated for ϵ, given in Table 5.2, indicate that the anisotropy in the Upper Ror Formation is not weak. The Rüger (1997) approximation is still used to model the effect, seeing that the parameter epsilon, ϵ, is not much higher than 0.2, and that the Tofte Formation also has a minor contribution of anisotropy. The input parameters used as constants in the reflection coefficient modelling is given in Table 5.3.

Table 5.3: 6506/J-1 H reflection coefficient modelling input parameters

Formation	$\overline{V_{P,0}}$ (m/s)	$\overline{V_{S,0}}$ (m/s)	$\overline{\rho}$ (kg/m^3)	$\overline{\epsilon}$	$\overline{\delta}$
Ror	4117	2444	2598	0.263	0.084
Tofte	4324	2704	2465	0.073	0.023

5.1.3 Removal of the anisotropy effect

A scheme to remove potential anisotropy effects has been included, and the MATLAB code is given in Appendix B. The work flow is very similar to that of the detuning work flow described in Section 6.3. Anisotropy effects can be removed by multiplying an amplitude map by the factor (1 - anisotropy effect), where the anisotropy effect is defined as the relative change in amplitude from the anisotropic to the isotropic case, as given in Equation 2.77.

5.2 The results of the anisotropy effect investigation

5.2.1 Resulting anisotropy parameters

The results of the anisotropy parameter estimation are given in Table 5.2. The anisotropy well log curves can be seen in Figure 3.2 and 3.3. Studying the estimated ϵ in the Upper Ror Formation, it is evident that it appears not to be weak, as it is higher than the limit for weak anisotropy (Thomsen, 1986). The anisotropy is slightly smaller in well 6506/12-1 compared to 6506/12-J-1 H for the Upper Ror Formation, which might show that the latter has some deviation in the target interval. The parameter δ appears to be weak, which is the parameter with the greatest impact on the anisotropy for near vertical angles of incidence.

Some possible sources of error have to be considered here when using the Li (2006) empirical relationships. The wells may not be perpendicular to the bedding, and the LFP_VSH curve may not be fully representative of the clay volume. It could be assumed that using the shale volume as input will yield too high estimates for the anistropy parameters, as the silt and mud-sized particles are also included in the volume fraction. However, these estimates are still used as input in the reflection coefficient modelling, as the well log curves are considered to be sufficient to use as input.

5.2.2 The modelled anisotropy effect

The results of the reflection coefficient modelling are shown in Figure 5.1. It is evident that for up to an incident angle of about 30°, there appears to be little to no anisotropy effect which can affect the data.

It can be observed that the anisotropy effect at the Upper Ror-Tofte Formation interface has a more or less positive contribution to the absolute reflection coefficient, growing larger with increasing offset. The anisotropy effect adds constructively to the negative P-wave reflection coefficient, just like the expected tuning effects.

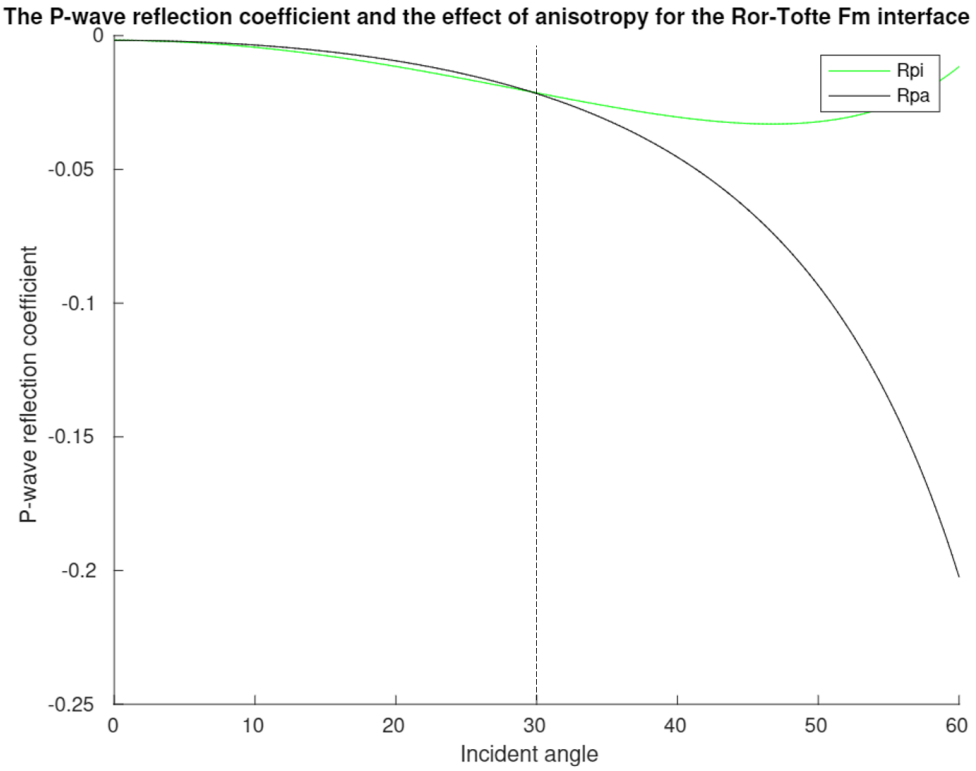

Figure 5.1: The modelling of the isotropic and the anisotropic reflection coefficient. R_{pi} represents the isotropic case, while R_{pa} represents the anisotropic case.

The expected anisotropy effect, as given in Equation 2.77, is given in Table 5.4 for the effective

angle of the mid and far angle cubes. At an effective angle of 48° there is an approximately 10% increase in the absolute amplitude value, while at 32° there is less than a 5% increase. Thus it is concluded that the anisotropy effect does not require any corrections in the angle range which is used as input in the AVO analysis (12 – 36°).

Table 5.4: Estimated ansiotropy effect

Effective angle	Anisotropy effect (relative change in R_p)
24	0.0261
32	0.0458
40	0.0689
48	0.0940

Chapter 6

Evaluation of Tuning Effects and the Following Detuning Scheme

6.1 Extraction of input data

The necessary input for the evaluation of the tuning effect and the subsequent detuning process is a thickness map, the tuning curves and the amplitude maps which are to be detuned. The thickness map and the amplitude maps are created in, and exported from, DecisionSpace GeoScience (version 10ep.3.05.5), in short DSG. The workflow followed is as listed below.

workflow for creating and exporting thickness and amplitude maps in DSG

- Create the Tofte Formation thickness map
- Extract amplitudes from each angle cube for the top Tofte Formation reflector to create the amplitude maps
- Export the maps from DSG in .xyz or .txt format.

The extraction of the thickness and amplitude maps is limited by three polygons, shown in Figure 6.1, which exclude bad data near the Smørbukk Fault and interpolation of the Tofte Formation interpretation outside of the Smørbukk Field.

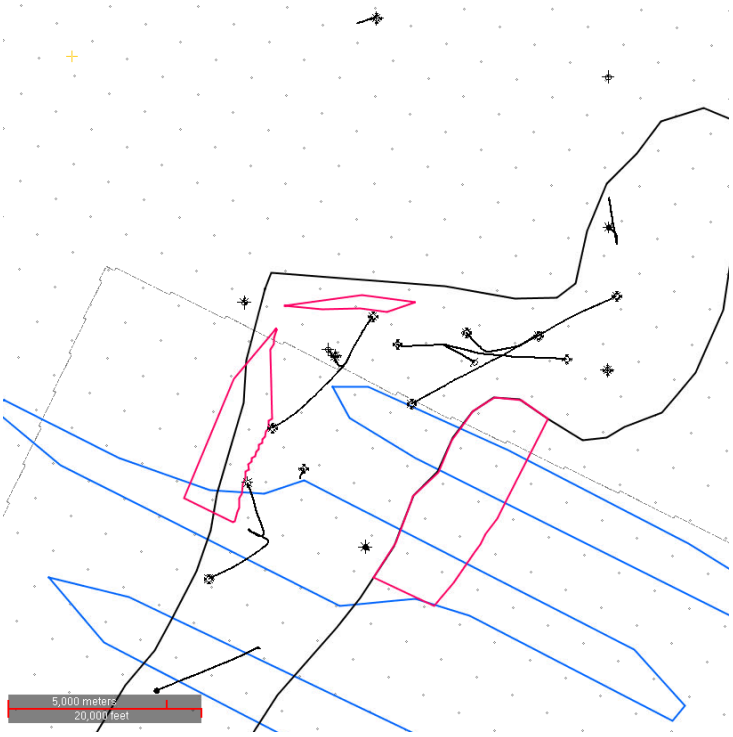

Figure 6.1: A close up of the target area in the Smørbukk Field. The bad data polygons used to remove anomalous data points in the amplitude and thickness maps are shown in pink.

6.1.1 Thickness map of the Tofte Formation

The first step is to create a time thickness (TWT) map of the Tofte Formation. The map was created using the calculator function in DSG by applying the basic vertical travel time equation to calculate the depth in TWT from the top Tofte reflector down to the base of the formation. To create this map it was assumed that the velocity is constant in the Tofte Formation and down to the Tilje 1 Formation.

The input was the interpolated interpretation of the top Tofte and the the top Tilje 1 reflectors, both in TWT, combined with surfaces from the Smørbukk geomodel in TVDss. The input used to create the thickness map is given in Table 6.1.

Table 6.1: Input in the estimation of the thickness map of the Tofte Formation

Geomodel surface (TVDss)	Interpolated interpretation (TWT)
Top Tofte	Top Tofte
Top Tilje 1	Top Tilje 1
Top Tilje 6	-

Figure 6.3 shows how the thickness varies across the northern part of the Smørbukk Field. In the north-west the thickness varies from 25-30 ms, and towards the south-east it increases. In Figure

4.1 and 4.2 it can be seen that the sedimentary package between the Tofte and Tilje Formation reflector appears to thicken. The thickness map of the Tofte Formation created from well log data, found in Figure A.1 also show same trend when the local minima are not considered. It appears that the thickness map is sufficient to use in the following detuning scheme.

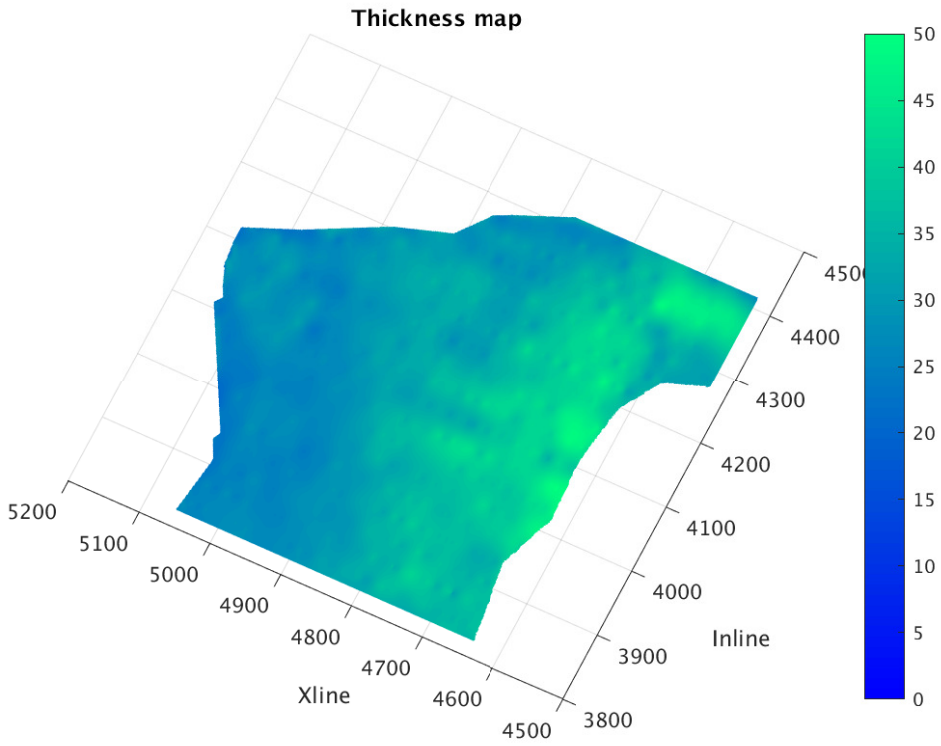

Figure 6.2: The thickness map (ms) of the Tofte Formation in the northern part of the Smørbukk Field.

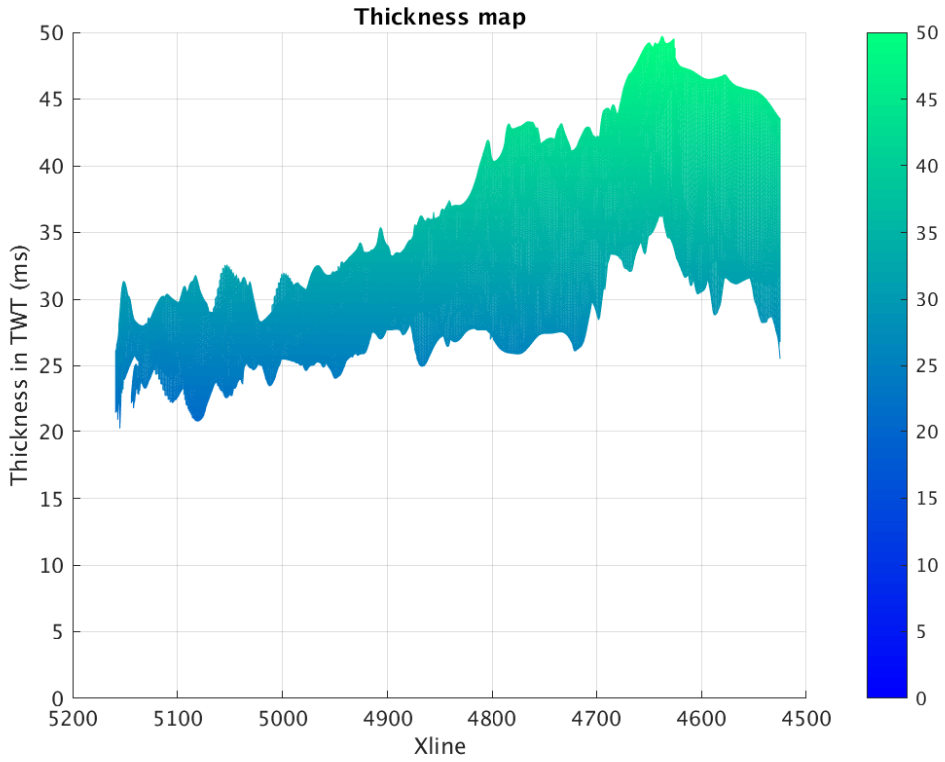

Figure 6.3: The thickness map (ms) of the Tofte Formation in the northern part of the Smørbukk Field, shown varying with crosslines.

6.1.2 Extraction of amplitude maps

The amplitudes are extracted in CDG from each of the angle cubes. The minimum amplitude is extracted in each inline and crossline point for a window (-15 ms to + 15 ms) centered at the interpolated interpretation of the top Tofte Formation. Any positive amplitudes which were extracted are set equal to zero, as it is assumed that these amplitudes have been picked erroneously, or have been picked in areas where the Tofte Formation reflector is either weak or missing.

6.2 Wedge modelling: Evaluation of tuning effects

The tuning effects were evaluated through the creation of wedge models in RokDoc (Version 6.6.1.133), following the workflow given below. The resulting wedge models, tuning curves and wavelets are presented later in the chapter. The wedge modelling was done using well 6506/12-J-4 H as input for the constant layer properties, given in Table 6.2. In this well the Tofte Formation is overlain by the Upper Ror Formation, and underlain by a thin layer of the Lower

Ror Formation, which lies directly above the Tilje Formation. The 6506/12-J-4 H well section in the target zone can be seen in Figure 3.4.

For the purpose of this analysis wedge models and tuning curves have been created for all of the available angle cubes (excluding the ultra far cube) in order to assess the overall development of the tuning effects for the top Tofte Formation reflector. Only the top reflector is considered, as there is not an existing interpretation of the top Lower Ror or Tilje Formation in the area of interest.

It is important to note that these wedge models have been created for high net-to-gross values in the Tofte Formation in order to assess the maximum expected tuning effects. For lower values of net-to-gross the amplitude response between the Upper Ror Formation and the Tofte Formation will be reduced, and the tuning effects will be different, and are assumed to decrease. The tuning effects will also depend on the shalyness of the Lower Ror and Tilje Formations which influence the base reflector response. Thus this is a simplified analysis, but were the Tofte Formation is very shaly, it is also likely that no tuning effects exist as the distinction between the Upper Ror and the Tofte Formation will be marginal.

Workflow for tuning effect evaluation

- Import the necessary well log data. The well chosen for the wedge modelling should have a high N/G in the Tofte Formation.
- Import the wavelets belonging to each angle cube which is to be used in the analysis.
- Create working intervals of 40 meters above and below the Tofte Formation, and a working interval in the Tofte Formation itself.
- Make average sets of the P-wave velocity, S-wave velocity and density from the working intervals.
- Create a wedge model with constant input values for the P-wave velocity, S-wave velocity and density, along with the zero phase wavelets extracted from each cube. The Tofte Formation makes up the wedge, while the Upper Ror Formation lies above. Directly below either the Lower Ror Formation or the Tilje Formation is found, depending on which well is used.
- The synthetic wedge model is calculated using the Zoeppritz (1919) equations for each effective angle, using the constant input values and the wavelet extracted from each angle cube.
- Measure the tuning curve values in RokDoc by tracking the amplitudes at the top of the model.
- Extract the tuning curve from RokDoc in .xls and .xlsx format.
- Analyse the tuning curves. Determine the tuning effects and the tuning thickness. How do they vary with incidence angle?

The tuning effect is defined similarly to the the anisotropy effect, as the relative change from the stable amplitude to the tuning amplitude at tuning thickness, given in Equation 6.1. The stable amplitude is defined as the amplitude value for thicknesses higher than $\frac{\lambda}{2}$, and the tuning amplitude the amplitude value at tuning thickness $\frac{\lambda}{4}$.

$$\text{Relative change} = \frac{A_{\text{tuning}} - A_{\text{stable}}}{A_{\text{stable}}} \tag{6.1}$$

Table 6.2: 6506/12-J-4 H wedge model constant input

Layers	V_P (m/s)	V_S (m/s)	ρ (kg/m^2)
Upper Ror Fm	4070	2472	2581
Tofte Fm	4085	2660	2413
Lower Ror and Tilje Fm	4235	2722	2479

6.3 The detuning process

The detuning method chosen is based on the work of Brown et al. (1986) and Francis (2015), and is a detuning function as a function of layer thickness, as given in Equation 2.90.

The detuning process has been created as several functions in MATLAB, which can be found in Appendix B. The workflow followed by the MATLAB functions is given below. The functions are general and can be used for any input files with the format xyz., .txt, xls, or .xlsx, and any type of three-layer cases.

Modelling of tuning effects and the detuning scheme workflow in MATLAB

- amplitude_import.m and thickness_import.m: Import the thickness and amplitude maps (in .xyz or .txt format).
- tuning_import.m: Import the tuning curve data points (in .xls or .xlsx format).
- tuning_curve.m: Estimate the tuning curve as a polynomial.
- horizon_sorting.m: Sort the data points in the thickness and amplitude maps by inlines and crosslines.
- detuning.m: Create the tuning map by running the thickness map through the tuning curve, and the detuning map by dividing the amplitude value at a thickness unaffected by tuning by the tuning map. The next step is then to detune the input amplitude map by multiplying it with the detuning map.
- horizon_desorting.m and amplitude_export.m: Export the detuned amplitude map (in .xyz or .txt format) from MATLAB

6.4 Results of the tuning effect analysis

6.4.1 Estimated tuning effects and tuning thickness

The tuning effects for each effective angle is given below in Table 6.3. The tuning effects are constructive, and appear to decrease with increasing angle, with the highest modelled tuning effect being 25 % at an effective angle of 8°. The shape of the tuning curve is more or less unchanged with angle above tuning thickness, and so is the tuning thickness. The tuning curve is flat around the tuning thickness, before there is a sharp decline in amplitude strength. The decreasing tuning effect with increasing angle appears to be caused by the AVO behaviour of the top and base of the Tofte Formation, where the top reflector is of class 2n or 3, while the base reflector is of class 4. At low angles the weaker top reflector will be more affected by the interference of the side lobes of the base reflector than at higher angles.

The AVO attributes of the top reflector are expected to be affected by the tuning effects. The intercept is expected to be exaggerated where the Tofte Formation has a high net-to-gross ratio, and it appears that the varying tuning effect with angle can counteract the true gradient. It is expected that the effect of tuning on both AVO attributes will decrease with decreasing net-to-gross ratio.

Table 6.3: 6506/12-J-4 H estimated tuning effects

	Relative change in amplitude at tuning thickness	
Effective angle	Constant input of average values	Well log input
8	0.2446	0.234
16	0.1664	0.1574
24	0.1206	0.1132
32	0.852	0.805
40	0.786	0.756

For comparison both the measured relative change in amplitude for the simple wedge model with the constant layer properties, as shown in the figures below, and the relative change when using the well logs as input in the wedge model, are included in Table 6.3. There is not a significant difference in the estimated tuning effects, and it appears that it is sufficient to use the constant values to create the wedge models and the subsequent tuning curves.

The tuning thickness in each wedge model is given in Table 6.4. The average tuning thickness is approximately 37 ms, but it is evident that the decline in amplitude strength does not happen until the thickness is approximately 25-20 ms for all of the tuning curves. The average thickness of the thickness map is 33 ms. Thus we can conclude that the Tofte Formation is, for the most

part, at and above tuning thickness. The constructive tuning effects are present for the top Tofte Formation reflector in the northern part of the Smørbukk Field, and it is not expected to observe any destructive tuning effects based on the thickness map of the formation. The results are in agreement with what was found by Johannessen (2018).

Table 6.4: Estimated tuning thickness (ms) with varying incident angle

Effective angle	Tuning thickness (ms)
8	44.26
16	26.03
24	28.64
32	46.87
40	39.06
Average	36.97

6.4.2 Wedge model results

8 ° effective angle

The tuning curve created from the wedge model for an effective angle of 8° can be seen in Figure 6.4. The tuning thickness appears to be at 44 ms, but it can be seen that the destructive effects of tuning do not initiate until the thickness reaches 20-25 ms. As the thickness goes to zero the amplitude of the top reflector decreases sharply, and becomes slightly positive near zero thickness.

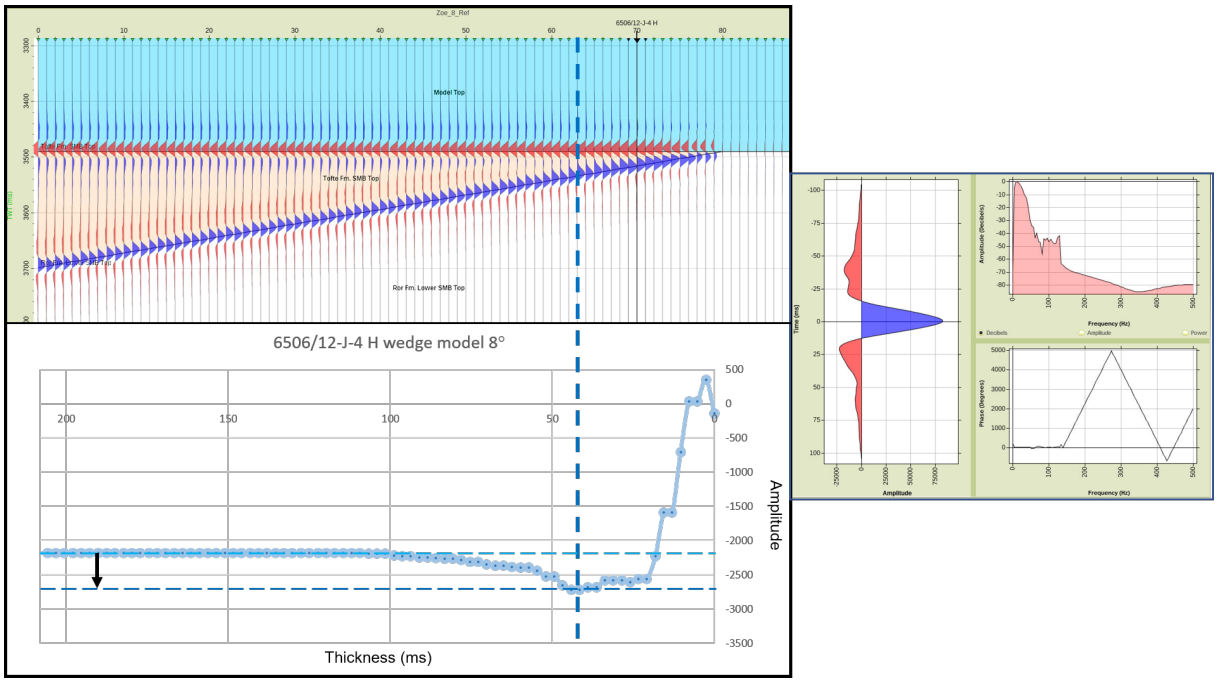

Figure 6.4: The wedge model, corresponding tuning curve and wavelet for cube 4 – 12°. In the tuning curve the stable amplitude is indicated by the light blue dotted line, the tuning amplitude by the dark blue dotted line, and the tuning effect by the black arrow.

16 ° effective angle

At 16° effective angle it can be seen that the tuning effect has decreased by approximately 10 %. The decreasing tuning effect is indicated by the now smaller black arrow in the tuning curve in Figure 6.5. The tuning curve is more flat than the curve derived for an effective angle of 8°, but the same shape and gradual increase in amplitude can be seen. The tuning thickness is here set at 26 ms.

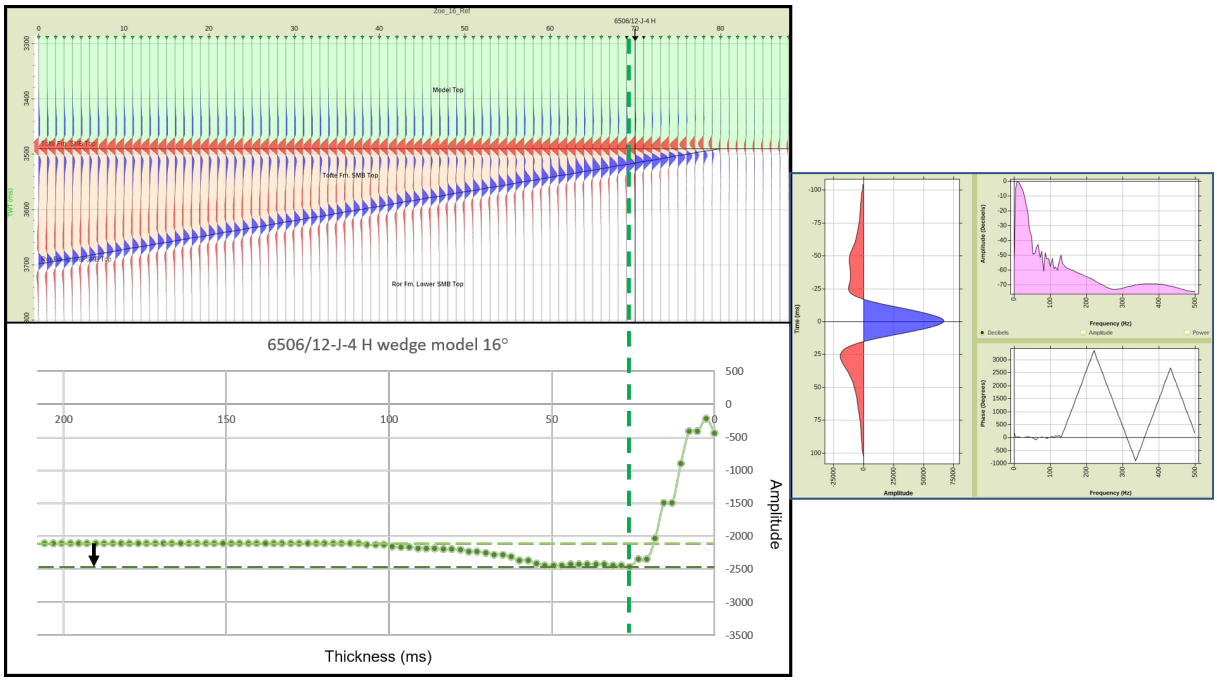

Figure 6.5: The wedge model, corresponding tuning curve and wavelet for cube 12 – 20°. In the tuning curve the stable amplitude is indicated by the light green dotted line, the tuning amplitude by the dark green dotted line, and the tuning effect by the black arrow.

24 ° effective angle

Moving on to the wedge model and the tuning curve extracted for an effective angle of 24° in Figure 6.6, the tuning curve looks the same as the two previous curves, with the exception of a smaller tuning effect and a less sharp decrease of amplitude for thicknesses below the "effective" tuning thickness. The tuning thickness has been set at approximately 28 ms.

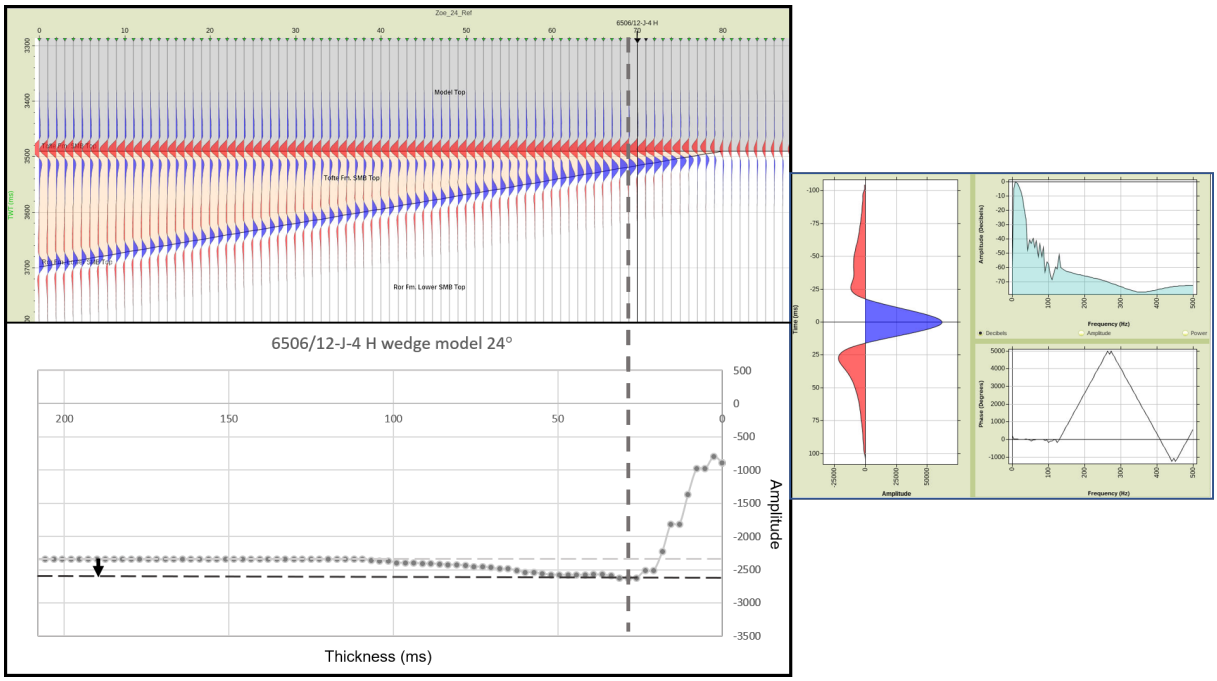

Figure 6.6: The wedge model, corresponding tuning curve and wavelet for cube 20 – 28°. In the tuning curve the stable amplitude is indicated by the light grey dotted line, the tuning amplitude by the dark grey dotted line, and the tuning effect by the black arrow.

32 ° and 40 ° effective angle

The 32° and 40° effective angle tuning curves look very similar to the 24° curve, with decreasingly destructive tuning effects below tuning thickness, and a decreasing tuning effect. The tuning thickness are set at 47 and 39 ms, respectively, but they have the same "effective" tuning thickness, just like the rest of the curves. The tuning effect is not decreasing as rapidly as at lower angles, and at 32° and 40° the tuning effect is estimated to be below 10 %, and thus more or less insignificant.

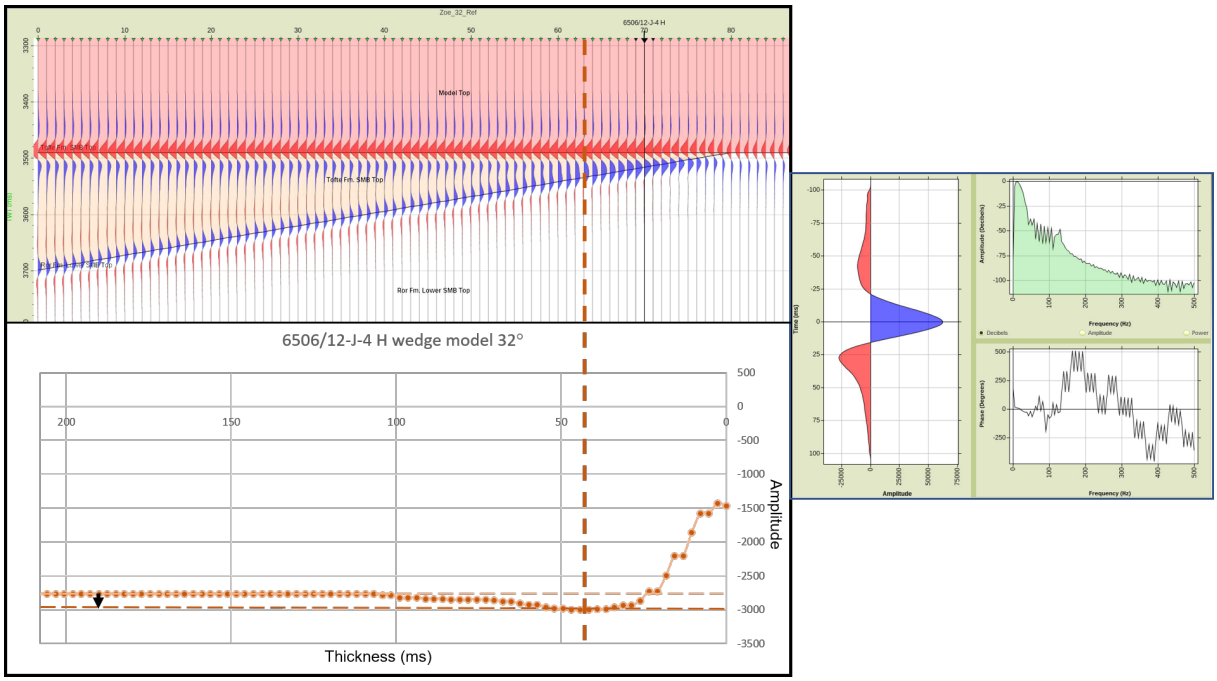

Figure 6.7: The wedge model, corresponding tuning curve and wavelet for cube 28 – 32°. In the tuning curve the stable amplitude is indicated by the light orange dotted line, the tuning amplitude by the dark orange dotted line, and the tuning effect by the black arrow.

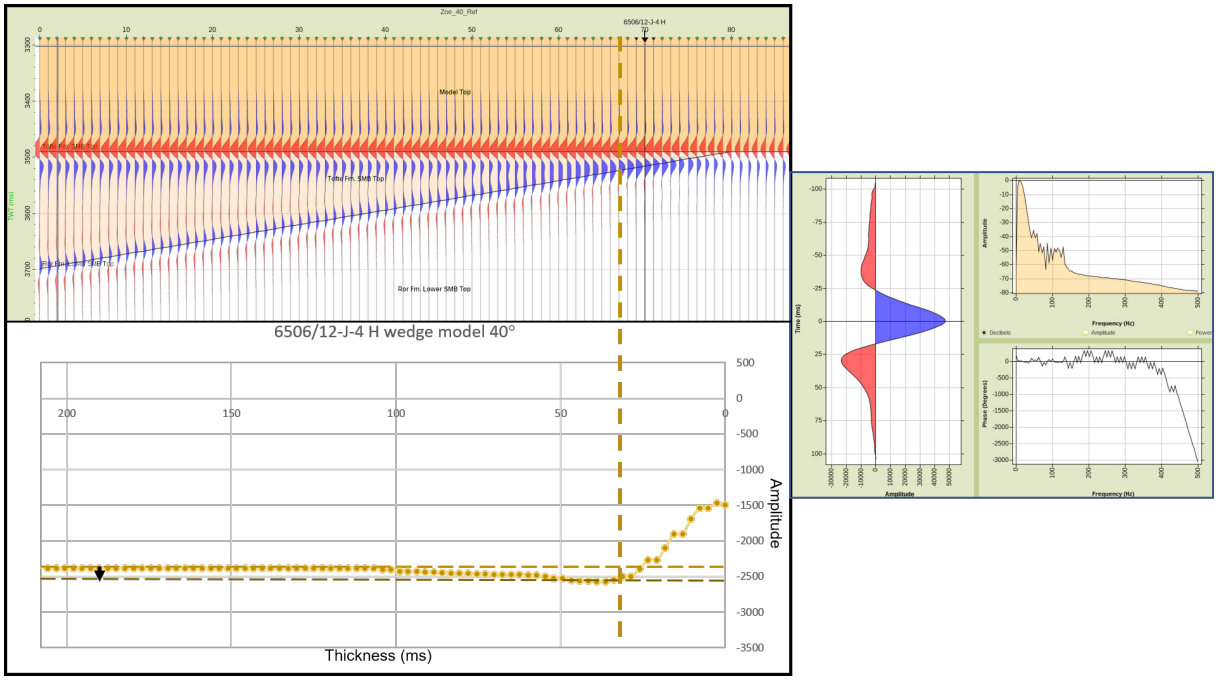

Figure 6.8: The wedge model, corresponding tuning curve and wavelet for cube 36 – 44°. In the tuning curve the stable amplitude is indicated by the light yellow dotted line, the tuning amplitude by the dark yellow dotted line, and the tuning effect by the black arrow.

Comparison of the tuning curves

Figure 6.9 shows all of the tuning curves plotted together for each respective effective angle. The tuning curves for effective angles 8° and 16° go down towards zero as the thickness goes to zero, while the rest of the tuning curves at increasing effective angles go down to less negative values, and are not completely destructive.

Looking at how the amplitudes are affected by the varying tuning effects, it is also important to consider how the AVO attributes will be affected with these tuned amplitude responses used as input to create them. When studying Figure 6.9 it appears that the amplitude value for 8° effective angle is higher than the amplitude values at 16° and 24°, and when following each stable value in towards the tuning thickness, it is apparent that the relationship between the curves changes. Thus it is likely that the AVO intercept will become increasingly negative with thicknesses in towards the tuning thickness, and that the AVO gradient will become less negative at tuning thickness, possibly changing the AVO class response.

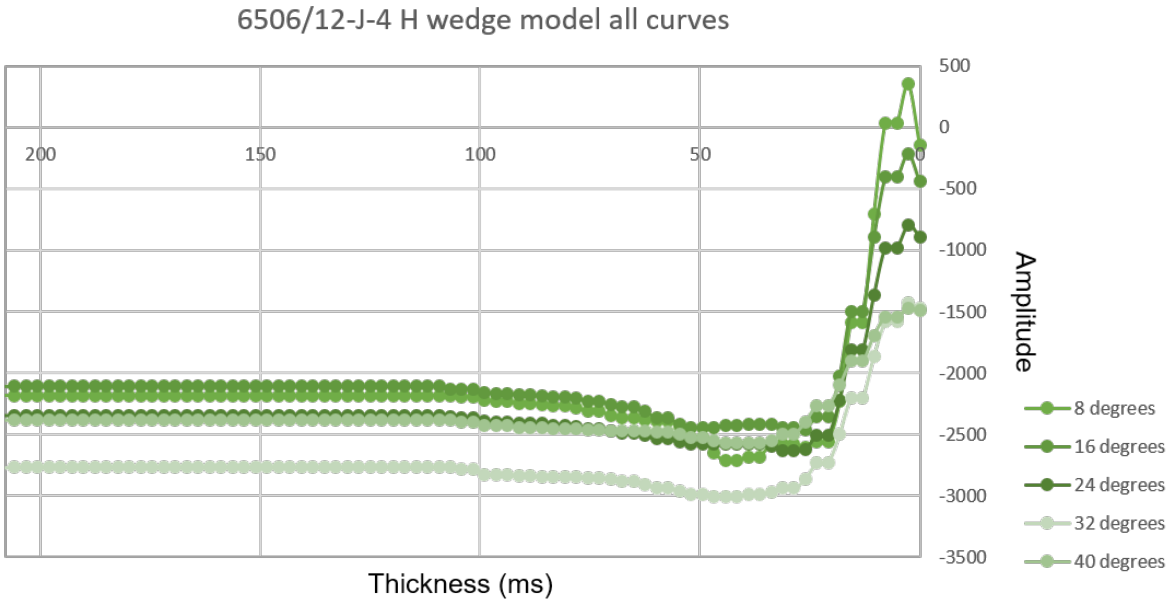

Figure 6.9: A plot with all the tuning curves at each effective angle.

6.5 Results of the detuning process

The input amplitude maps and the resulting detuned amplitude maps are shown in Figure 6.10-6.17 below.

The analysis of the tuning effects revealed that the expected tuning effect at the angle range from 12° to 36° ranges from approximately 16% to 8%. Even though these tuning effects are not necessarily very high, they appear to affect the AVO attributes. If the tuning effects are not removed properly from the amplitude maps, these effects will transfer to the AVO attributes, and further affect the net-to-gross inversion.

Since the Tofte Formation appears to be of thicknesses at and close to the tuning thickness, and the tuning curve is relatively flat around the tuning thickness, an overall reduction in amplitude is seen in each of the detuned amplitude maps. Then biggest effect of the detuning is seen for the $12 - 20°$ amplitude map in Figure 6.10 and 6.11.

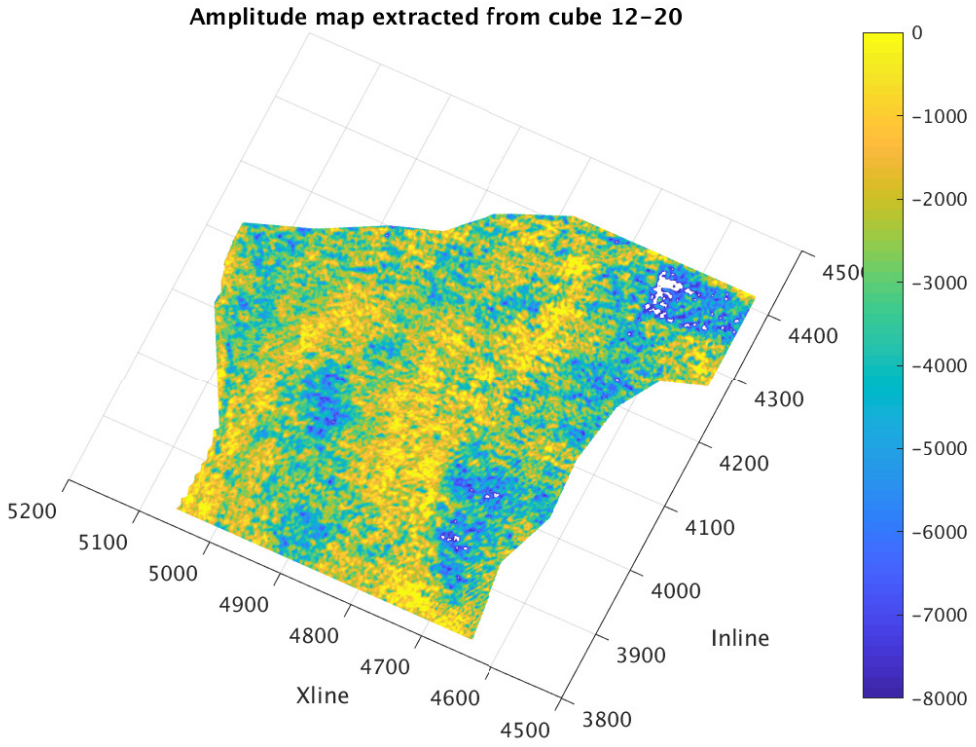

(a) Prior to detuning

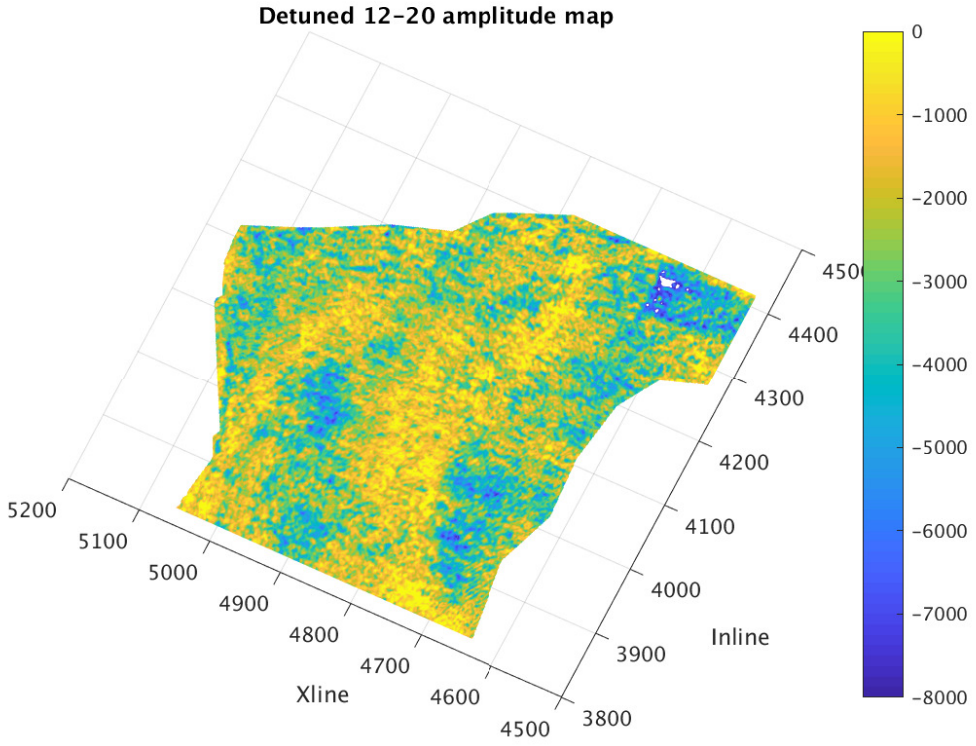

(b) After detuning

Figure 6.10: Detuning results of the top Tofte Formation amplitude map for the angle range of 12 – 20°.

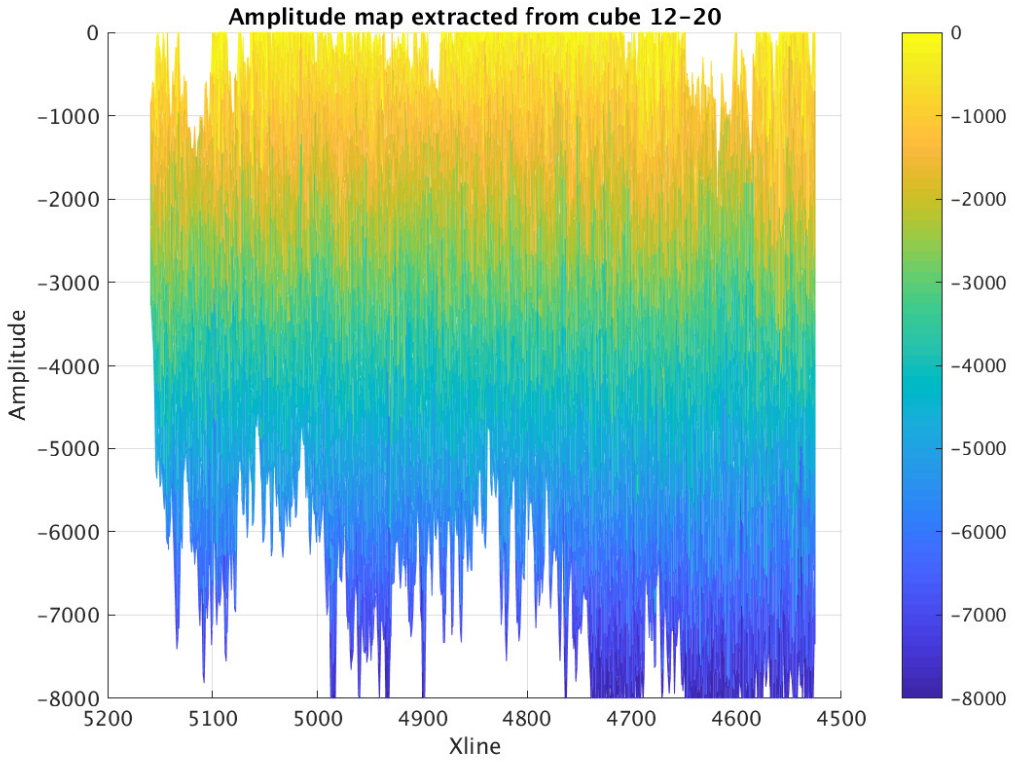

(a) Prior to detuning

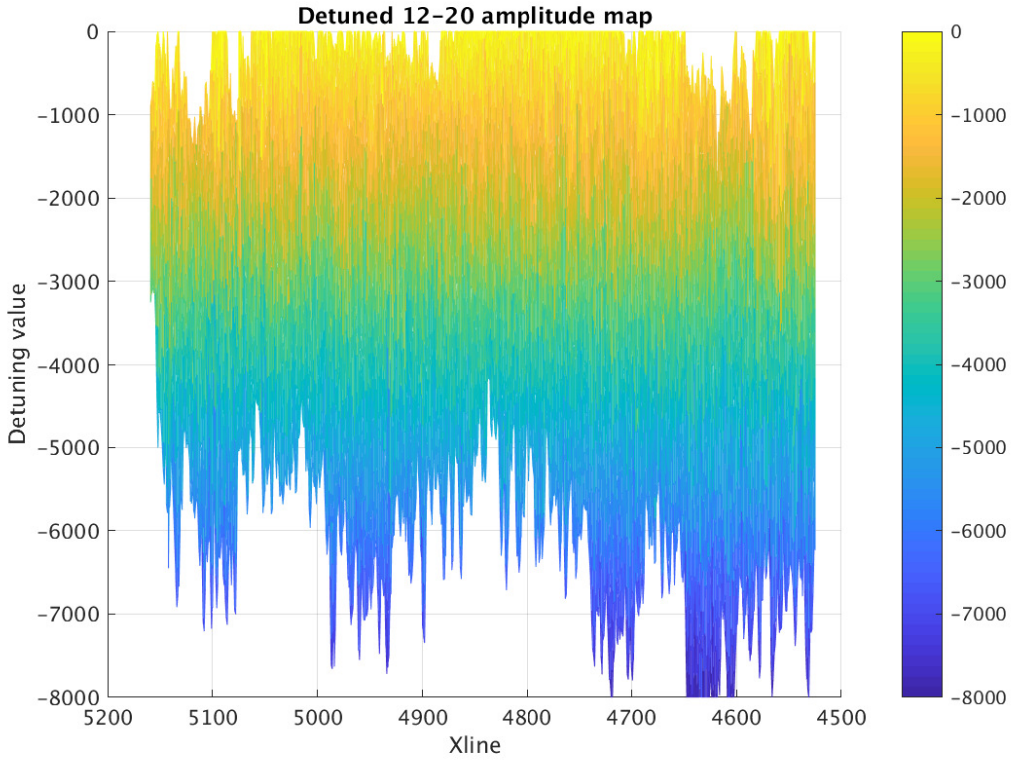

(b) After detuning

Figure 6.11: Detuning results of the top Tofte Formation amplitude map for the angle range of $12 - 20°$ shown for crosslines.

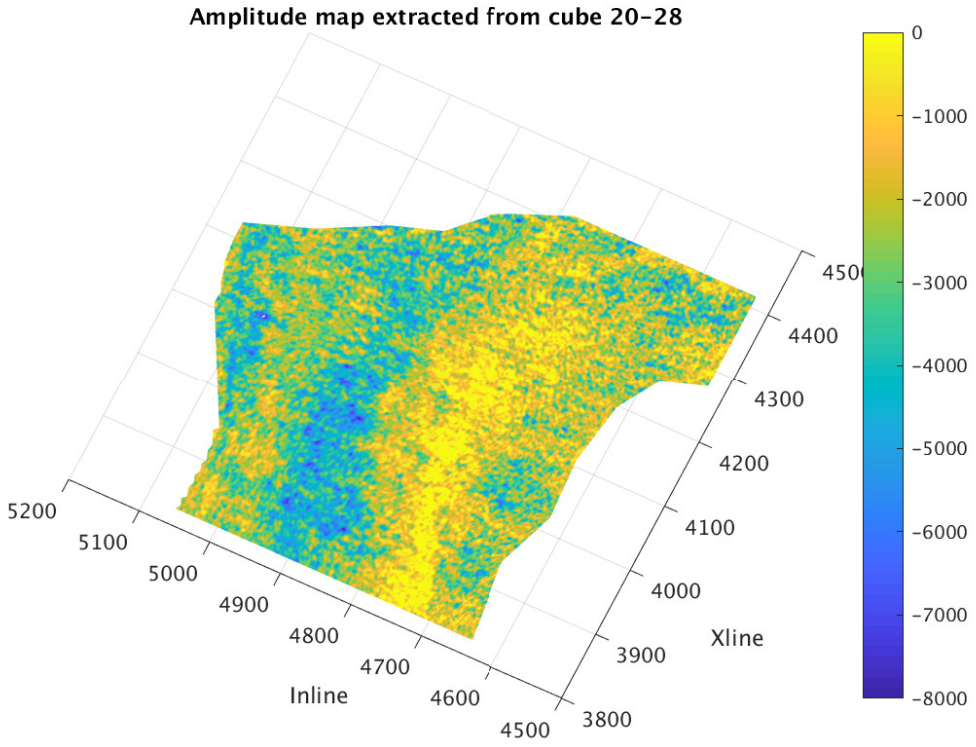

(a) Prior to detuning

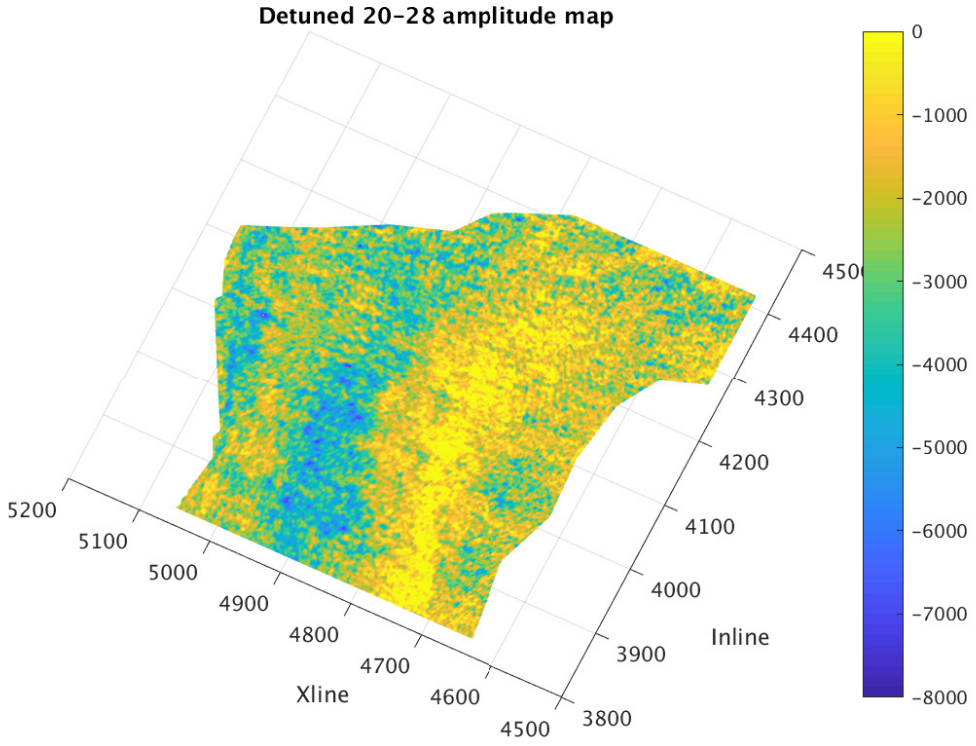

(b) After detuning

Figure 6.12: Detuning results of the top Tofte Formation amplitude map for the angle range of 20 – 28°.

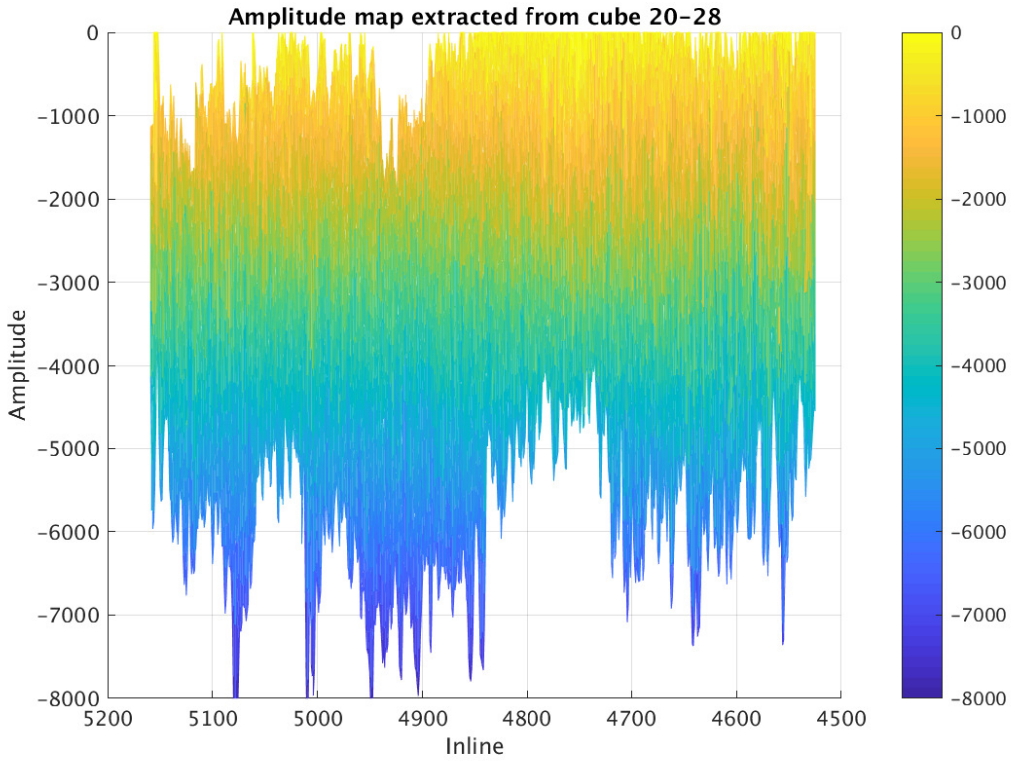

(a) Prior to detuning

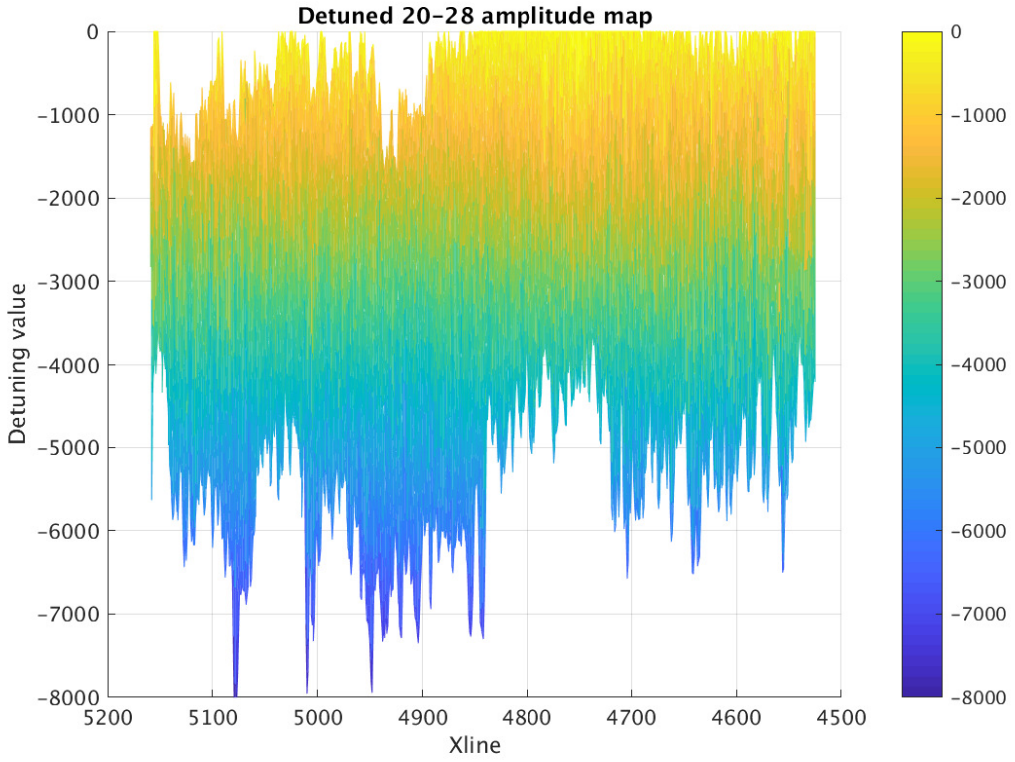

(b) After detuning

Figure 6.13: Detuning results of the top Tofte Formation amplitude map for the angle range of $20 - 28°$ shown for varying amplitude versus crossline.

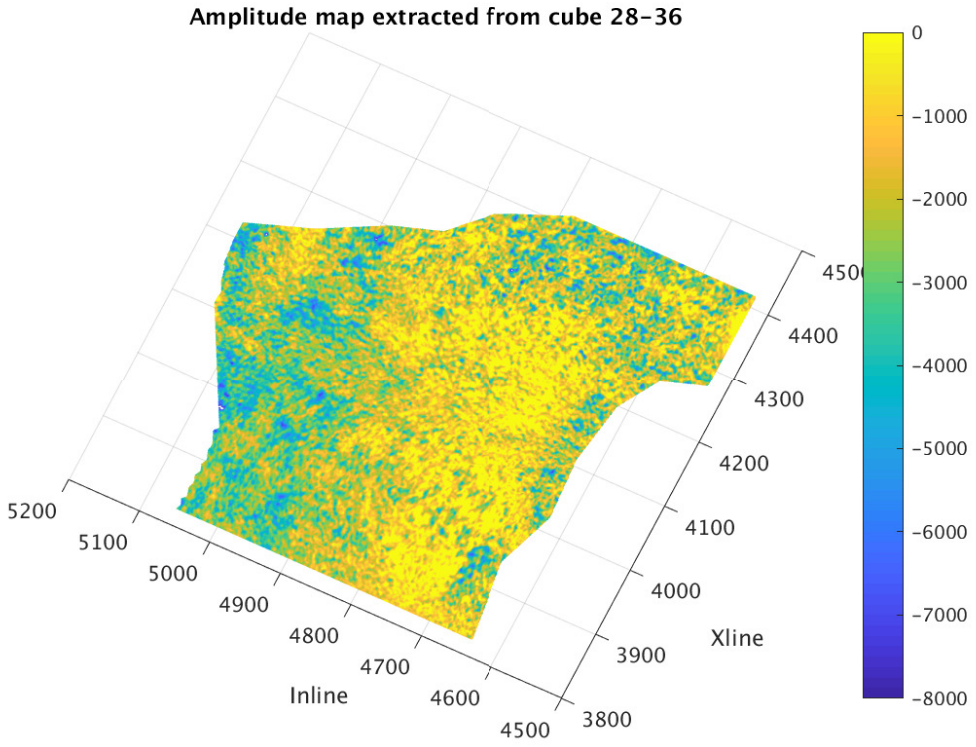

(a) Prior to detunig

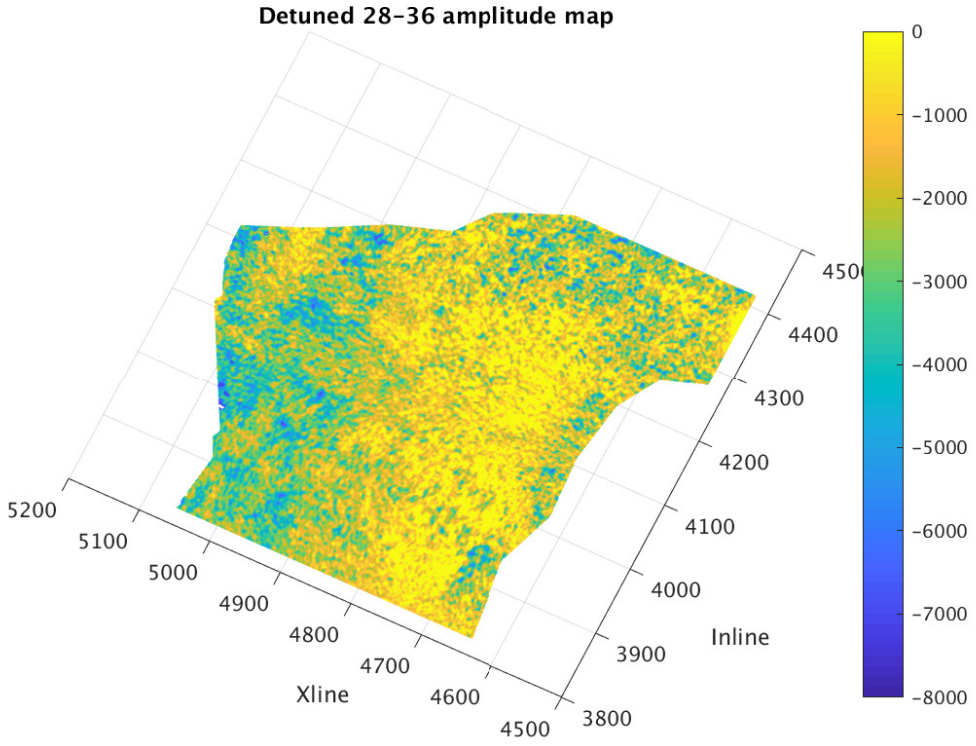

(b) After detuning

Figure 6.14: Detuning results of the top Tofte Formation amplitude map for the angle range of 28 – 36°.

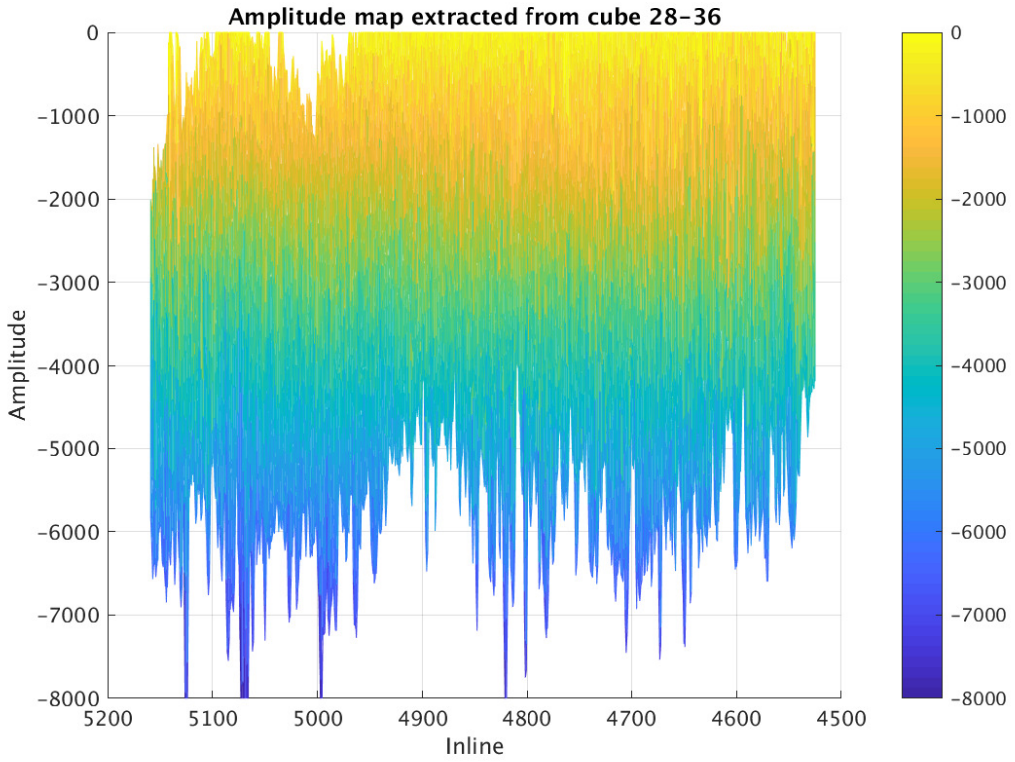

(a) Prior to detuning

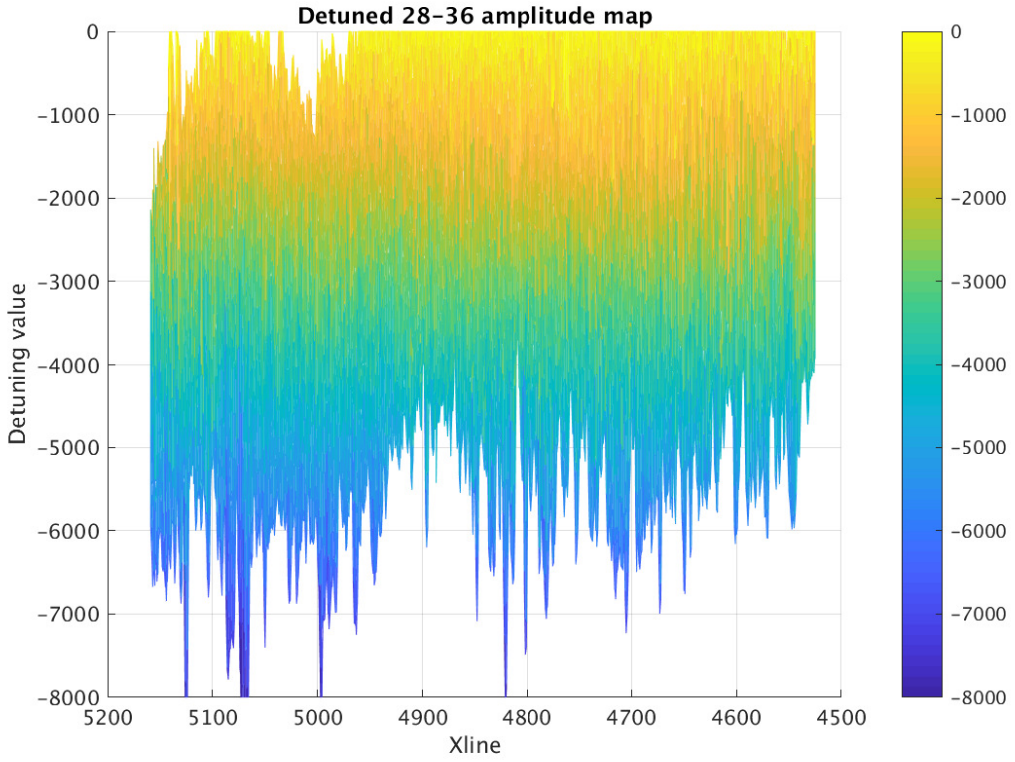

(b) After detuning

Figure 6.15: Detuning results of the top Tofte Formation amplitude map for the angle range of $28 - 36°$ shown for varying amplitude versus crossline.

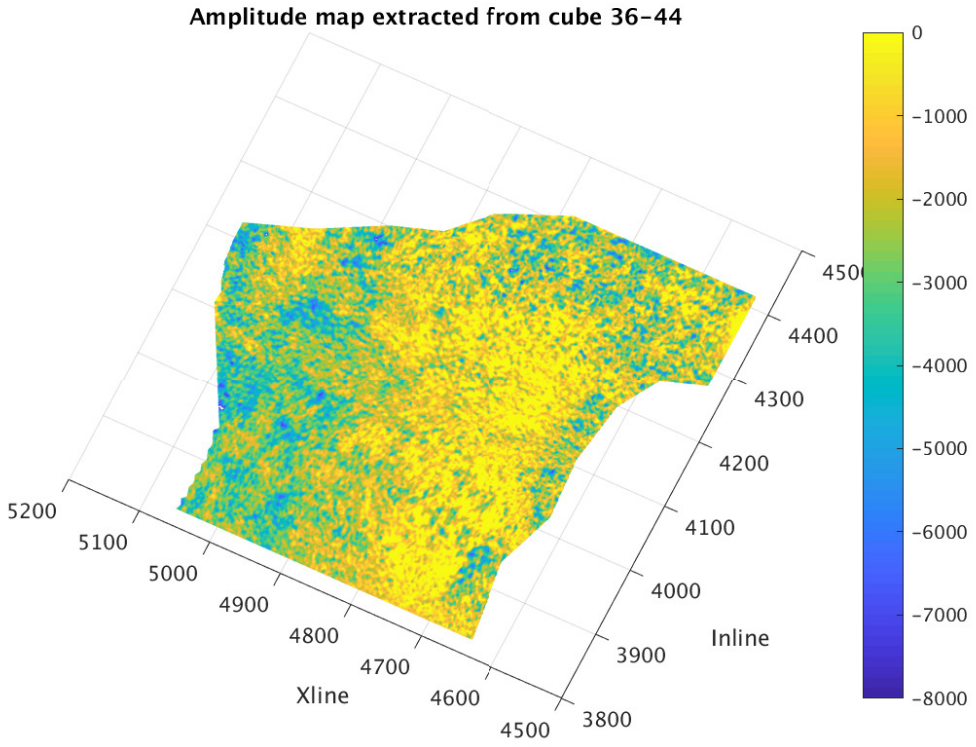

(a) Prior to detuning

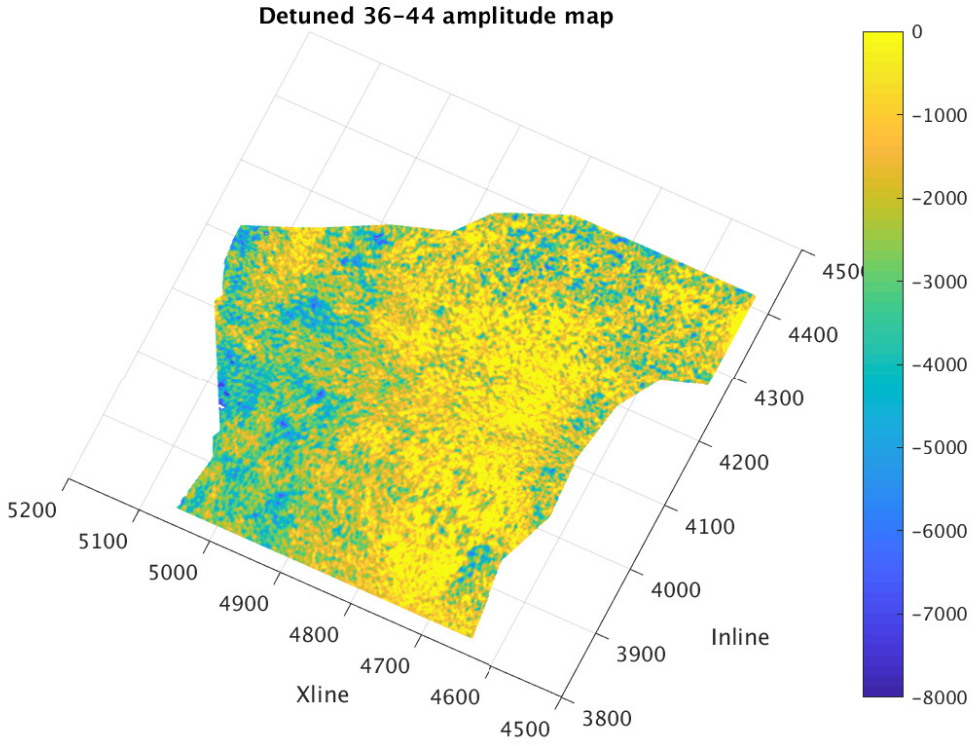

(b) After detuning

Figure 6.16: Detuning results of the top Tofte Formation amplitude map for the angle range of 36 – 44°.

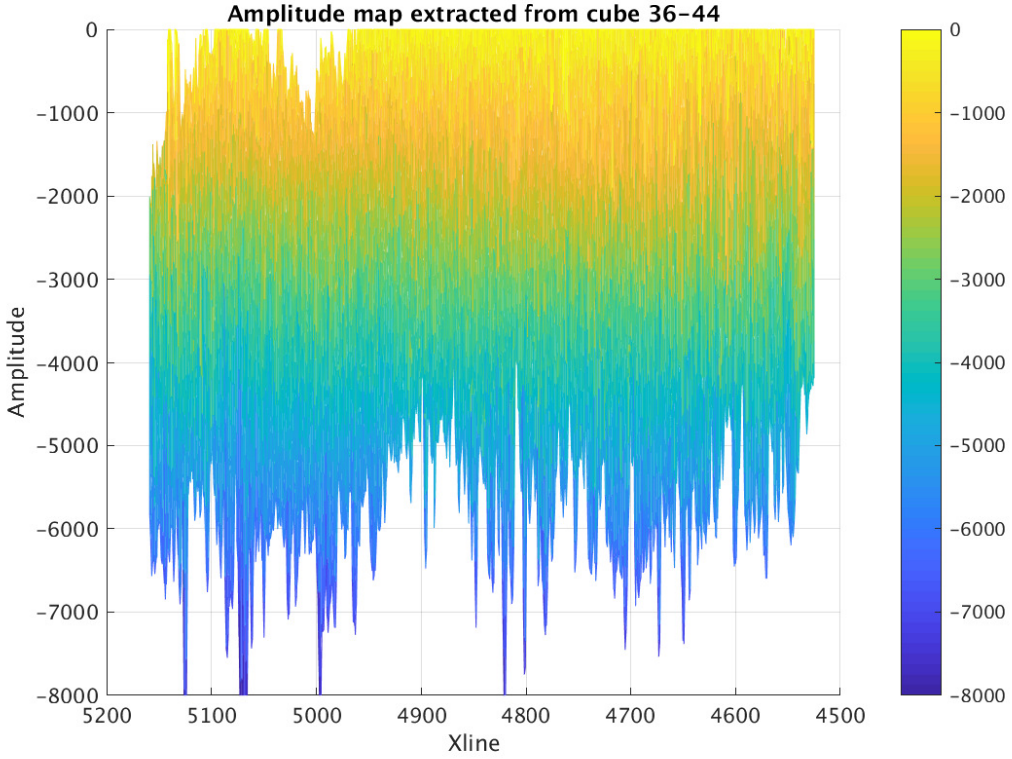

(a) Prior to detuning

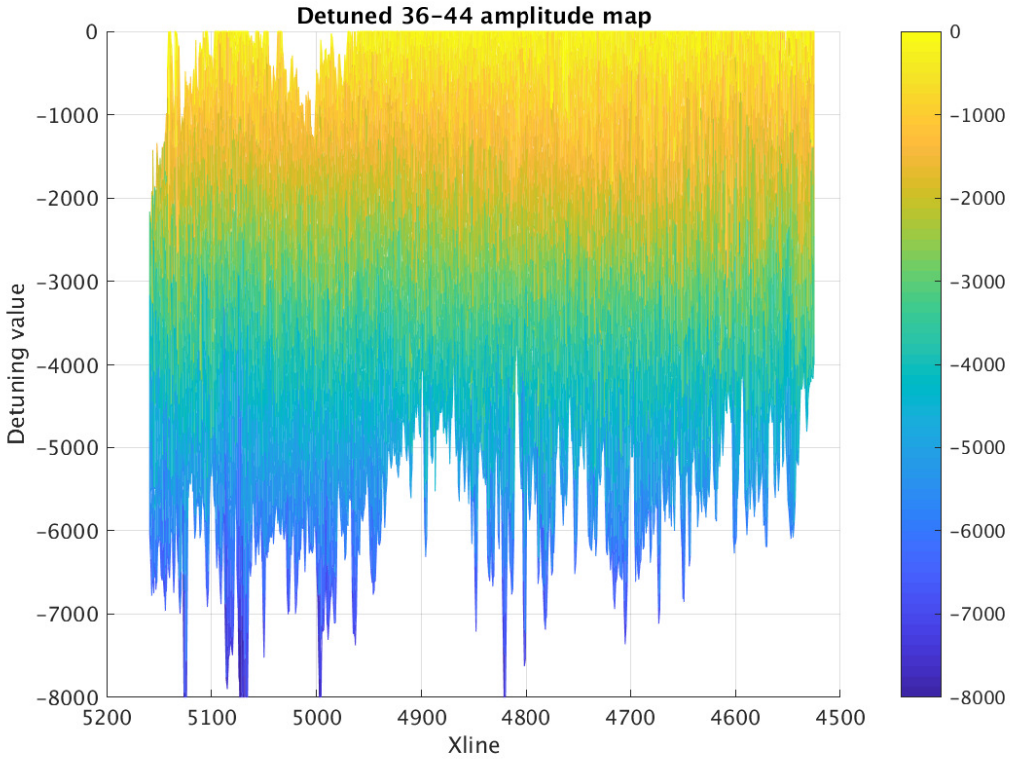

(b) After detuning

Figure 6.17: Detuning results of the top Tofte Formation amplitude map for the angle range of $36 - 44°$, shown for varying amplitude versus crossline.

6.6 Comments on the trends in the detuned amplitude maps

There appears to be some NE-SW amplitude trends in the 12 – 20° and 20 – 28° maps, with at least two NE-SW high negative amplitude "belts". The belt to the left appears to become increasingly negative with angle when comparing the two maps, while the belt to the right become less negative. Moving on to study the trends in the 28 – 36° and 36 – 44° angle cube maps, the NW-SE "belts" are more or less gone.

It appears that there is residual multiple energy affecting the amplitude maps for the near- and mid-angle ranges, and that the preceding multiple removal of the seismic data set has not been completely successful. These NW-SE trends fit well with the multiple polygons shown in Figure 4.3, and it appears that the two data sets suffers from similar residual multiple energy problems.

Thus if the 12 – 20° and 20 – 28° maps are used as input to create the AVO intercept and gradient, the multiple energy will transfer to the net-to-gross estimates and affect the final results.

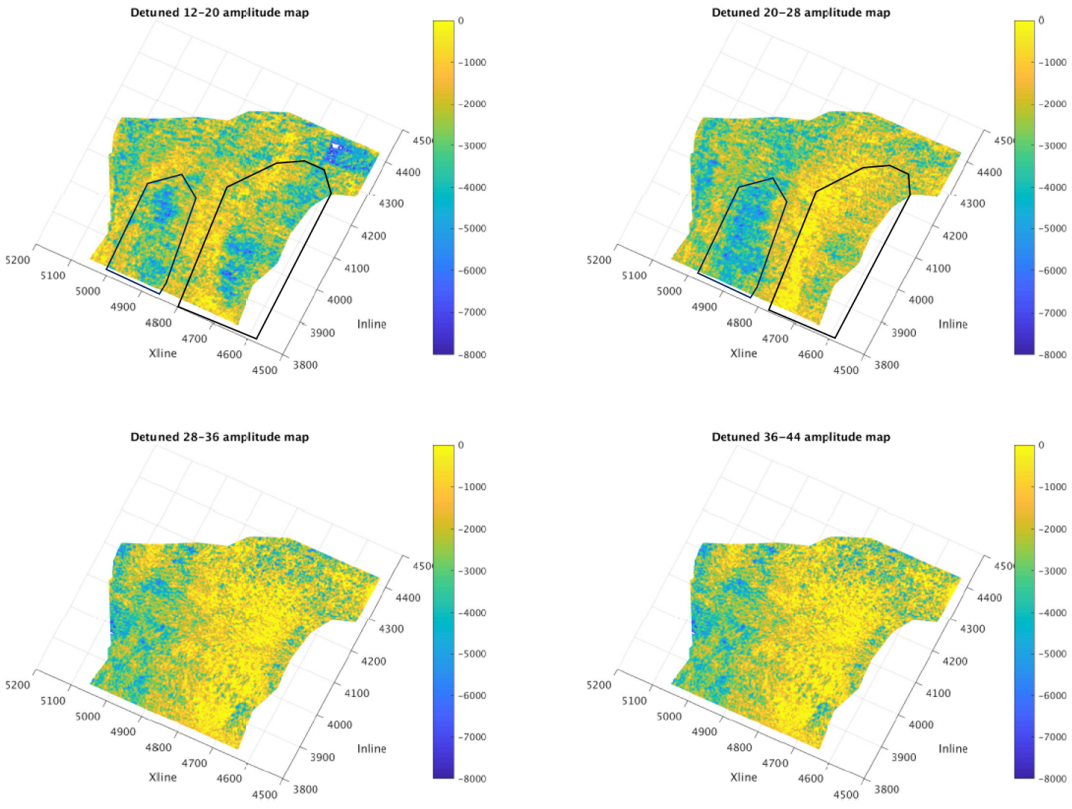

Figure 6.18: A comparison of the detuned amplitude maps of the top Tofte Formation. The multiple polygons are shown in black.

Chapter 7

AVO Attribute Inversion and Net-to-Gross Estimates

7.1 AVO analysis scheme: attribute inversion to net-to-gross

The steps for estimating the AVO attributes and performing the net-to-gross inversion done using MATLAB, and the functions can be found in Appendix B.

7.1.1 Creating the AVO attributes

The AVO attributes where created as intercept and gradient maps from the detuned amplitude maps by fitting a polynomial to the amplitudes in each inline-crossline point, using the Shuey (1985) equation. The maps were calculated using two sets of input, as given in Table 7.1. These two input sets were chosen based on the amplitude trends discovered in the detuned amplitude maps discussed in the previous chapter.

The second input set excludes the near ($12-20°$) amplitude map to investigate if it is possible to reduce the effect of the assumed residual multiple energy when comparing the use of the near, mid and far cube with only using the mid and far cube.

AVO attribute set	Input amplitude maps
1	$12-20°$, $20-28°$, $28-36°$
2	$20-28°$, $28-36°$

Table 7.1: The input to the AVO attribute approximations

Workflow for the AVO attribute estimation in MATLAB

- AVO_attributes.m: Uses amplitude maps of different angle ranges to estimate the intercept and gradient.

The intercept and gradient maps can be exported using the same functions made for exporting the detuned amplitude maps.

Scaling of the intercept and gradient prior to the net-to-gross inversion

To be able to perform the Stovas, Landrø, and Avseth (2006) net-to-gross inversion, the calculated intercept and gradient values have to be scaled down to the reflection coefficient domain. Two different methods of scaling were considered.

Method 1

- Create a Ricker wavelet with a suitable dominant frequency
- Do an AVO forward modelling in a well, or several wells, of choice
- Match the reflection coefficients from the AVO forward modelling with an amplitude value in the amplitude map in the vicinity of the well(s)
- Define factors, F, for scaling down the amplitude maps at different effective angles, as given in Equation 7.1.

If this method is chosen it is necessary to scale down each amplitude map prior to the AVO attribute estimation.

$$A = \text{factor} R_{pp} \tag{7.1}$$

Method 2

- Do an AVO forward modelling in one or several wells using an extracted wavelet from the seismic, and measure the intercept and gradient at the top Tofte Formation reflector
- Use the N/G equations to calculate two coefficients necessary for scaling down the input intercept and gradient, when the net-to-gross of the well is known.

Using this method the intercept and gradient values can be scaled down to reflection coefficient domain using N/G inversion equations directly, as given in Equation 7.4 and 7.5.

$$N/G \approx \frac{2}{\Delta V_P + \Delta\rho}\frac{R}{C_1} \tag{7.2}$$

$$N/G \approx \frac{2}{\Delta V_P - 2\gamma_1^2(\Delta\rho + 2\Delta V_S)}\frac{G}{C_2} \tag{7.3}$$

Which gives the scaling values

$$C_1 \approx \frac{2R}{\Delta V_P + \Delta\rho}\frac{1}{N/G} \tag{7.4}$$

$$C_2 \approx \frac{2G}{\Delta V_P - 2\gamma_1^2(\Delta\rho + 2\Delta V_S)}\frac{1}{N/G} \tag{7.5}$$

The second method was chosen because it is less time consuming, and to avoid the uncertainties in picking correct amplitudes close to the well trajectory in the amplitude maps. The wavelet used for the AVO forward modelling is the wavelet extracted at an effective angle of 24°, which is the mean angle of the angle range used as input.

Calculation of intercept and gradient scaling factors

The three wells 6506/J-1 H, 6506/J-4 H and 6506/12-S were used to calculate the scaling factors for the AVO attributes. The AVO forward modelling can be seen in the well section snapshots in Figure 3.2-3.4, and the calculated intercept and gradient values for the top Tofte Formation interface can be found in Table 7.2.

Table 7.2: Intercept and gradient values from AVO forward modelling

Well	Net-to-gross	Estimated R	Estimated G
6506/J-1 H	≈ 0.95	186	-14 321
6506/J-4 H	≈ 1	-2740	-10 154
(6506/12-1)	(≈ 1)	(-993)	(-6 344)
Average value		-1182*	- 12 238*

Well 6506/12-1 is an exploration well and contains only a synthetic DTS logs, while the other two wells have actual DTS log data. The synthetic DTS log appears to have a noticeable impact on the gradient from the AVO forward modelling, and this well is thus excluded as input for finding scalar values. The estimated gradients in well 6506/J-1 H and 6506/J-4 H are of the same sign and of similar size. The resulting scalars are given in Table 7.3.

Table 7.3: The net-to-gross scaling factors

Well	Net-to-gross	Calculated C_1	Calculated C_2
6506/J-1 H	≈ 0.95	-121150	535420
6506/J-4 H	≈ 1	77670	370630
Average value		-17238	453030

AVO crossplot

The AVO crossplot is created by plotting the scaled intercept map and gradient map against each other.

7.1.2 Net-to-gross inversion

The inversion from AVO attributes to net-to-gross will be performed using the work of Stovas, Landrø, and Avseth (2006), by inverting the intercept and gradient equations for net-to-gross, as given in Equation 2.34 and 2.35. Four different net-to-gross maps are created, one map with each intercept and gradient map as input.

Workflow for inverting AVO attributes to net-to-gross

- Create scaling values for the net-to-gross inversion through AVO forward modelling in a well
- NG_inversion.m: Create four net-to-gross maps from each of the attribute maps
- Create relative net-to-gross maps by normalizing the values in each map. Normalize the assumed multiple areas separately.
- Smooth the final map
- Analyze the net-to-gross distribution

Multiple polygons

Based on the apparent residual multiple energy observed in the detuned amplitude maps in the previous chapter, two multiple polygons, as seen in Figure 6.18, will be implemented in the making and analysis of the net-to-gross maps.

Relative N/G maps: The normalisation of the N/G maps

To make the interpretation of the net-to-gross maps easier, the maps are normalised to fit a range of 0-1. The normalisation of each point is done using Equation 7.6.

$$x_{\text{norm}} = \frac{x - x_{\text{min}}}{x_{\text{max}} - x_{\text{min}}} \tag{7.6}$$

Quality control of the relative N/G maps

A quality control of the match of the relative N/G maps was performed by comparing the net-to-gross values in the LFP wells in the target area to the values in each N/G map. The N/G map with the best match will be used as the final output map.

7.2 Resulting AVO attribute maps

The resulting intercept and gradient maps are shown below in Figure 7.1-7.4. The values in intercept map 1 are are slightly positive and negative, as would be expected of a reflector which shows a class 2 to 3 behaviour. The values in intercept map 2 appear to have too large of a spread, with both very high positive and negative values, which does not fit with the expected behaviour of the top Tofte reflector. The values in intercept map 1 are are slightly positive and negative, as would be expected of a reflector which shows a class 2 and 3 behaviour. The difference between the gradient maps in terms of spread of data is not as large as for the intercept maps.

When comparing the two gradient maps inside the multiple polygons, gradient map 2 appears to contain less traces of the residual multiple energy than gradient map 1. The same conclusion can not be made for the intercept maps.

The AVO crossplot for each intercept and gradient set can be seen in Figure 7.5, and has been included to give further insight into the intercept and gradient maps. The trend in both maps is overall the same, but the spread is larger for the AVO crossplot of set 2. The top Tofte reflector is modelled to have a class 2p/2n or class 3 behaviour. The points around and at zero intercept and gradient will most likely be related to very shaly Tofte Formations, where the amplitude response is weak with a positive gradient (Johannessen, 2018).

The points which plot with high intercept and gradient values in the first quadrant, type 5, can be assumed to be related to residual multiple energy, be caused by noise, or have been picked erroneously and belong to other reflectors than the top Tofte Formation reflector. The points plotting in the fourth quadrant with class 1 behaviour, outside of the 2p zone, can be expected to belong to the formation reflector.

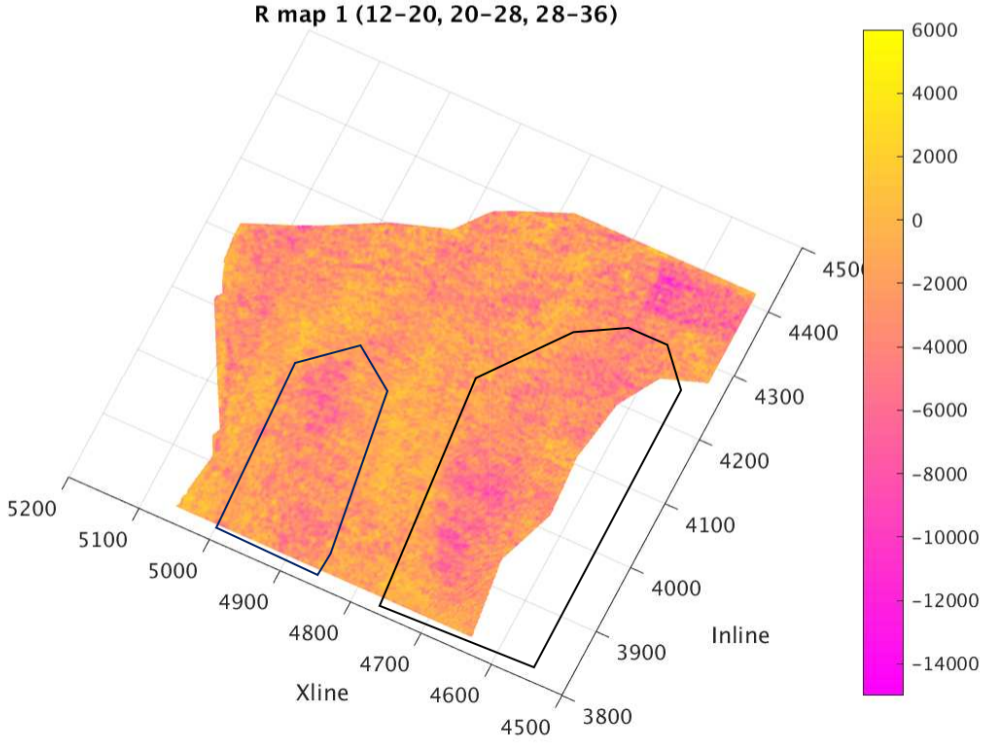

(a)

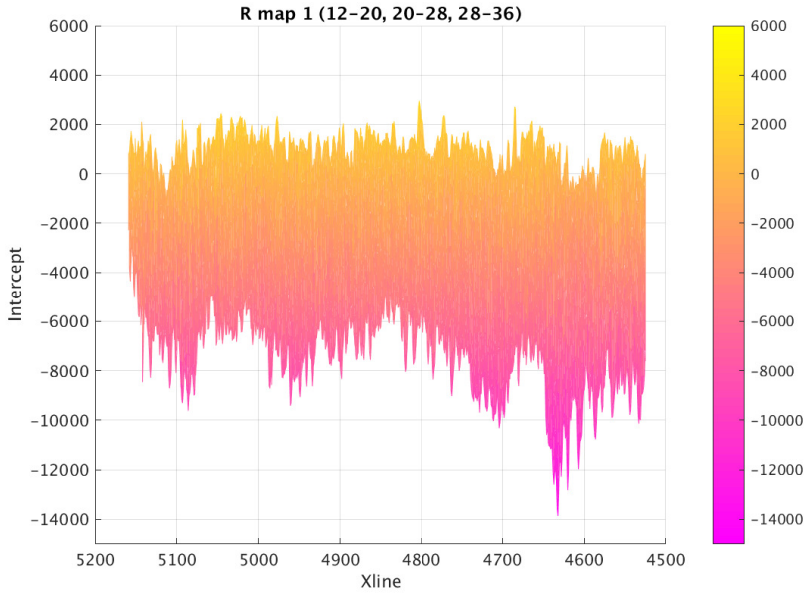

(b) Intercept versus crossline

Figure 7.1: The intercept map 1 which is estimated from the $12-20°$, $20-28°$ and $28-36°$.

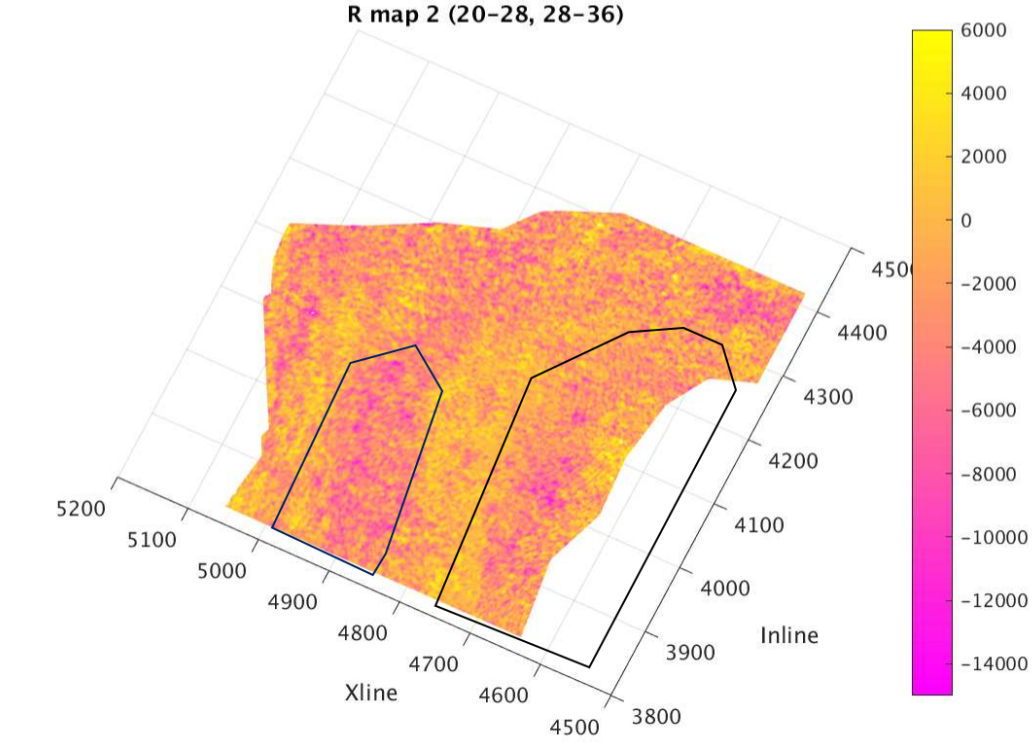

(a)

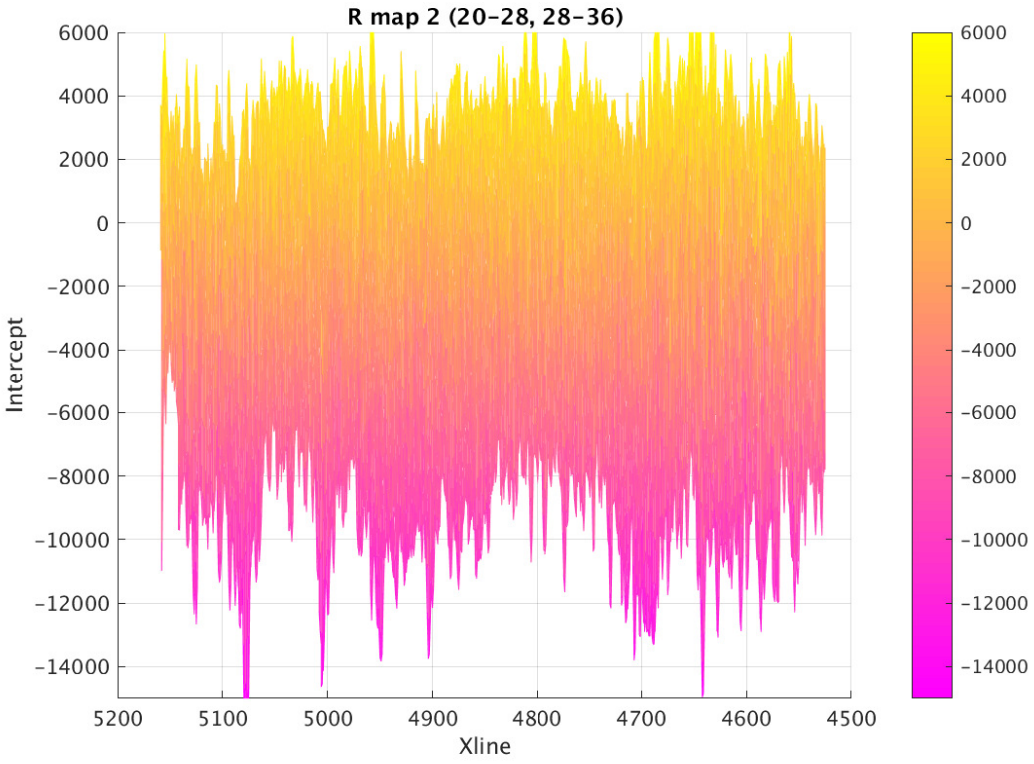

(b) Intercept versus crossline

Figure 7.2: The intercept map 2 which is estimated from the $20-28°$ and $28-36$ maps. The multiple polygons are shown in black.

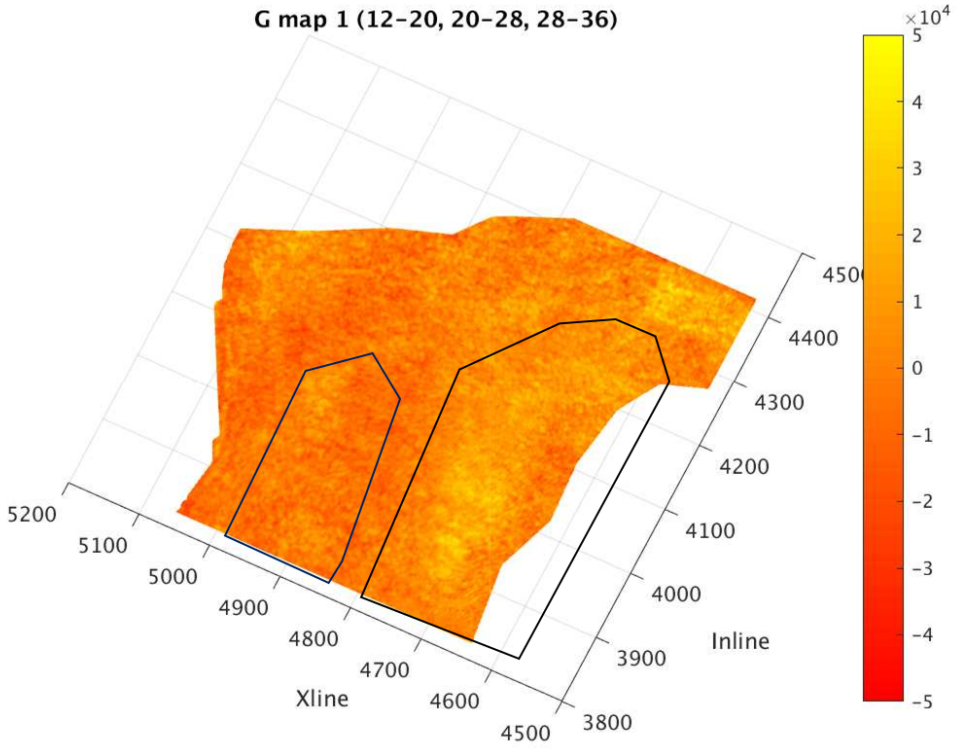

(a)

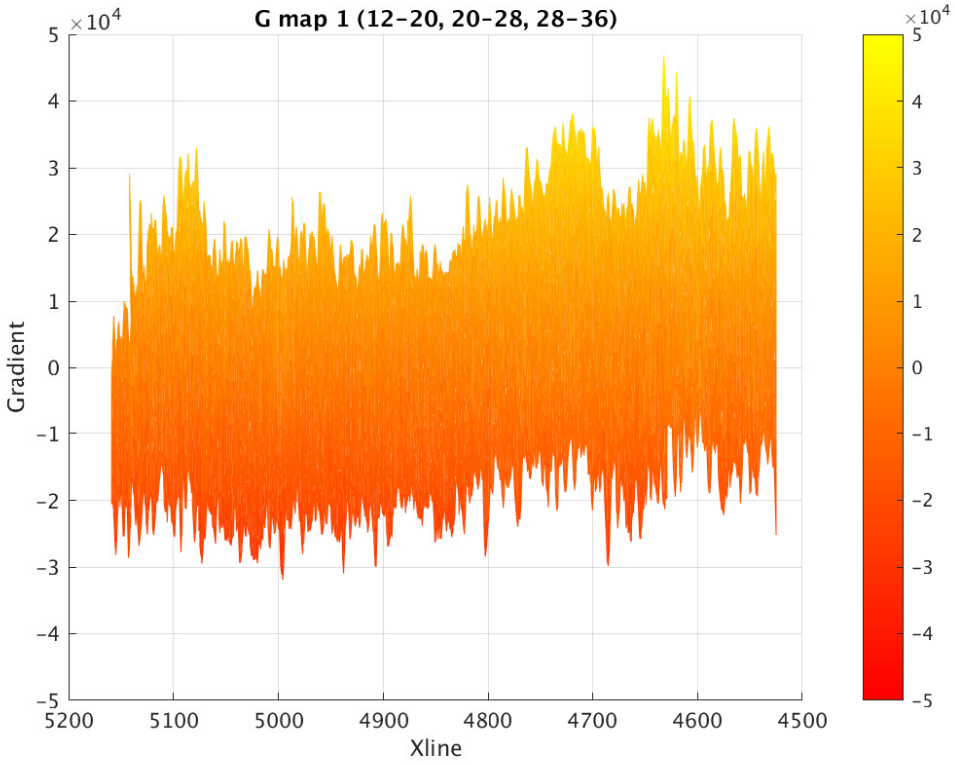

(b) Gradient versus crossine

Figure 7.3: The gradient map 1 which is estimated from the $12-20°$, $20-28°$ and $28-36°$. The multiple polygons are shown in black.

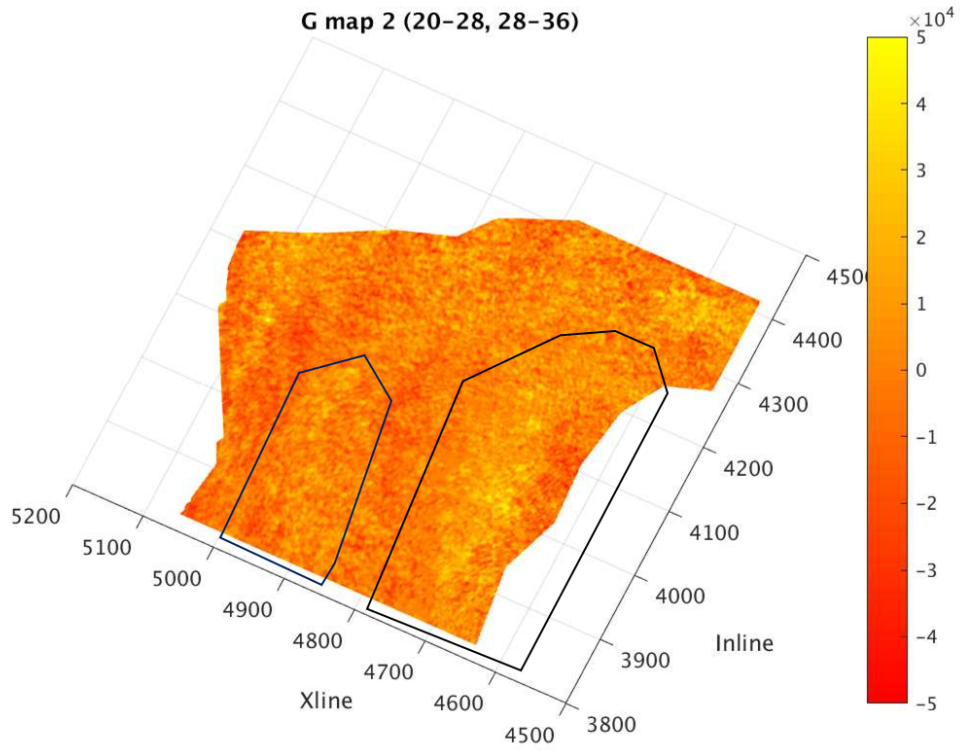

(a)

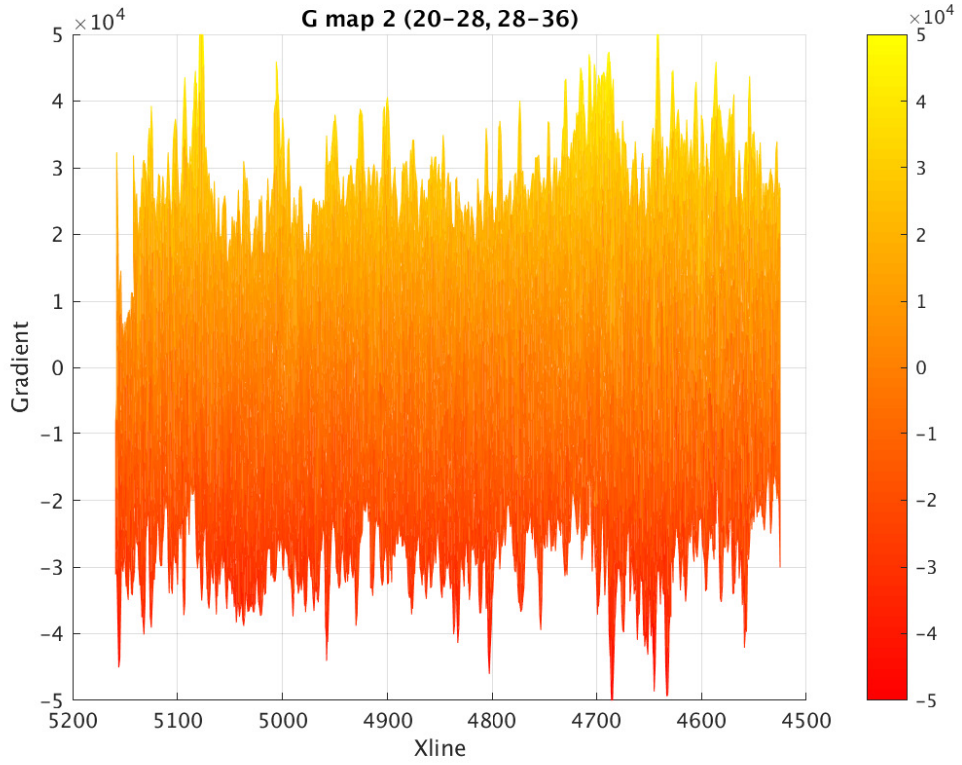

(b) Gradient versus crossline

Figure 7.4: The gradient map 2 which is estimated from the $20-28°$ and $28-36$ maps. The multiple polygons are shown in black.

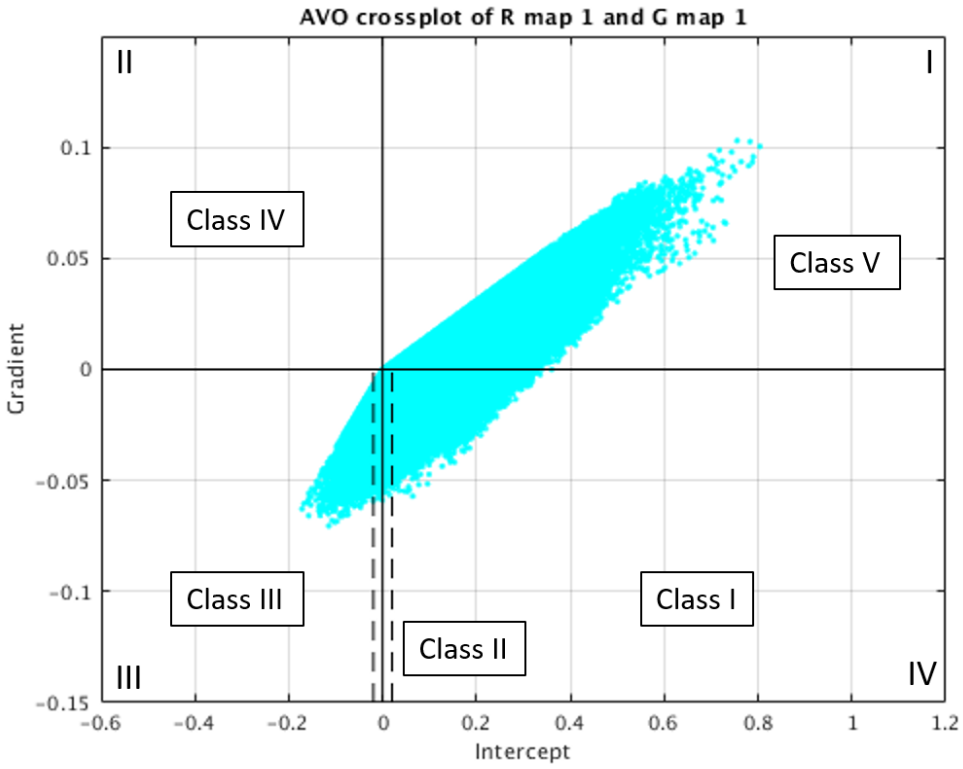

(a) Crossplot 1

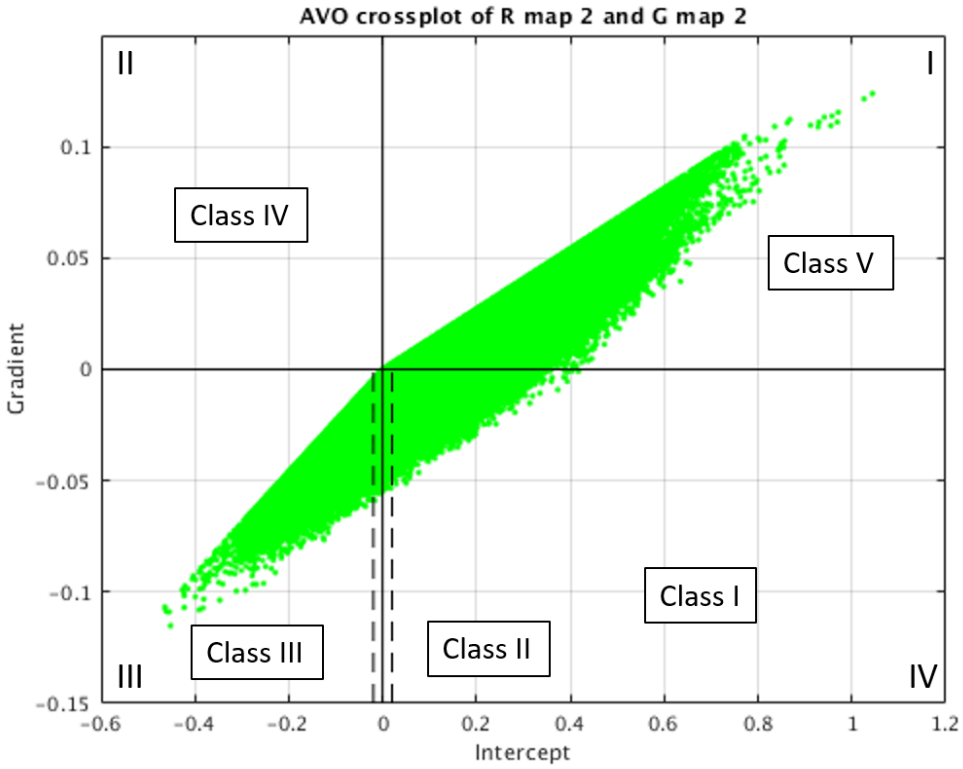

(b) Crossplot 2

Figure 7.5: The two AVO crossplots created for each set of the intercept and gradient maps. The classification scheme of Rutherford and Williams (1989) and Castagna and Swan (1997) has been used.

7.3 Results of the net-to-gross inversion

The net-gross-maps created from each of the intercept and gradient maps can be seen below in Figures 7.6-7.7 7.8-7.13. The first set of figures have not been normalized, and show the spread in the data points. The largest spread is seen in the net-to-gross map from the intercept map created using only the mid and far amplitude maps. The best fit, i.e. the value range closest to 0 and 1, appears to be the net-to-gross maps created using the gradient maps as input, and the difference between the net-to-gross gradient and intercept maps is significant.

Based on these results, three net-to-gross maps created from the gradient maps and the intercept map 1 have been normalised and analysed further. Both of the N/G gradient maps are analysed further to infer if the multiple effect becomes less for the second map where the near angle map has been purposely left out.

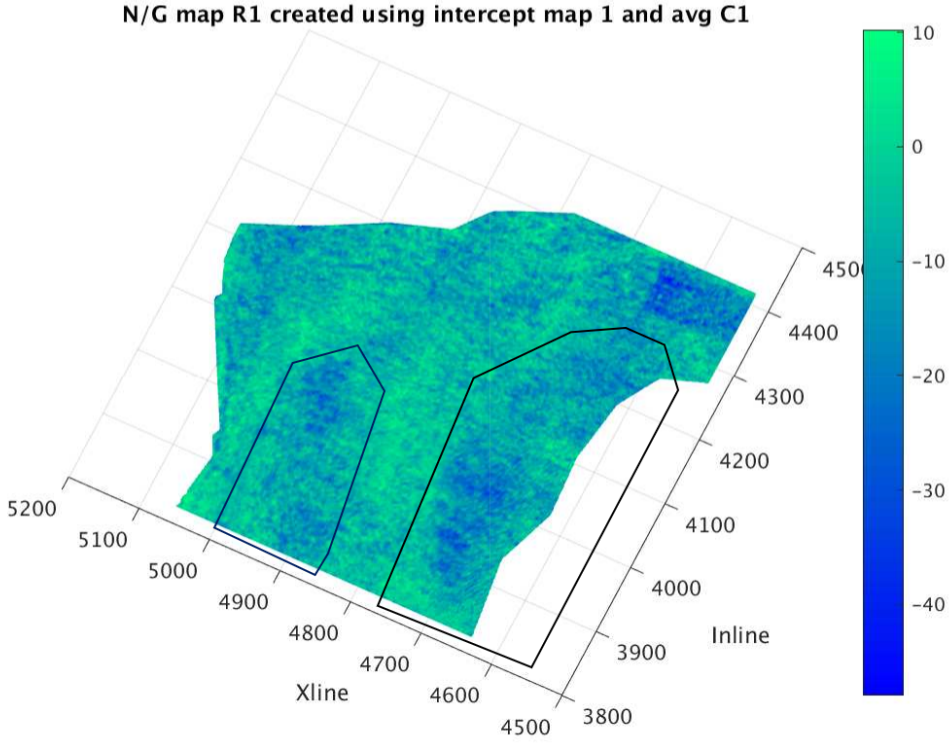

(a) N/G map R1

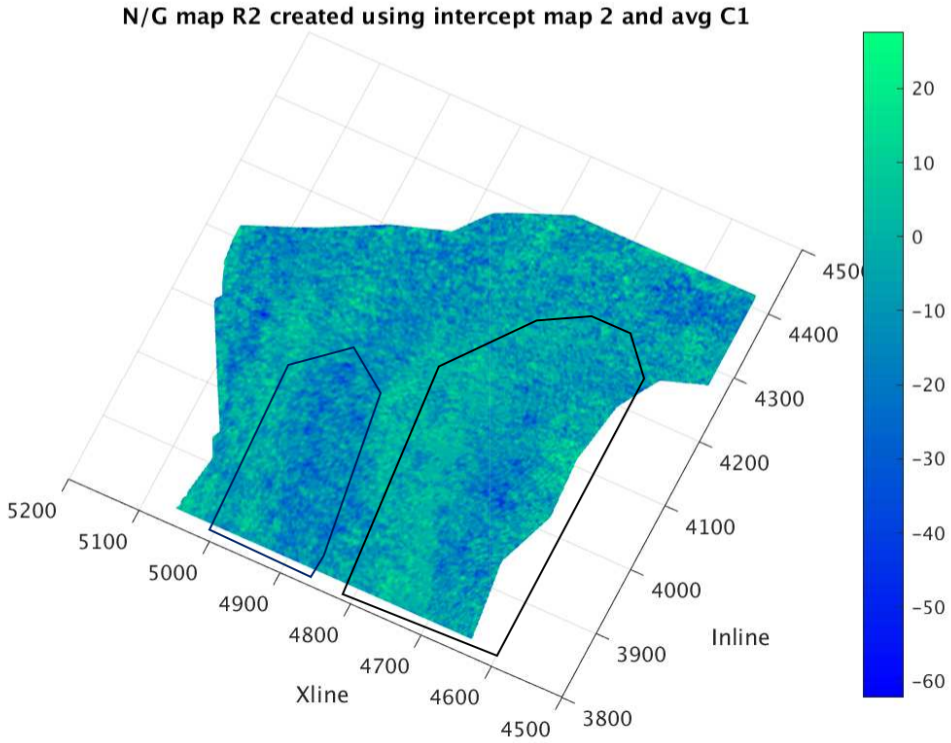

(b) N/G map R2

Figure 7.6: The net-to-gross maps created from the intercept maps.

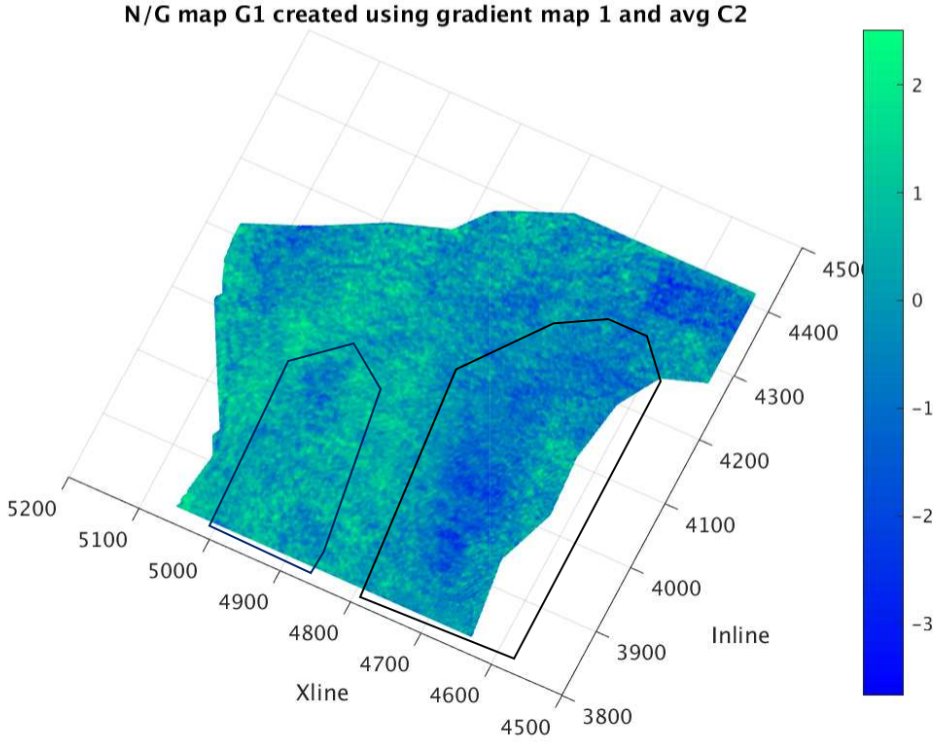

(a) N/G map G1

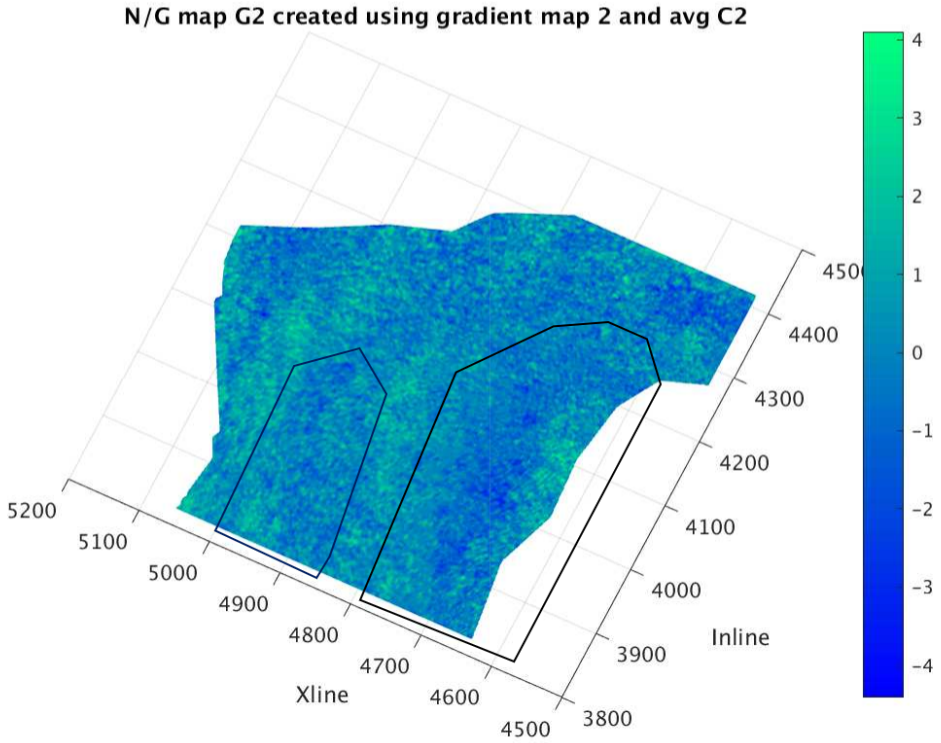

(b) N/G map G2

Figure 7.7: The net-to-gross maps created from the intercept maps.

7.3.1 Relative N/G maps and quality control

Based on the analysis of the multiple cube discussed in Section 4.1 and the preliminary multiple polygons which are shown in Figure 4.3, the analysis of the net-to-gross maps is separated on the basis of the final multiple polygons shown in Figure 6.18. It appears that the quality of the N/G maps in the rig holes is sufficient, but it may have some effect on the residual multiple energy in polygon 1.

The three net-to-gross maps are separated into three maps each, one map for each of the two areas assumed to be contaminated by multiple energy, and one for the area assumed to be free of multiple energy. After the separation, each map is normalised using its respective minimum and maximum value. The normalisation is done to simplify the analysis of the maps, and to allow for a better comparison with the LFP wells in the area.

To evaluate the fit of the relative net-to-gross maps, the net-to-gross ratio in several LFP wells have been compared to the map values near each well, and the result is shown in Table 7.4-7.6.

In the zone assumed to contain no multiple energy the match in the N/G maps is not perfect, but relatively high values in the maps match with high values in the wells. Unfortunately, there is only one LFP well available in each of the multiple polygons. Well 6506/12-K-3 H penetrates the Tofte Formation in the second multiple polygon, and were the well shows a high net-to-gross value, the map indicates low net-to-gross in the area. It could seem like the multiple energy is masking the real net-to-gross response. In the first multiple polygon it is possible to compare well 6506/12-N-2 H with the map in Figure 7.11a. Here the match is better, but it could also be that the well penetrates the formation at the edge of the area affected by multiple energy.

From the quality control it is evident that the R1 and G1 relative N/G maps provide the best net-to-gross prediction. The G2 N/G map, which is created using only two amplitude maps, appear to suffer from the lack of data points compared to the other two maps. The issue of multiples does not appear to be solved by leaving out the near cube, as the two multiple areas look similar, and give the same result in the quality control in all three maps. The multiple energy appears to have more or less the same effect on the intercept and the gradient N/G maps.

From the quality control it appears that the G1 N/G map is slightly better than the R1 N/G map, but they show overall the same trends. The G1 N/G map is used as the resulting map, as it is assumed that the top Tofte reflection response is mostly dependent on the shear velocity contrast (Equinor in house study, Report 1, 2016) indicating that it will be best represented by the gradient.

Net-to-gross map R1

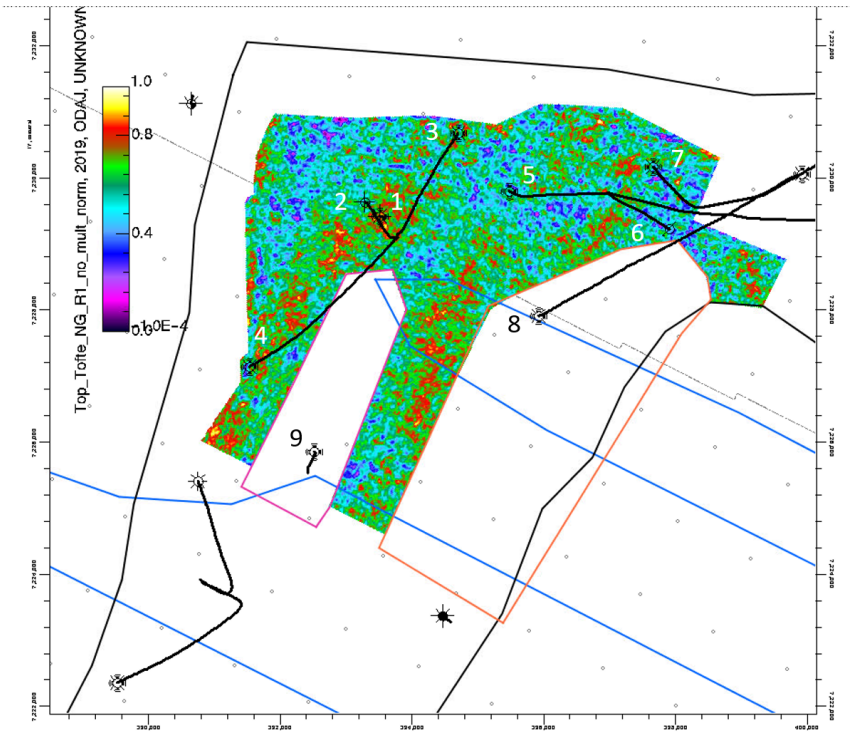

Figure 7.8: The relative (normalised) R1 N/G map for the area assumed not to contain traces of multiple energy. The well paths are shown in black, while the exclusive multiple polygons are shown in pink and orange. The black outline marks the Smørbukk Field, and the blue polygons the righoles. The numbering corresponds to the LFP wells in Table 7.4

.

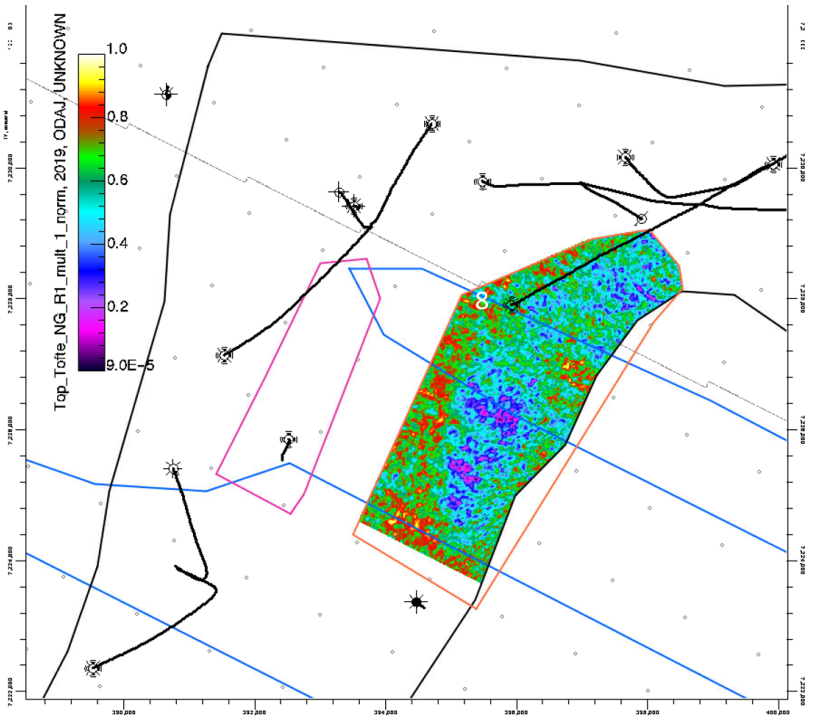

(a) Multiple 1

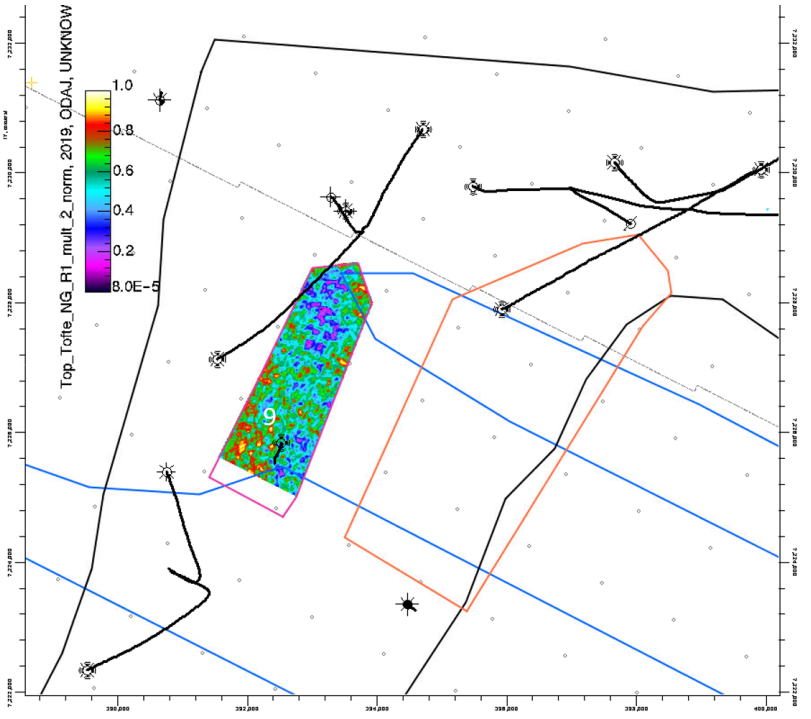

(b) Multiple 2

Figure 7.9: The relative (normalised) G1 N/G maps in the areas assumed to contain multiples. The well paths are shown in black, while the exclusive multiple polygons are shown in pink and orange. The black outline marks the Smørbukk Field, and the blue polygons the righoles. The numbering corresponds to the LFP wells in Table 7.4

Well	Number in figure	N/G in well	Value in N/G map near well		
			No multiples	Multiple 1	Multiple 2
6506/12-1	1	0.95	0.84	-	-
6506/12-J-1 H	2	0.95	0.6	-	-
6506/12-J-3 H	3	0.95	0.73	-	-
6506/12-J-4 H	4	0.95	0.6	-	-
6506/12-M-1 H	5	0.9	0.64	-	-
6506/12-M-2 H	6	0.40	0.40	-	-
6506/12-N-1 H	7	0.4	0.50	-	-
6506/12-N-2 H	8	0.6	-	0.65	-
6506/12-K-3 H	9	0.95	-	-	0.28

Table 7.4: Quality control of the relative R1 N/G maps

Net-to-gross map G1

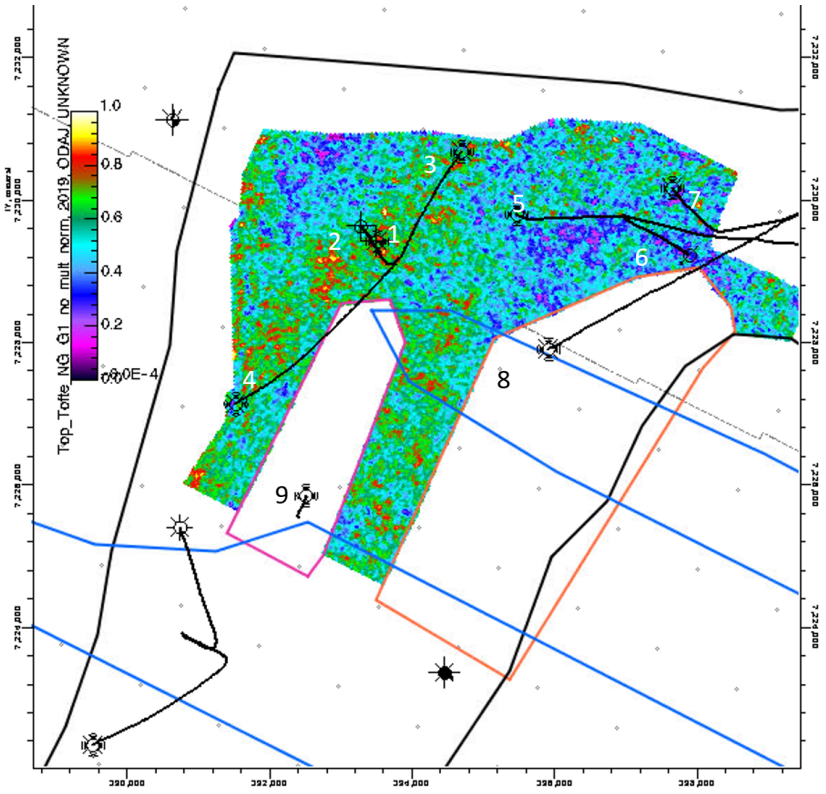

Figure 7.10: The relative (normalised) G1 N/G map for the area assumed not to contain traces of multiple energy. The well paths are shown in black, while the exclusive multiple polygons are shown in pink and orange. The black outline marks the Smørbukk Field, and the blue polygons the righoles. The numbering corresponds to the LFP wells in Table 7.5

.

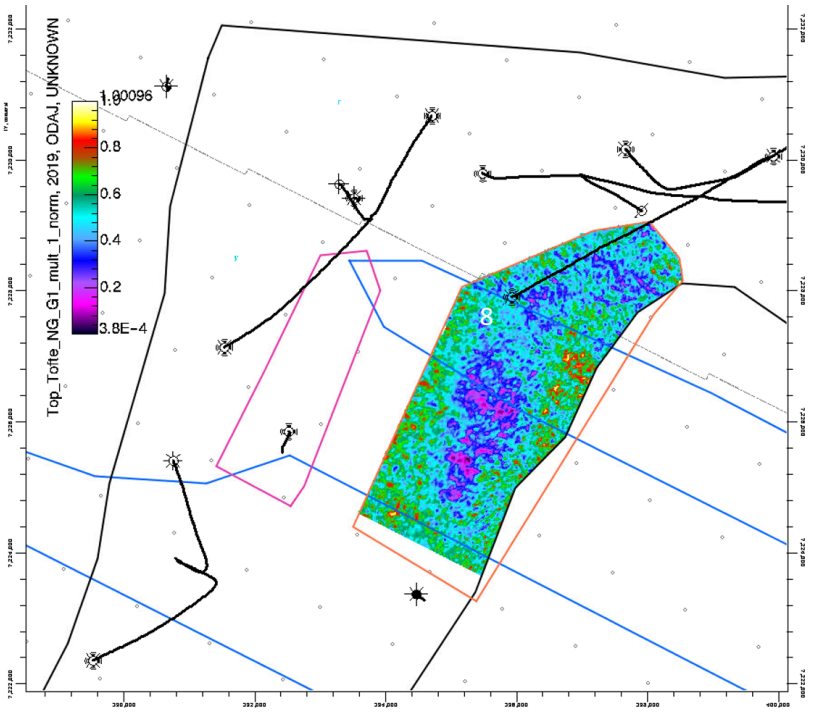

(a) Multiple 1

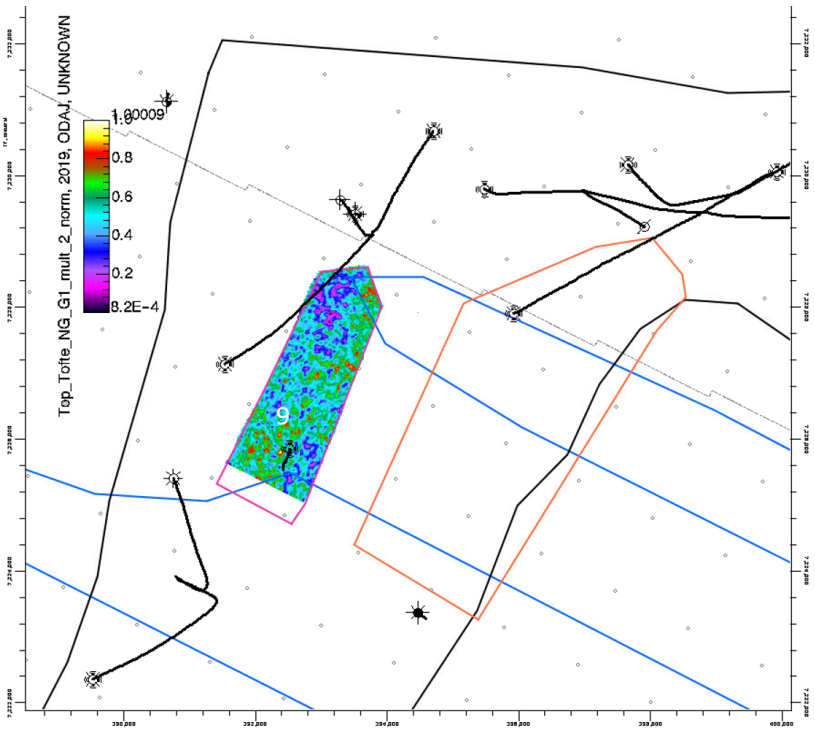

(b) Multiple 2

Figure 7.11: The relative (normalised) G1 N/G maps in the areas assumed to contain multiples. The well paths are shown in black, while the exclusive multiple polygons are shown in pink and orange. The black outline marks the Smørbukk Field, and the blue polygons the righoles. The numbering corresponds to the LFP wells in Table 7.5

.

Well	Number in figure	N/G in well	Value in N/G map near well		
			No multiples	Multiple 1	Multiple 2
6506/12-1	1	0.95	0.8	-	-
6506/12-J-1 H	2	0.95	0.6-0.7	-	-
6506/12-J-3 H	3	0.95	0.75	-	-
6506/12-J-4 H	4	0.95	0.7	-	-
6506/12-M-1 H	5	0.9	0.65	-	-
6506/12-M-2 H	6	0.40	0.45	-	-
6506/12-N-1 H	7	0.4	0.36	-	-
6506/12-N-2 H	8	0.6	-	0.5	-
6506/12-K-3 H	9	0.95	-	-	0.25

Table 7.5: Quality control of the relative G1 N/G maps

Net-to-gross map G2

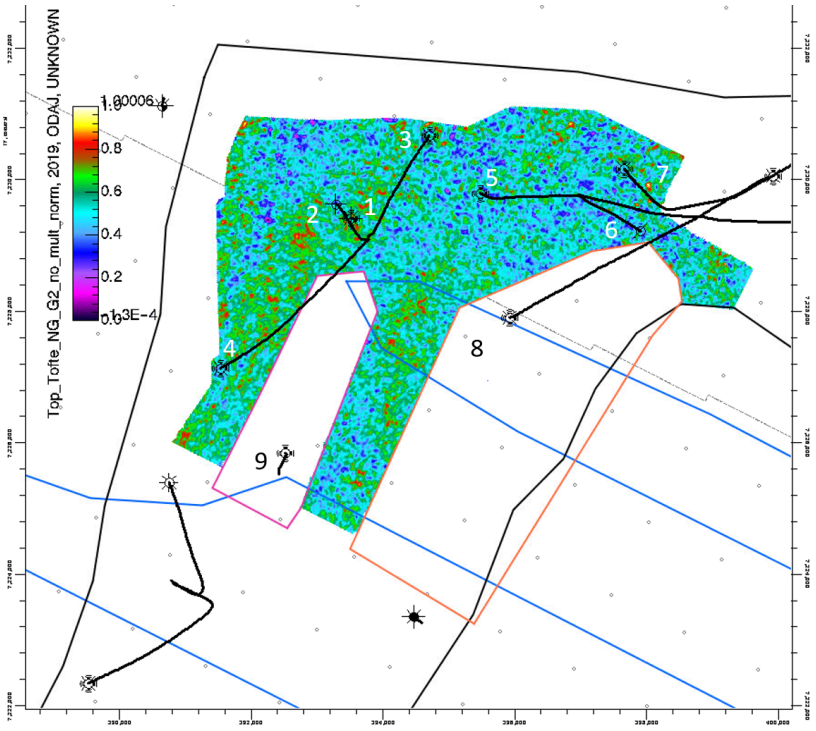

Figure 7.12: The relative (normalised) G1 N/G map for the area assumed not to contain traces of multiple energy. The well paths are shown in black, while the exclusive multiple polygons are shown in pink and orange. The black outline marks the Smørbukk Field, and the blue polygons the righoles. The numbering corresponds to the LFP wells in Table 7.6

.

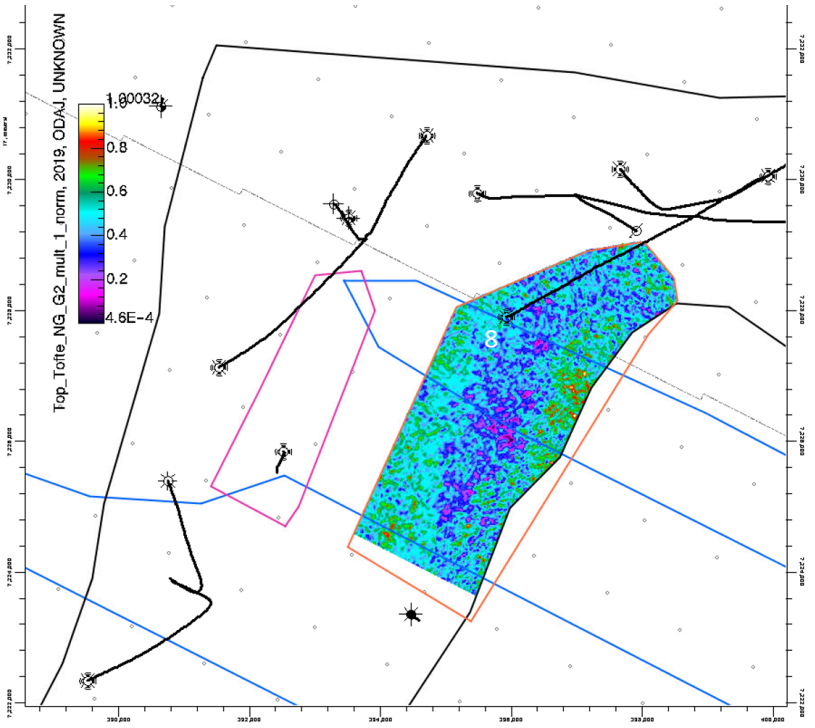

(a) Multiple 1

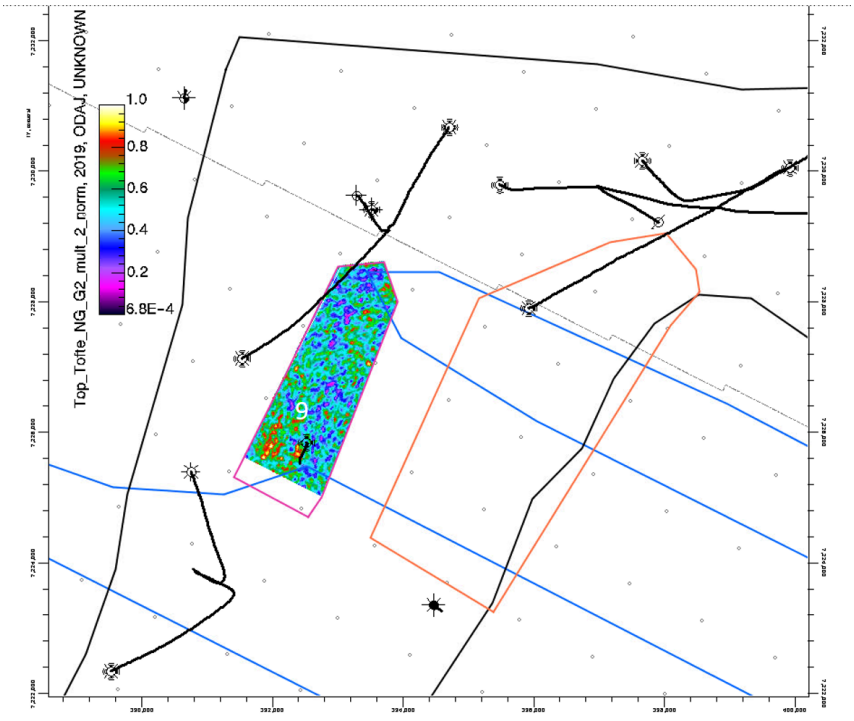

(b) Multiple 2

Figure 7.13: The relative (normalised) G1 N/G maps in the areas assumed to contain multiples. The well paths are shown in black, while the exclusive multiple polygons are shown in pink and orange. The black outline marks the Smørbukk Field, and the blue polygons the righoles. The numbering corresponds to the LFP wells in Table 7.6.

Well	Number in figure	N/G in well	Value in N/G map near well		
			No multiples	Multiple 1	Multiple 2
6506/12-1	1	0.95	0.60	-	-
6506/12-J-1 H	2	0.95	0.41	-	-
6506/12-J-3 H	3	0.95	0.62	-	-
6506/12-J-4 H	4	0.95	0.53	-	-
6506/12-M-1 H	5	0.9	0.60	-	-
6506/12-M-2 H	6	0.40	0.45	-	-
6506/12-N-1 H	7	0.4	0.51	-	-
6506/12-N-2 H	8	0.6	-	0.44	-
6506/12-K-3 H	9	0.95	-	-	0.31

Table 7.6: Quality control of the relative G2 N/G maps

7.3.2 Resulting N/G map of the Tofte Formation

The final net-to-gross map of the Tofte Foramtion is shown in Figure 7.14, with a schematic given in Figure 7.15. It appears that the there is a trend in the N/G map similar to the geological understanding of the deposition given in Figure 1.2. The yellow dotted polygon indicates an apparent N/G trend, which could be one or several sand lobes.

The residual multiple energy complicates the interpretation of the map, and from the quality control it appears that the multiple energy masks the N/G trend in the two multiple polygons which have been investigated. High net-to-gross values are found in the map on either side of the multiple energy polygons in Figure 7.14, and the N/G map gives incorrect, low, N/G values in the second multiple polygon.

There could appear to be more multiple energy present than the two areas already investigated, as indicated by the black dotted polygon in Figure 7.14. However, this is difficult to say with complete certainty, and the area may also be suffering from residual tuning effects, or be related to the geology of the formation.

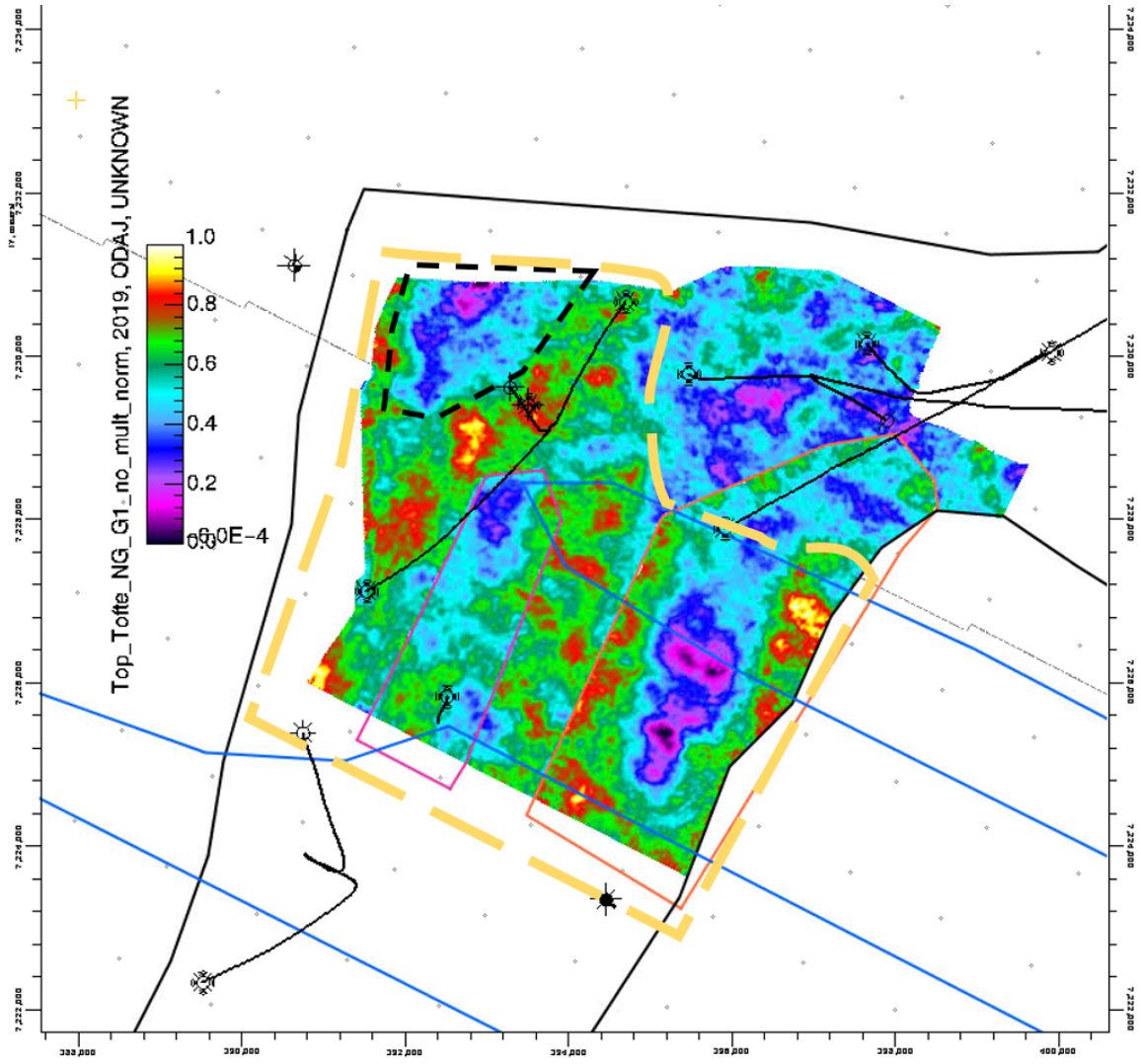

Figure 7.14: The final relative N/G map for the Tofte Formation, the smoothed G1 N/G map. The yellow dotted polygon indicates the apparent N/G trend. The black plotted polygon indicates an area possibly contaminated by multiple energy, residual tuning effects, noise or a trend related to the geology of the formation. The area of low N/G could also be related to a geological trend. The well paths are shown in black, while the exclusive multiple polygons are shown in pink and orange. The black outline marks the Smørbukk Field, and the blue polygons the righoles.

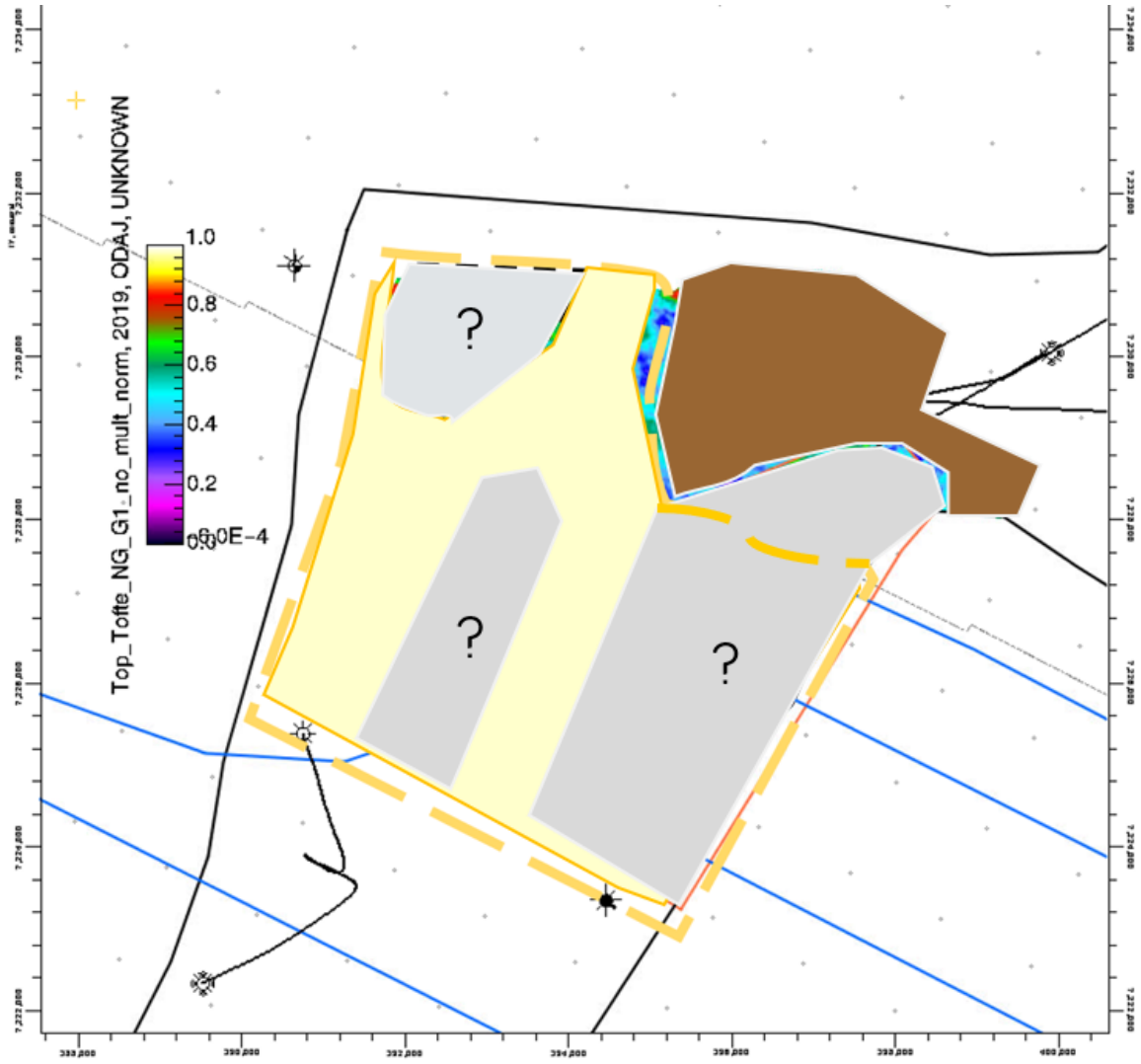

Figure 7.15: The schematic of the final relative N/G map for the Tofte Formation. The yellow dotted polygon indicates the apparent N/G trend. The grey polygons indicates areas of uncertainty in the map. The yellow polygon indicates the high net-gross-area of confidence, and the brown polygon the low net-to-gross area of confidence. The well paths are shown in black. The black outline marks the Smørbukk Field, and the blue polygons the righoles.

Chapter 8

Discussion

The results indicate that the net-to-gross distribution of the Tofte Formation shows an overall high-to-low trend moving from the south-west to the north-east of the area of interest, in concordance with the geological understanding of the depositional history. The tuning effects are constructive and significant, in agreement with earlier research, while the anisotropy effects are found to be insignificant for common acquisition angles. The residual multiple energy appears to still be an issue for the data quality.

Little was known prior to this work about the anisotropy effects, if they were at all significant, and how they would manifest if present. The modelling indicates that the anisotropy effects are constructive, in the same manner as the tuning effects, and that they are not significant but for larger angles of incidence. The modelling is similar to that found by Simm and Bacon (2014) in Figure 2.11.

Given that the effect of anisotropy is negligible, and in any case constructive, the following detuning scheme can be planned only focusing on the tuning effects. The investigation of the tuning effects revealed some interesting facts. The tuning effect appears in this case to be dependent on the AVO behaviour of the top an base reflector of the Tofte Formation, and for the case of a top reflector of type 2 or 3, and a base reflector of type 4, the interference between the side lobes appear to decrease with increasing angle. The decrease in tuning thickness associated with decreasing resolution as the offset becomes larger is hard to see, as the tuning curves are relatively flat.

Even when the tuning effect is relatively small, it is significant because the near angle cubes will be more affected than the far angle cubes, leading to tuning effect having an impact on the AVO attributes. Just like Xie et al. (2017) and many others found, the intercept appears to be increased by at least 25 % near and at tuning thickness, given that the net-to-gross ratio is high. The gradient appears to be masked, or possibly zeroed out, because the near amplitudes appear to grow higher than the far amplitudes near and at tuning thickness.

The findings of the tuning effect on the gradient is not in agreement with the results produced by Lin and Phair (1993), Hamlyn (2014) and Xie et al. (2017), who found that the sign of the intercept and gradient remained unchanged, and that the strength of both was increased by the tuning phenomenon. However, these findings were based on a simple three layer model of a sandstone sandwitched in a shale, and deviations from these results are thus to be expected. If the gradient becomes zero or even positive, and the detuning scheme is not successful, this will give type four or five AVO class behaviour, which could be observed in the second and first quadrant of an AVO crossplot in Figure 7.5, respectively. Thus a detuning scheme was necessary to perform, even though the tuning effects appear not to be very high.

The resulting relative net-to-gross map is assumed not to be affected by anistropy and tuning effects. It became evident in this work that residual multiple energy is still present in the top Tofte Formation reflector, following the demultiple of the data set prior to this work. There appears to be at least two, or possibly three, areas which are affected, and it appears that its presence masks the true net-to-gross trend, as can be seen in Figure 7.14. These areas have to be interpreted separately, and internally, and should not be compared directly with the rest the map.

The N/G map is in concordance with the understanding of the depositional pattern of the Tofte Formation, as described by Dalland, Worsley, and Ofstad (1988) and Figure 1.2 from the Equinor in house study Report 2 (2013). The residual multiple energy complicates the interpretation of the final net-to-gross map in Figure 7.14, but a trend can be seen which can be understood in the context of the formation being deposited by eastwards propagating deltas, where the fans thin out eastwards. Comparing the map in Figure 7.14 with the depositional trend in Figure 1.2, it is evident that the relative N/G map differs slightly from this. The trend in the western part of the area fits with the depositional model, but the trend seen in the eastern part of the N/G map indicates an area of high N/G value where the model predicts that there has been deposited more distal sediments.

From the quality control it appears that the relative N/G map is consistent, and adding this together with the match with the overall geological understanding, it would appear that the map can be trusted and used in further work of the development of the Tofte Formation.

An interesting fact to discuss is the relative match of high net-to-gross ratio in the wells and in the N/G maps. It appears that wells with a net-to-gross value close to one will show corresponding high values, but not higher than approximately 0.8. There are some areas in the relative N/G maps with relative values of one. Unfortunately, there are no wells in these areas to quality check, but the cause of these apparent high N/G values should be discussed. Since lower N/G values match with N/G values equal to one in the wells, these points could simply be the result of the scaling, residual tuning effects, noise, or a combination of all three. It could also be caused by the inversion method provided by Stovas, Landrø, and Avseth (2006). The method is

built for a bimodal effective medium consisting of sand and shale layers, which may not be the perfect match for the heterolithic Tofte Formation.

The black, dotted polygon in Figure 7.14 is also an interesting area to consider. This area could appear to also contain residual multiple energy, or it might simply be an area which has not been detuned properly. The thickness of the Tofte Formation is at its lowest in the west, as seen both in the thickness map in Figure 6.2 and in the seismic section shown in Figure 4.2, and it is possible that the detuning scheme has not been properly executed in this area, leading to anomalies which were not observed directly in the amplitude maps themselves. The area might also be related to the depositional nature of the Tofte Formation. The net-to-gross ratio of the formation can change rapidly, and thus it is not completely unrealistic to find areas like this of lower net-to-gross values in the formation.

In the case of the Tofte Formation in the Smørbukk Field, the AVO analysis as a tool is pushed to its limits. The formation lies at great depth, limiting vertical resolution, and is composed of heterolithics which have a highly variable net-to-gross ratio and marginal porosities. In addition to the amplitude effects and general data quality problems for higher angles, as seen in pre-stack evaluation, possible sources of error and uncertainty are being introduced in each step of the work flow in Figure 1.3.

The first step of the work flow, the investigation of the anisotropy effects, is done using anisotropy parameters derived from an empirical estimation as input. The Li (2006) estimation requires the input of the clay volume and vertical velocities, and these requirements might not be met. The shale volume log is used as a substitute for clay volume, and the well chosen for modelling, 6506/12-J-1 H, is most likely not completely perpendicular to the bedding in the reservoir interval. However, the results of the anistropy parameter estimation from well 6506/12-1, a vertical wildcat, are similar to that of the estimates in 6506/12-J-1 H.

Further more, the modelled anisotropy effect is small for common acquisition angles, which is what would be expected (Thomsen, 1986). Thus the results appear realistic, and the possible sources of error introduced by the Li (2006) estimation seem not to affect the modelling too much. Unfortunately, there is little to compare these results with.

The reliability of detuning scheme is based on the tuning curves and the thickness map used to create the detuning function, in addition to the quality of the input amplitude maps.

Its natural to start the consideration of the limitations of the detuning scheme with the wedge modelling itself. The wedge model has been made using constant layer properties to simplify the resulting tuning curves. This might be thought to be too simplistic, but when comparing the constant input wedge model tuning curves with a wedge model created using the log curves of the same well as input, the estimated tuning effects are very similar. Thus it seems that a simple wedge model is sufficient for this purpose.

The tuning curves were created using the input from one well in an area where the Tofte Formation has a high net-to-gross ratio. A well with a sandy Tofte Formation interval was chosen because the largest tuning effects are believed to be observed were the net-to-gross ratio is highest. This fact introduces several uncertainties. Using these tuning curves to detune areas where the Tofte Formation has a lower net-to-gross ratio will possibly lead to a too harsh detuning process being applied, as the tuning curve are assumed to represent the maximum tuning curve possible in the area of interest. It is also necessary to consider whether the tuning curves are representative or not for the overall tuning effects, and the maximum expected tuning effects for the formation.

Even though only one well is used, it is believed to be representative for the expected tuning effects in the area. A well with a high net-to-gross ratio is also believed correct to use, because as the net-to-gross ratio decreases, the amplitude response of the top Tofte Formation will decrease accordingly, and so will the tuning effects. Using a well of lower sand content would thus underestimate the tuning effects in the areas of high sand content. As the net-to-gross ratio decrease further, there will be no amplitude response, and thus nothing to detune.

The dependence on incidence angle found for the tuning effects will depend on the relative changes in elastic parameters between the Tofte and Lower Ror or Tilje Formations, given a high net-to-gross ratio in the Tofte Formation. The variability in the Tilje Formation is hard to account for in this analysis, and this has not been investigated. However, the Tilje Formation in well 6506/12-J-4 H is characteristic of the formation in the area of interest, with alternating sand and shale laminations. The same can be said for the Lower Ror Formation, which is not more than a thin layer of shale lying on top of the Tilje Formation in the area of interest.

The next important input to the detuning function is the thickness map of the top Tofte Formation. The map is created from five different surfaces in time and depth. Since a base Tofte Formation interpretation is not available, the assumption that the P-wave velocity is approximately constant from the top of the Tofte Formation down to the top of the Tilje 1 Formation is necessary to use. Looking at the well log data it appears that this is an appropriate assumption to make. The Lower Ror Formation is not taken into consideration when creating the thickness map, but given that it is very thin in the area of interest, with thicknesses of approximately one meter, it is not expected to introduce any substantial error to the map.

The thickness map is dependent on the reliability of the interpolated interpretations and the geomodel surfaces used to create it. Given that the internal geometry of the Smørbukk Field is relatively simple, and the interpreted Tofte and Tilje 1 Formation tops are easy to interpret, the input is deemed to be sufficient. Comparing the map with the overall thickness trend in Figure A.1 the map seems to be reliable and fit to use as an estimation of the true thickness of the Tofte Formation in the detuning scheme.

The relatively simple choice of detuning scheme should also be discussed. Given that the estimated tuning effects appear to be small for the angle range used in this work, and that little is

known prior to this thesis regarding the tuning effects in detail, a simple approach is determined to be the best place to start.

Following the discussion of the detuning scheme itself, it is natural to also include a consideration of the input to the detuning scheme, namely the amplitude maps. The extraction of the amplitude map is, much like the thickness map, dependent on the reliability of the interpolated interpretation of the top Tofte Formation.

It has been observed that some areas contain anomalous amplitudes which are suspected not to be related to the formation itself. Some of these areas are removed by the polygons, while others are not. The positive values which have been extracted are set to zero following extraction, as these values are assumed to be related to either wrong picks, wrong or bad interpolation of the top Tofte Formation reflector, related to the reflector being weak or affected by noise, or being caused by residual multiple energy. These uncertainties are something that is necessary to be aware of when analysing the results.

The final step, the AVO attribute inversion to net-to-gross maps, is dependent on the quality of the input data, the validity of the scheme provided by Stovas, Landrø, and Avseth (2006), and the method used for scaling down the intercept and gradient maps. As the resulting N/G maps are not a perfect match to the real N/G of the formation, the first output maps have ranges of positive to negative values, and it appears that the scaling of the intercept map could be more questionable than the scaling of the gradient map due to the difference in range. However, two of the output maps produce promising results for relative N/G estimates, and thus, despite all of these limitations and possible sources of error, it is believed that the AVO inversion has produced maps of the N/G distribution which can be trusted.

Chapter 9

Conclusion

This thesis sought to increase the understanding of the net-to-gross distribution of the Tofte Formation in the northern part of the Smørbukk Field, while also investigating how the formation's amplitude response is affected by tuning and anisotropy. The final relative net-to-gross map shows an overall agreement with the previously described depositional trend of the Tofte Formation, but is more optimistic of the extent of high quality sand bodies in the formation.

The relative net-to-gross map shows a high net-to-gross trend in the south-west, which decreases towards the north-east. Even though the map is relative, it is in good agreement with all wells in the region, with the exception of one the well which penetrates one of the assumed areas affected by residual multiple energy. It appears that the presence of multiple energy masks the net-to-gross trend in the map, and the map should be used with care in these areas. These areas should be interpreted separately from the rest of the map, and N/G values should only be compared internally in each polygon.

The anisotropy effects appear to only be significant at high angles of incidence and not in the angle range used in this work. The modelled anisotropy effect for the P-wave reflection coefficient is constructive, and will strengthen the response of the Tofte Formation at large angles of incidence.

The tuning effects are constructive and significant for the angle range used, and the effect has a decreasing influence with increasing incidence angle caused by the AVO behaviour of the top and base of the Tofte Formation. The shape of the tuning curve and the tuning thickness remains more or less unchanged with varying incidence angle. The Tofte Formation appears to be at and above tuning thickness in the northern part of the Smørbukk Field. Thus, it is not expected to be able to see any destructive effects in the Tofte Formation reflector caused by tuning.

The tuning effects were removed by a detuning scheme, and the resulting detuned amplitude maps were used as input to create the AVO attributes and the inverted relative net-to-gross maps. Although multiple sources of error require a cautious interpretation of the results in certain

regions, the workflow developed in this thesis was able to successfully evaluate the net-to-gross distribution, and produce a final net-to-gross map which can used in further evaluation of the Tofte Formation.

Chapter 10

Further work

- Further research is required regarding the areas suspected of containing residual multiple energy, and the effect it has on the net-to-gross trend of the Tofte Formation. The understanding of the geology of the formation needs to be combined in this investigation to get a better understanding of which trends can be attributed to the geology of the formation, and which trends that could be caused by other effects.
- Based on the results of the investigation of the tuning effects, the dependence of the tuning effects of the Tofte Formation on the underlying Lower Ror and Tilje Formations should be considered further, to see if different tuning curves should be used in different parts of the area of interest.
- The method of scaling the input amplitude maps prior to the net-to-gross inversion shows room for improvement, and it should be made to be more robust.
- The detuning and net-to-gross inversion scheme can also be expanded to include the whole of the Tofte Formation in the Smørbukk Field.

Bibliography

Aki, K. and Richards, P. G. (1980). *Quantitative Seismology: Theory and Methods*. San Fransisco: Freeman.

Avseth, P., Mukerji, T., and Mavko, G. (2008). *Quantitative Seismic Interpretation*. First edition. New York: Cambridge University Press.

Bakke, N. E. and Ursin, B. (1998). "Thin-bed AVO effects". In: *Geophysical Prospecting* 46.6, pp. 571–587.

Banik, N. C. (1987). "An effective anisotropy parameter in transversely isotropic media". In: *Geophysics* 52.12, pp. 1654–1664.

Blangy, J. P. (1994). "AVO in transversely isotropic media - An overview". In: *Geophysics* 59.5, pp. 775–781.

Bortfeld, R. (1961). "Approximations to the reflection and transmission coefficients of plane longitudinal and transverse waves". In: *Geophysical Prospecting* 9.4, pp. 485–502.

Brown, A. R., Wright, R. M., Burkart, K. D., and Abriel, W. L. (1984). "Interactive seismic mapping of net producible gas sand in the Gulf of Mexico". In: *Geophysics* 49.6, pp. 686–714.

Brown, A. R., Wright, R. M., Burkart, K. D., Abriel, W. L., and McBeath, R. G. (1986). "Tuning effects, lithological effects and depositional effects in the seismic response of gas reservoirs". In: *Geophysical Prospecting* 34.5, pp. 623–647.

Castagna, J. P. (1993). "AVO Analysis - Tutorial and review". In: *Offset-Dependent Reflectivity - Theory and Practice of AVO Analysis*. Ed. by J. P. Castagna and M. M. Backus. First edition. SEG.

Castagna, J. P. and Swan, H. W. (1997). "Principles of AVO crossplotting". In: *The Leading Edge* 16.4.

Connolly, P. (2005). "Net Pay Estimation from Seismic Attributes". In: *EAGE 67th Conference and Exhibition*.

– (2007). "A simple, robust algorithm for seismic net pay estimation". In: *The Leading Edge* 26.10, pp. 1278–1282.

Daley, P. F. and Hron, F. (1977). "Reflection and transmission coefficients for transversely isotropic media". In: *Bulletin of the Seismological Society of America* 67.3, pp. 661–675.

Dalland, A., Worsley, D., and Ofstad, K. (1988). *NPD-BULLETIN NO 4: A lithostratigraphic scheme for the Mesozoic and Cenozoic succession offshore mid- and northern Norway*. Stavanger: Norwegian Petroleum Directorate.

Francis, A. (2015). "A Simple Guide to Seismic Amplitudes and Detuning". In: *GEO ExPro Magazine* 12.5, pp. 68–72.

Hamlyn, W. (2014). "Thin beds, tuning, and AVO". In: *The Leading Edge* 33.12, pp. 1394–1396.

Johannessen, O. M. (2018). "AVO Feasibility Study of the Ror Formation and the Heterogeneous Tofte and Tilje Formations in the Smørbukk Field (unpublished)".

Keith, C. M. and Crampin, S. (1977). "Seismic body waves in anisotropic media: reflection and refraction at a plane interface". In: *Geophysical Journal International* 49.1, pp. 181–208.

Knott, C. G. (1899). "III. Reflexion and refraction of elastic waves, with seismological applications". In: *The London, Edinburgh, and Dublin Philosophical Magazine and Journal of Science* 48.290, pp. 64–97.

Li, F., Cao, S., Han, D., and Yao, J. (2009). "Phase scanning method for detuning in thin bed". In: *SEG Technical Program Expanded Abstracts*, pp. 346–350.

Li, Y. (2006). "An empirical method for estimation of anisotropic parameters in clastic rocks". In: *The Leading Edge* 25.6, pp. 706–711.

Lin, T. L. and Phair, R. (1993). "AVO Tuning". In: *SEG Technical Program Expanded Abstracts*, pp. 727–730.

Marion, D., Nur, A., Yin, H., and Han, D. H. (1992). "Compressional velocity and porosity in sand-clay mixtures". In: *Geophysics* 57.4, pp. 554–563.

Martinius, A. W., Ringrose, P. S., Brostrøm C. Elfenbein, C., Næss, A., and Ringås, J. E. (2005). "Reservoir challenges of heterolithic tidal sandstone reservoirs in the Halten Terrace, mid-Norway". In: *Petroleum Geoscience* 11.1, pp. 3–16.

Mavko, G., Mukerji, T., and Dvorkin, J. (2012). *The Rock Physics Handbook: Tools For Seismic Analysis of Porous Media*. Second edition. New York: Cambridge University Press.

Meckel, L. D. Jr. and Nath, A. K (1977). "Geologic Considerations for Stratigraphic Modeling and Interpretation: Section 3. Stratigraphic Models from Seismic Data". In: AAPG, pp. 417–438.

Norwegian Petroleum (2019). *Åsgard*. URL: http://www.norskpetroleum.no/en/facts/field/asgard (visited on 02/05/2019).

Norwegian Petroleum Directorate (2019). *FactPages*. URL: http://www.factpages.npd.no/factpages/ (visited on 11/03/2019).

Ostrander, W. J. (1984). "Plane-wave reflection coefficients for gas sands at nonnormal angles of incidence". In: *Geophysics* 49.10, pp. 1637–1648.

Rüger, A. (1997). "P-wave reflection coefficients for transversely isotropic models with vertical and horizontal axis of symmetry". In: *Geophysics* 62.3, pp. 713–722.

Rutherford, S. R. and Williams, R. H. (1989). "Amplitude-versus-offset variations in gas sands". In: *Geophysics* 54.6, pp. 680–688.

Shuey, R. T. (1985). “A simplification of the Zoeppritz equations”. In: *Geophysics* 50.4, pp. 609–614.

Simm, R. and Bacon, M. (2014). *Seismic amplitude*. First edition. New York: Cambridge University Press.

Stovas, A., Landrø, M., and Avseth, P. (2006). “AVO attribute inversion for finely layered reservoirs”. In: *Geophysics* 71.3, pp. C25–C36.

Thomsen, L. (1986). “Weak elastic anisotropy”. In: *Geophysics* 51.10, pp. 1954–1966.

– (1993). “Weak anisotropic reflections”. In: *Offset-Dependent Reflectivity - Theory and Practice of AVO Analysis*. Ed. by J. P. Castagna and M. M. Backus. First edition. SEG.

– (2002). *Understanding Seismic Anisotropy in Exploration and Exploitation*. Second edition. New York: SEG.

Widess, M. B. (1973). “HOW THIN IS A THIN BED?” In: *Geophysics* 38.6, pp. 1176–1180.

Wiggins, R., Kenny, G. S., and McClure, C. D. (1983). “A method for determining and displaying the shear velocity reflectivities of a geologic formation. European Patent Application 0113944.” In:

Wright, J. (1987). “The effects of transverse isotropy on reflection amplitude versus offset”. In: *Geophysics* 52.4, pp. 564–567.

Xie, X., Fan, J., Zhang, Z., Shen, H., and Guo, N. (2017). “Quantitative analysis of AVO tuning effect for a single thin bed”. In: *SEG Technical Program Expanded Abstracts*, pp. 733–737.

Zhang, H. and Brown, R. J. (2001). “A review of AVO analysis”. In: *CREWES Research Report* 13, pp. 357–380.

Zoeppritz, K. (1919). “On the reflection and propagation of seismic waves”. In: *Gottinger Nachr* 1, pp. 66–84.

Appendices

Appendix A

Thickness map of the Tofte Formation from well log data

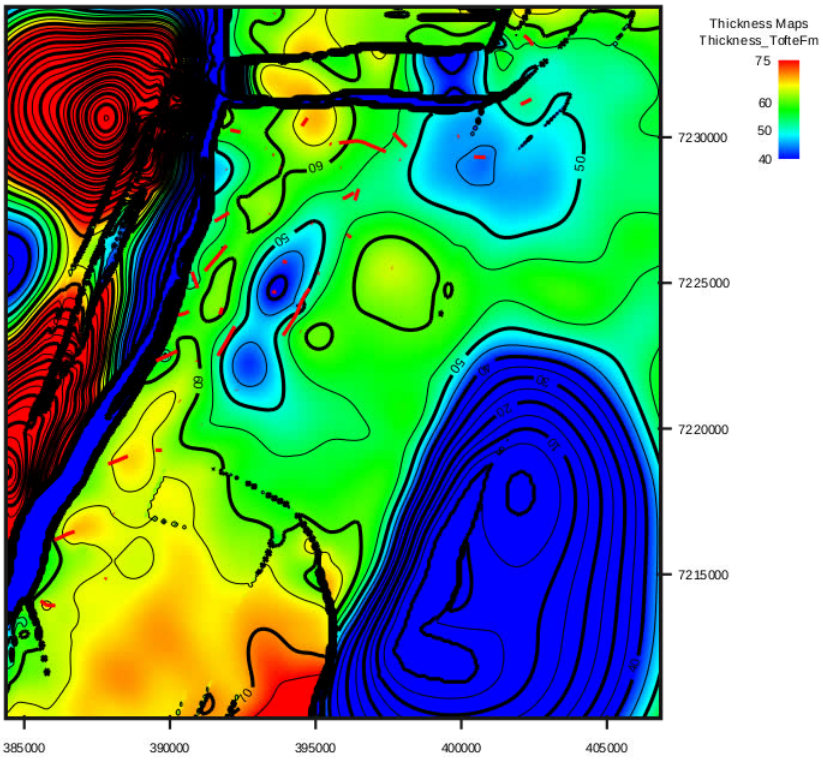

Figure A.1: Thickness map of the Tofte Formation from well log data in the Smørbukk Field. The unit is meters.

Appendix B

MATLAB Functions

B.1 Anisotropy effect investigation and removal

```
%% Modelling of the anisotropy effect on the P-wave reflection
   coefficient for the Ror-Tofte Fm interface.

%% Input
% Incident angle range
theta = 0:0.1:60;

% Velocity and density input for Ror (layer 1) and Tofte (layer
    2) (average values 40 above and below interface)
Vp1 = 4117;
Vp2 = 4324;

Vs1 = 2444;
Vs2 = 2704;

rho1 = 2598;
rho2 = 2465;

Z1 = rho1 * Vp1;
Z2 = rho2 * Vp2;
Z = (Z1 + Z2)/2;
dZ = Z2 - Z1;

G1 = rho1 * Vs1^(2);
```

```
23 G2 = rho2* Vs2^(2);
24 G = (G1 + G2)/2;
25 dG = G2 - G1;
26
27 % Thomsen (1986) parameters epsilon and delta (average values
       40 m above and below interface)
28 epsilon1 = 0.263;
29 epsilon2 = 0.073;
30
31 delta1 = 0.084;
32 delta2 = 0.023;
33
34 depsilon = epsilon2 - epsilon1;
35 ddelta = delta2 - delta1;
36
37
38 %% Modelling using Aki and Richards approximation assuming
       isotropy
39 % Input to Shuey's approximaton
40 Vp = (Vp1 + Vp2)/2;
41 Vs = (Vs1 + Vs2)/2;
42 rho = (rho1 + rho2)/2;
43 VsVp2 = (Vs/Vp)^(2);
44
45 dVp = Vp2 - Vp1;
46 dVs = Vs2 - Vs1;
47 drho = rho2 - rho1;
48
49
50 % Shuey's appproximation of the P-wave reflection coefficient
       at a horizontal interface in an isotropic medium
51
52 A = 0.5*(dVp/Vp + drho/rho);
53 B = dVp/(2*Vp) - 4*VsVp2*(dVs/Vs) - 2*VsVp2*(drho/rho);
54 C = 0.5*(dVp/Vp);
55
56 Rpi = A + B .* (sind(theta)).^(2) + C .* (sind(theta)).^(2).*(
       tand(theta)).^(2);
57
```

```
58 % Approximation to the P-wave reflection coefficientat a
       horizontal boundary in VTI media by Ruger (1997)
59
60 Rpa = 0.5*(dZ/Z) + 0.5 .*(dVp/Vp - (((2*Vs/Vp)^(2))*(dG/G) +
       ddelta)) .* (sind(theta)).^(2) + 0.5 .*(dVp/Vp + depsilon)
       .*((sind(theta)).^(2)) .*((tand(theta)).^(2));
61
62
63
64 %% Plot
65 figure
66 hold on
67
68 plot(theta, Rpi, 'g')
69 plot(theta, Rpa, 'black')
70
71 title('The P-wave reflection coefficient and the effect of
       anisotropy for the Ror-Tofte Fm interface')
72 xlabel('Incident angle')
73 ylabel('P-wave reflection coefficient')
74
75 legend('Rpi','Rpa')
76 hold off
77
78 %% Anisotropy effect in relative change in reflection
       coefficient at different effective angles
79
80 rel_change_24 = (Rpi(24) - Rpa(24))/Rpa(24);
81 rel_change_32 = (Rpi(32) - Rpa(32))/Rpa(32);
82 rel_change_40 = (Rpi(40) - Rpa(40))/Rpa(40);
83 rel_change_48 = (Rpi(48) - Rpa(48))/Rpa(48);
```

```
% Function for removing the anisotropy effect

function amplitude_map_ani = remove_anisotropy(amplitude_map)

    % Input data:
    % The input is the amplitude map sorted by inlines and
       xlines, the output from function horizon_sorting.m.

    ani_coeff = 0.05; % Rel. change in ref. coeff. from
       isotropic to anisotropic case

    amplitude_map_ani = amplitude_map .* (1-ani_coeff);


end
```

B.2 Import functions

```
% 1. Import amplitude maps. Convert from xyz or txt file to three arrays x (x coord. or inline), y (y coord. or xline) and z (amplitude).

function [x_a, y_a, z_a] = amplitude_import(filename)

    % Important:
    % The no. of inlines of the thickness map has to match the no. of inlines of the ampltiude map.

    fid = fopen(filename, 'r'); % Permission to read 'r'

    C = textscan(fid, '%f %f %f', 'headerLines',30); % Skipping the 30 first lines of the header

    x_a = C{1};
    y_a = C{2};
    z_a = C{3};

    %[ind1, ~] = find(z_a<-550); % Find all values lower than 550

    %x_a(ind1) = [];
    %y_a(ind1) = [];
    %z_a(ind1) = [];

    %for i = 1:length(z_a)

    %    z_a(i) = z_a(i) - 1; % The amplitudes have a 1.00 added to them in the export from DSG which needs to be removed

    %end

    fclose(fid);

end
```

```
% 2. Import thickness maps. Convert from .xyz or .txt file to
   three arrays x (x coord. or inline), y (y coord. or xline)
   and z (thickness in TWT).

function [x_t, y_t, z_t] = thickness_import(filename)

    % Important:
    % The no of inlines of the thickness map has to match the
       no of inlines of the ampltiude map.

    fid = fopen(filename, 'r'); % Permission to read 'r'

    C = textscan(fid, '%f %f %f', 'headerLines',30); % Skipping
        the 30 first lines of the header

    x_t = C{1};
    y_t = C{2};
    z_t = C{3};

    [ind1, ~] = find(z_t>=55); % Find all values higher than 55
        ms or lower than 0 ms to remove them
    [ind2, ~] = find(z_t<0);

    x_t([ind1; ind2]) = [];
    y_t([ind1; ind2]) = [];
    z_t([ind1; ind2]) = [];

    fclose(fid);

end
```

```
% 3. Import of .xls- and .xlsx-files of tuning curve data points by conversion to vectors

function [tuning_thickness_TWT, tuning_amplitudes] = tuning_import(filename)

    % Input data:
    % Data starts at row 4. Number of traces is 80, resulting in 81 data points.

    % Column A contains wedge thickness in TWT/TVDss. Column B contains corresponding amplitude values.

    sheet = 1;
    aRange = 'A4:A84'; % Start and end row for data
    bRange = 'B4:B84';

    tuning_thickness_TWT = xlsread(filename, sheet, aRange);
    tuning_amplitudes = xlsread(filename, sheet, bRange);

    % .xlsx files can be read using sheet and range specification. This does not work for .xls files.

    %x = xlsread(filename);

    %range = length(x(:, 1));

    %tuning_thickness = x(4:range, 1);
    %tuning_amplitudes = x(4:range, 2);

end
```

B.3 Detuning scheme

```
% 4. Fit a tuning curve to the wedge model data points

function [P_TWT, no_tuning_amplitude] = tuning_curve(
    tuning_thickness_TWT, tuning_amplitudes)

    % Input data:
    % The vectors containing the thickness values of the wedge
        model (TWT) and the corresponding measured amplitudes
        which makes up the tuning curve.

    % Output data:
    % P is is a vector of length n+1 whose elements are the
        coefficients of an nth-degree polynomial (p(x) = p1x^n +
        p2x^(n-1) +.. + pnx + pn-1x)

    n = 7; %

    [P_TWT, S_TWT] = polyfit(tuning_thickness_TWT,
        tuning_amplitudes, n);

    %P1_TWT = polyval(P_TWT, tuning_thickness_TWT, S_TWT);

    no_tuning_amplitude = tuning_amplitudes(1); % First element
        contains highest thickness

    %thickness1 = linspace(0,n,3);

    %eval = polyval(P, thickness_1);

    % Delta is an estimate of the standard error in predicting
        a future observation at x by p(x)

    %figure

    %plot(tuning_thickness_TWT,tuning_amplitudes, 'o');
    %hold on
    %plot(tuning_thickness_TWT,P1_TWT,'r-');
```

```
30
31      %legend('Wedge model data points', 'Polynomial')
32
33      %xlabel('Wedge thickness (TWT)')
34      %ylabel('Amplitude')
35     % xlim([0 200])
36      %ylim([-0.15 0.05])
37
38      %hold off
39
40      %figure
41
42      %plot(tuning_thickness_TVD,tuning_amplitudes, 'o');
43
44      %hold on
45      %plot(tuning_thickness_TVD,P1_TVD,'r-');
46
47      %legend('Wedge model data points', 'Polynomial')
48
49      %xlabel('Wedge thickness (TWT)')
50      %ylabel('Amplitude')
51      %xlim([0 200])
52      %ylim([-0.15 0.05])
53
54      %hold off
55
56
57
58  end
```

```
1  % 5. Horizon sorting
2
3  function [HzHz1,HzHz2,InIn,XlXl] = horizon_sorting(Inline1,
       Xline1, Hz1, Inline2, Xline2, Hz2)
4
5      % This function sorts two different horizon data sets into
6      % meshgrids, location calues according to their inline and
           Xline position
7
8      % The input is two sets of inlines, xlines and horizon data
           (Hz1 and Hz2)
9      % Set 1: InLine1 , XLine1 , Hz1
10     % Set 2: InLine2 , XLine2 , Hz2
11
12     % Checking the dimensions of each horizon.
13     if min(Inline1) ~= min(Inline2) || max(Inline1) ~= max(
           Inline2)
14         error('Inline dimensions does not match')
15     end
16
17     max_Xl = max([max(Xline1), max(Xline2)]); % Maximum xline
           in data sets
18     max_In = max(Inline1);
19
20     % Creating some grids
21     array1 = NaN(max_Xl, 1); % Creating an array, or a M-by-N (
           max_Xl by 1) matrix of NaNs
22     array2 = NaN(max_Xl, 1);
23
24     % Creating 2D grids of inlines and xlines
25     [InIn, XlXl] = meshgrid(1:max_In,1:max_Xl);
26     % Inline: 1:4416, Xline: 1:5159
27
28     % Creating max_Xl by max_In matrices consisting of NaNs
29     HzHz1 = NaN(size(InIn)); % size(InIn) gives a 5129-by-4416
           matrix consisting of NaNs
30     HzHz2 = NaN(size(InIn));
31
```

```
32      for n = min(Inline1): max(Inline1)  % Loop over the inlines
33
34          % Find indices for inline equal to n
35          [ind1, ~] = find(Inline1==n);
36          [ind2, ~] = find(Inline2==n);
37
38          % Sort them to correspond to the xline position
39          array1(Xline1(ind1)) = Hz1(ind1);
40          array2(Xline2(ind2)) = Hz2(ind2);
41
42          % Add the horizon data to an IlXl grid
43          HzHz1(:,n) = array1;
44          HzHz2(:,n) = array2;
45
46          % Delete data in temporary array
47          array1 = NaN(max_Xl,1);
48          array2 = NaN(max_Xl,1);
49      end
50
51  end
```

```
1  % 6. The detuning function
2
3  function [detuning_curve, tuning_curve, detuned_amplitude_map]
       = detuning(P_TWT, thickness_map_TWT, amplitude_map,
       no_tuning_amplitude)
4
5      % Input data:
6      % The coefficients of polynomial estimating the tuning
           curve, the thicknesses corresponding to the tuning curve
           , the stable amplitude value and the amplitude map which
            is to be detuned.
7
8      tuning_curve = P_TWT(1) .* thickness_map_TWT.^(7) + P_TWT
           (2) .* thickness_map_TWT.^(6) + P_TWT(3) .*
           thickness_map_TWT.^(5) + P_TWT(4) .* thickness_map_TWT
           .^(4) + P_TWT(5) .* thickness_map_TWT.^(3) + P_TWT(6) .*
            thickness_map_TWT.^(2) + P_TWT(7) .* thickness_map_TWT
           + P_TWT(8);
9
10     detuning_curve = no_tuning_amplitude./tuning_curve;
11
12     detuned_amplitude_map = amplitude_map .* detuning_curve;
13
14
15
16 end
```

B.4 AVO attributes and net-to-gross inversion

```
% 7. Horizon de-sorting. Sorting the horizons back into cell
    arrays.

function amplitude_map_ca = horizon_desorting(InIn, XlXl,
    amplitude_map)

    % Finding the elements that are nans and putting them in an
        array
    InIn_desorted = InIn(~isnan(amplitude_map));
    XlXl_desorted = XlXl(~isnan(amplitude_map));
    amplitude_map_desorted = amplitude_map(~isnan(amplitude_map
        ));

    % To replace delete NaN points in InIn: InIn(isnan(
        amplitude_map))
    % = [];

    % Creating the ampltiude map as a cell array, ready for
        attribute calculation or export
    amplitude_map_ca = {InIn_desorted, XlXl_desorted,
        amplitude_map_desorted};

end
```

```
% 8. Intercept (R) and gradient (G) maps
% The R and G 2D maps are created from "angle maps". This function is created for 3 different maps, 1 indicating smallest angle range, and 3 the highest.

function [R_map_1, G_map_1] = AVO_attributes(amplitude_map_1, amplitude_map_2, amplitude_map_3, phi_eff_1, phi_eff_2, phi_eff_3)
%% Input data:
    % The three amplitude maps should be in cell array format. phi_eff indicates the effective angle of each amplitude map.

%% Checking the dimensions of the amplitude maps
    if length(amplitude_map_1{1}) ~= length(amplitude_map_2{1}) || length(amplitude_map_1{1}) ~= length(amplitude_map_3{1}) || length(amplitude_map_2{1}) ~= length(amplitude_map_3{1})
        error('Map dimensions do not match')
    end

    R_map_1 = {zeros(length(amplitude_map_1{1}), 1), zeros(length(amplitude_map_1{1}), 1), zeros(length(amplitude_map_1{1}), 1)};
    G_map_1 = {zeros(length(amplitude_map_1{1}), 1), zeros(length(amplitude_map_1{1}), 1), zeros(length(amplitude_map_1{1}), 1)};

%% Linear fitting with Shueys equation

    x = [(sind(phi_eff_1))^2, (sind(phi_eff_2))^2, (sind(phi_eff_3))^2];
    n = length(amplitude_map_1{1});

    % yfit = P(1) * X + P(2).

    for i = 1 : n

```

```
25          if amplitude_map_1{1}(i) == amplitude_map_2{1}(i)  &&
               amplitude_map_1{2}(i) == amplitude_map_2{2}(i) &&
               amplitude_map_1{1}(i) == amplitude_map_3{1}(i) &&
               amplitude_map_1{2}(i) == amplitude_map_3{2}(i)
26
27              G_map_1{1}(i) = amplitude_map_1{1}(i);
28              G_map_1{2}(i) = amplitude_map_1{2}(i);
29
30              R_map_1{1}(i) = amplitude_map_1{1}(i);
31              R_map_1{2}(i) = amplitude_map_1{2}(i);
32
33              [P, S] = polyfit(x, [amplitude_map_1{3}(i),
                   amplitude_map_2{3}(i), amplitude_map_3{3}(i)],
                   1);
34
35              %P1 = polyval(P, x, S)
36
37              %figure
38
39              %plot(x,[amplitude_map_1{3}(i), amplitude_map_2{3}(
                   i),amplitude_map_3{3}(i) ], 'o')
40
41              %hold on
42              %plot(x,P1,'r-')
43
44              %title(['AVO attributes: Linear fit for data
                   contained in line ', num2str(i),''])
45
46              %legend('12-20, 20-28, 28-36 map points', 'Linear
                   fit ')
47
48              %xlabel('sin(theta)^2')
49              %ylabel('Amplitude')
50              %xlim([0 40])
51              %ylim([0 2000])
52
53              %%hold off
54
55              G_map_1{3}(i) = P(1);
```

```
56                R_map_1{3}(i) = P(2); % Last p is intercept
57
58            else
59                R_map_2{1}(i) = 0;
60                R_map_2{2}(i) = 0;
61
62                G_map_1{1}(i) = 0;
63                G_map_1{2}(i) = 0;
64
65                R_map_2{3}(i) = 0;
66                G_map_1{3}(i) = 0;
67            end
68        end
69
70    end
```

```
% 9. Function for estimating N/G from R and G

function [NG_map_R, NG_map_G] = NG_inversion(R_map, G_map)
%% Input data:
% The input map is a cell array, where the gradient map has
    been through the desorting function.

%% Well 1 data: J-1
    % Layer 1 avg properties
    rho1_1 = 2598;
    Vp1_1 = 4117;
    Vs1_1 = 2444;

    % Layer 2 avg properties
    rho1_2 = 2465;
    Vp1_2 = 4324;
    Vs1_2 = 2704;
    NG1 = 0.95;

    drho1 = 2*((rho1_2 - rho1_1)/(rho1_2 + rho1_1));
    dVp1 = 2*(Vp1_2 - Vp1_1)/(Vp1_2 + Vp1_1);
    dVs1 = 2*(Vs1_2 - Vs1_1)/(Vs1_2+Vs1_1);
    gamma1_1 = (Vs1_1/Vp1_1)^2;

    % Calculated R and G
    R1 = 186;
    G1 = -14321;

    %% Scalars in well 1
    A1 = (2*R1)/(NG1*(dVp1 + drho1))
    B1 = (2*G1)/(NG1*(dVp1 - 2*gamma1_1*(drho1 + 2*dVs1)))

    %A1 = (0.5*NG1*(dVp1 + drho1))/R1;
    %B1 = (0.5*NG1*(dVp1 - 2*gamma1_1*(drho1 + 2*dVs1)))/G1;

    %B_amp = (2*(-15633))/(NG1*(dVp1 - 2*gamma1_1*(drho1 + 2*
        dVs1))) % G input from amplitude map
    %% Well 2 data: J-4
```

```
37      % Layer 1 avg properties
38      rho2_1 = 2581;
39      Vp2_1 = 4070;
40      Vs2_1 = 2472;
41
42      % Layer 2 avg properties
43      rho2_2 = 2413;
44      Vp2_2 = 4085;
45      Vs2_2 = 2660;
46      NG2 = 1;
47
48      % Calculated R and G
49      R2 = -2470;
50      G2 = -10154;
51
52      drho2 = 2*((rho2_2 - rho2_1)/(rho2_2 + rho2_1));
53      dVp2 = 2*(Vp2_2 - Vp2_1)/(Vp2_2 + Vp2_1);
54      dVs2 = 2*(Vs2_2 - Vs2_1)/(Vs2_2+Vs2_1);
55      gamma1_2 = (Vs2_1/Vp2_1)^2;
56
57      %% Scalars in well 2
58      A2 = (2*R2)/(NG2*(dVp2 + drho2))
59      B2 = (2*G2)/(NG2*(dVp2 - 2*gamma1_2*(drho2 + 2*dVs2)))
60
61      %A2 = (0.5*NG2*(dVp2 + drho2))/R2;
62      %B2 = (0.5*NG2*(dVp2 - 2*gamma1_2*(drho2 + 2*dVs2)))/G2;
63
64      %% Average scalars
65      A = (A1 + A2)/2
66      B = (B1 + B2)/2
67
68      %% Average change in Vp, Vs and rho
69      dVp = (dVp1 + dVp2)/2
70      dVs = (dVs1 + dVs2)/2
71      drho = (drho1 + drho2)/2
72      gamma1 = (gamma1_1 + gamma1_2)/2
73
74      %% Estimate the net-to-gross map from the dependence
           between G and N/G
```

```
75
76      NG_map_G = (2 .* G_map) ./ (B*(dVp- 2*gamma1 *(drho + 2*dVs
            ))); % Weak approximation
77      NG_map_R = (2 .* R_map) ./ (A*(dVp + drho));
78
79  end
```

B.5 Export function

```
% 10. Amplitude export

function Y = amplitude_export(amplitude_map_ca, filename_output)

    fid = fopen(filename_output, 'w+'); % open or create file for reading and writing; discard existing contents

    c = clock;

    % Defining the header
    11 = '@File_Version: 4';
    12 ='@Coordinate_Type_is: 0';
    13 = '@Export_Type_is: 1';
    14 = '@Number_of_Projects 8';
    15 = '@Project_Type_Name: , 3,MC3D-HVG2013, 3,ce0801, 3,sw7005, 3,sw7044, 3,sw7053, 3,tr1000, 3,tr1008, 3,tr1100,';
    16 = '@Project_Unit_is: meters ,
       ST_ED50_UTM32N_P23032_T1133 ,
       PROJECTED_COORDINATE_SYSTEM';
    17 = '#File_Version_____________-> 4';
    18 = '#Project_Name_____________-> MC3D-HVG2013';
    19 = '#Project_Type_____________-> 3';
    110 = '#Export_XY_Unit__________-> meters';
    111 = '#OpenWorks_Project_______-> ''ASG_SMB_SMS''';
    112 = '#Master_Project_______->';
    113 = '#Coordinate_type_________-> 0';
    114 = '#Number_of_points_in_hzd_-> 1';
    115 = '#Horizon_internal_id_____-> 29816';
    116 = '#Horizon_extremes_are____-> -21327.67578  -0.00203';
    117 = '#Horizon_onset_is_Minimum_____-> 1';
    118 = '#Horizon_type_is_MAX_NEG_AMPLITUDE_____-> 0';
    119 = '#Horizon_color_is________-> 255 0 0';
    120 = '#Horizon_name____________-> Tofte_Fm_SMB_Top+SMB14_HVG13_20-36_IL_int_x-x_detuned';      % Change according to input
```

```
30      121 = '#Horizon_attribute_______-> MAX_NEG_AMPLITUDE';
31      122 = '#Horizon_version_________-> 2019';
32      123 = '#Horizon_interp_status___-> STUDY';
33      124 = '#Horizon_class___________-> INTERPOLATED';
34      125 = '#Export_Z_Unit___________-> ';
35      126 = '#Horizon_onset_type______-> Minimum';
36      127 = '#Horizon_data_domain_____-> OTHER';
37      128 = '#Horizon_remark_size_____-> 62';
38      130 = '#End_of_Horizon_ASCII_Header_';
39
40      %fprintf('Calculated on the %.0f.%.0f.%.0f at %.0f.%.0f.%.0
            f', c(3), c(2), c(1), c(4), c(5), c(6));
41
42      % Writing the header and the columns of data to the file
43      C = [amplitude_map_ca{1}, amplitude_map_ca{2},
            amplitude_map_ca{3}];
44
45      fprintf(fid, '%s\n %s\n %s\n %s\n %s\n %s\n %s\n %s\n
          %s\n %s\n %s\n %s\n %s\n %s\n %s\n %s\n %s\n %s\n %s\n %
          s\n %s\n %s\n %s\n %s\n %s\n %s\n Calculated on the
           %.0f.%.0f.%.0f at %.0f.%.0f.%.0f\n using MATLAB R2017b.
           %s\n',11,12,13,14,15,16,17,18,19,110,111,112,113,114,
          115,116,117,118,119,120,121,122,123,124,125,126,127,128,
          c(3), c(2), c(1), c(4), c(5), c(6),130);
46      fprintf(fid,'%.1f %.1f %.5f\n', C.');
47      fprintf(fid,'EOD');
48      fclose(fid);
49
50      Y = 1;
51      fprintf('The export to text-file was successful.')
52
53  end
```